BOSTON UNIVERSITY

COLLEGE OF ENGINEERING

Dissertation

ROLE OF MIXED IONIC AND ELECTRONIC TRANSPORT ON ELECTROCATALYTIC ACTIVITY OF INFILTRATED NANOPARTICLES IN SOLID OXIDE FUEL CELL CERMET ELECTRODES

by

BOSHAN MO

B.S., Boston University, 2016
M.S., Boston University, 2016

Submitted in partial fulfillment of the

requirements for the degree of

Doctor of Philosophy

2020

© 2020
BOSHAN MO
All rights reserved

Approved by

First Reader
Srikanth Gopalan, Ph.D.
Associate Professor of Mechanical Engineering
Associate Professor of Materials Science and Engineering

Second Reader
Uday B. Pal, Ph.D.
Professor of Mechanical Engineering
Professor of Materials Science and Engineering

Third Reader
Soumendra N. Basu, Ph.D.
Professor of Mechanical Engineering
Professor and Associate Division Head of Materials Science and Engineering

Fourth Reader
Emily Ryan, Ph.D.
Assistant Professor of Mechanical Engineering
Assistant Professor of Materials Science and Engineering

ACKNOLEDGEMENTS

Throughout the writing of this dissertation I have received a great deal of support and assistance.

A special thanks to my family. Words cannot express how grateful I am to my friends and family, especially my parents and in-laws, for the wise counsel, sympathetic ear, and for all of the sacrifices that they've made on my behalf. Without them, I would not be the person I am today.

I would like to thank my primary advisors: Professor Gopalan, Professor Pal, and Professor Basu. Without the consistent guidance, tutelage, support, unparalleled knowledge, and encouragement of my three mentors, this thesis would never have existed. I would like to thank Professor Gopalan supporting my research and the ideas we developed during my doctorate, who went above and beyond to read every line of the manuscript in meticulous detail. I thank Professor Pal for accepting me as a Masters student, and giving me the chance to work with his group. I must say a special thank you to Professor Basu - your insightful feedback pushed me to sharpen my thinking and brought my work to a higher level, even while I was just an undergraduate at BU. The advice you all have given me toward research as well as my career has been invaluable.

My sincere thanks must also go to Professor Emily Ryan, Professor Bishop for serving as my committee members.

My work would not have been possible without the support of my labmates, but a I am extremely grateful for my project partners, Paul Gasper, Yanchen Lu and Jillian Rix, as they were instrumental in defining the path of my research; Paul for his willingness to help and for his eclectic experiences and knowledge, and Yanchen Lu for always extending his hospitality, as

well as his sense of humor. I would like to extend a special thanks to the co-author of my papers: Jillian Rix for her support and energy.

I would like to acknowledge my equipment staff and characterization team for their wonderful collaboration. I would particularly like thank Bob Sjostrom, Kara Mogensen, David Campbell, Joe Estano in EPIC, and Anlee Krupp in the Photonics Center, I thank you for your guidance and teachings to design and characterize my experiments.

I would also like to thank the Administrative staff, Elizabeth Flagg and Ruth Mason for their valuable guidance throughout my studies. A special thanks to Nicole Lawton, for handling all capital purchases and ordering. You provided me with the tools that I needed to successfully complete my dissertation.

To my wife, Jeanne Tran, I thank you for all the love and constant encouragement you have given me, for all the late nights and early mornings, and for keeping me sane over the past few months. You have always been a shining example of how hard work, perseverance and dedication can define a person, and you always push me to be my best. Thank you for being my muse, editor, proofreader, and support. But most of all, thank you for being my best friend. I owe you everything.

Finally, despite my love for mathematics, the work reported in this thesis would not have been possible without the financial support of the Department of Energy under award DE-FE0026096 for which I am grateful.

ROLE OF MIXED IONIC AND ELECTRONIC TRANSPORT ON ELECTROCATALYTIC ACTIVITY OF INFILTRATED NANOPARTICLES IN SOLID OXIDE FUEL CELL CERMET ELECTRODES

BOSHAN MO

Boston University College of Engineering, 2020

Major Professor: Srikanth Gopalan, Ph.D.,
Associate Professor of Mechanical Engineering,
Associate Professor of Materials Science and Engineering

ABSTRACT

The infiltration of nanoparticle electrocatalysts into solid oxide fuel cell (SOFC) electrodes has been proven to produce a high density of electrochemically active sites, and reduce charge transfer polarization losses in SOFC electrodes. This is crucial for intermediate temperature operation, as these losses increase greatly at lower temperatures. Nickel-yttria stabilized zirconia (Ni-YSZ) cermets are low-cost, and exhibit excellent stability, but their main disadvantage stems from nickel coarsening and performance loss over their operational lifetimes. Infiltration of electrocatalyst nanoparticles has been shown to mitigate nickel coarsening and the consequent anode degradation. In this work, the effects of these infiltrants have been observed in a standard Ni-YSZ electrode. In addition to nickel, mixed ionic and electronic conducting (MIEC) phases have been infiltrated into Ni-YSZ scaffolds and their performance characterized using electrochemical impedance spectroscopy (EIS). Cross-sectional microscopy of fractured cells has been used to compare electrode microstructure and particle statistics. A model has been proposed to explain the origin of anode performance enhancement from nanoscale electrocatalysts.

LIST OF FIGURES

LIST OF TABLES

LIST OF ABBREVIATIONS

AC	Alternating Current
AAL	Anode Active Layer
DC	Direct Current
DPB	Double Phase Boundary
DRT	Distribution of Relaxation Times
ECM	Equivalent Circuit Model
EIS	Electrochemical Impedance Spectroscopy
FeYSZ	Iron Oxide doped YSZ
GDC	Gadolinium Doped Ceria
I-V	Current-Voltage
Ni	Nickel
Ni-YSZ	Nickel – Yttria Stabilized Zirconia
NiO	Nickel Oxide
SEM	Scanning Electron Micrograph
SOFC	Solid Oxide Fuel Cell
TiYSZ	Titania doped YSZ
TLM	Transmission Line Model
TPB	Triple Phase Boundary
TPZ	Triple Phase Zone
YSZ	Yttria Stabilized Zirconia

1. INTRODUCTION

Solid oxide fuel cells (SOFCs) are a solution to the energy and environmental problems we face now as well as in the coming future. They are devices that utilize fuel, in the form of reformed hydrocarbon gases, i.e. hydrogen and carbon monoxide by electrochemically oxidizing them, and delivering electrons through an external circuit. This direct electrochemical reaction means that intermediate steps, such as a heat to mechanical work transformation, are not present. This allows SOFCs to operate without certain thermodynamic limitations, such as Carnot efficiency [1-5]. Not only are they more efficient than turbines and engines at electrical conversion, with a 60%-75% conversion rate, but when coupled with a combined heat and power system, the high-grade heat produced can bring the conversion of useable energy up to 80% efficiency via cogeneration [6,7]. SOFCs have no direct combustion reactions during operation, which lead to lower emissions of CO_2, NO_x, and SO_x compounds as well as lower particulate matter emissions. As evident by its name, the electrolyte is a solid oxygen ion conductor, which does not require a corrosion management system unlike its liquid electrolyte counterparts. Their lack of moving parts mean SOFCs are noise and vibration free, and require only pumps to regulate flow of fuel and oxidant gases. Lastly, their modular design allows SOFC cells to be assembled in series or parallel circuits, allowing applications ranging from utility grid conversion down to biofuel electric vehicle integration [8,9].

Unfortunately, there are still many barriers of entry that hold SOFCs back from mainstream adoption by companies and manufacturers. Their largest disadvantages include cost, durability and performance of the individual cells. This project attempts to address all of the disadvantages within the conventional anode electrode, nickel-ytrria stabilized zirconia (Ni-YSZ), with minimal additional processing methods, all of which will be discussed in Chapter 2.

Recently, one direction is to improve performance by infiltrating nanostructured electrocatalysts into the electrode. In particular, the precipitation and decomposition of metal nitrate mixtures within a pre-sintered scaffold is an emerging approach of interest [10-11]. This infiltration of metal precursors can not only form bulk phases, but also nanoparticle electrocatalysts within the electrode. The nanoscale features effectively increase the surface-to-volume ratio of the metal phases, increasing the density of sites for electrochemical reactions to take place [12,13].

One example is the infiltration of nickel nanoparticles into a Ni-YSZ scaffold, which has shown cell performance improvement without the need to introduce third component into the cermet. Although the initial performance of the cell does show improvement, continuous operation of the cell also shows coarsening of the infiltrated nanoparticles. This is significant especially at higher humidity levels in the anode gas (fuel). Prior work has shown that higher humidity levels in the anode allows nickel wetting for both the bulk and nanoscale phases [14-15]. This coarsening behavior has been observed alongside other metal infiltrants, but the mechanism driving this phenomenon is still unclear.

Although coarsening is more difficult to explain, the contribution of the metal nanoparticles to the overall cell performance can be described through the increase in electrochemically active sites and the transport of electrons through the metal phase. The addition of particles with a smaller feature size decreases the average feature size of the electrode, and increases the density of electrochemical sites within the active layer of the electrode [14-17]. These metallic nanoparticles not only provide more active sites to increase the rate of the charge transfer reaction. However, they can only be effective if they are not isolated as will be described further below.

Challenges that impede infiltration studies on anode cermets include the extent of processing behind the method. First, Ni-YSZ anode supported cells must be prepared in-situ by isolating and reducing the anode's nickel oxide (NiO), while maintaining the cathode under an oxidizing environment at operating temperatures. The anode support reduces to Ni-YSZ in the process, but it becomes much more fragile, and it is sensitive to stress and temperature changes after reduction [18-19]. One of the possible methods to combat this problem included infiltrating the NiO-YSZ active layer before reduction, but the technology is not easy to replicate and the overall loading of Ni nanoparticles was poor due to insufficient porosity [20].

Previous work in this project has shown that pre-reducing the cells in-situ at operating temperature, infiltrating the cells at room temperature and heating to a predetermined decomposition temperature is a solution to test infiltrated Ni-YSZ anode supports [21-23]. These studies have shown that not only do metal nitrate solution infiltrants improve initial cell performance, but infiltrants containing mixed ionic and electronic conducting phases, such as Gadolinium Doped Ceria (GDC), have also shown improvements in cell performance.

To continue further and elucidate the effects of infiltration, the present research systematically studies the effect of infiltration of electrocatalyst nanoparticles in SOFC electrodes comprising symmetrical cells. Symmetrical cells were infiltrated with multiple cycles of the same infiltrant solution, to observe if the cell electrochemical performance always continues to increase with the number of infiltration cycles, or if there is reversal in performance after a certain number of infiltration cycles. These electrochemical measurements will be correlated with the cross-sectional microstructure of the cells, to determine if the infiltration cycles lead to different microstructures which in turn influence their electrochemical performance. Lastly, an electrochemical model incorporating the distribution of relaxation times

(DRT) is developed to further simulate how the kinetics of the various electrochemical processes in the electrodes change with infiltration and different operating parameters.

The objective of this dissertation is to research and analyze how infiltration affects different anode materials, which will be presented in five chapters. Chapter two introduces the SOFC technology and its applicable fields, compares and contrasts the features within symmetric cells to conventional SOFCs, describes the infiltration process of electrocatalyst nanoparticles and the relevant techniques for measuring electrochemical performance of SOFCs, and describe modelling techniques to deconvolute the different polarization processes that impact symmetric cells. Chapter three describes the experimental results of a study on the impact of different infiltration cycles of electrocatalyst nanoparticles on the performance and stability of Ni-YSZ electrodes: the first part of chapter three studies the effect of infiltration of an existing phase, nickel, as the electrocatalyst; the second part of chapter three studies the effect of infiltration of a mixed ionic and electronic conduction (MIEC) phase as an electrocatalyst into the substrate. Chapter four explores the experimental results of a study discussing the impact of infiltration cycles of nickel nanoparticles on anode electrodes consisting of an MIEC phase substituting the ionic phase of the material, as well as an equivalent circuit to attribute polarization resistances to physical processes. The mechanisms behind activation polarization are further elucidated using transmission line models alongside DRT analysis, concluding that infiltrated nanoparticles must have a MIEC phase in order to be fully utilized. Chapter five further explores the effects of humidity conditions and operating temperature on cermet electrodes containing MIECs. Chapter six and seven summarizes any additional work and proposes topics and phenomena of discussion in future work.

2. BACKGROUND AND PROBLEM STATEMENT

2.1 Literature Review

2.1.1 Solid Oxide Fuel Cells

Whereas there are many types of fuel cells which utilize liquid electrolytes, solid oxide fuel cells are comprised of a solid oxide electrolyte, which allows oxygen ions resulting from reduction of molecular oxygen on the cathodic side to selectively pass through to the anodic side where they react with fuel and liberate electrons. The electrons liberated on the anodic side transport through an external circuit to the cathode side. In order for the oxygen ions to migrate across the electrolyte, SOFCs typically operate around temperatures between 600 - 1000°C to reduce various polarization losses [1-3]. The exothermic heat liberated due to the electrochemical oxidation of fuels provides high-grade heat for heating and cogeneration applications, in addition to the high electrical power generation efficiency [4,5]. Unfortunately, high-temperature operation has its disadvantages as well including undesirable interfacial reactions and differential thermal expansion between contiguous layers. This differential thermal expansion leads to delamination of layers at the interfaces between components during thermal cycles. The other caveat that affects SOFCs is that long term operation at high temperatures has been found to also degrade the overall cell performance, and this degradation stems from a variety of factors, including but not limited to: the poisoning of the cells' electrochemically active regions due to a variety of contaminants; the microstructural stability of the electrodes' scaffolds; the sudden changes in operating conditions due to external factors [1,2].

The SOFC cell is shown in Fig. 1 and primarily consists of three components: the anode, cathode, and electrolyte. Under fuel cell operating conductions, a fuel gas, e.g. hydrogen gas (H_2), is passed through channels in contact with the anode, while an oxidant gas, for example air, is passed through cathode gas channels. The fuel is oxidized within the anode, releasing electrons into the external circuit. To complete the circuit, the electrons liberated on the anode side transport back to the cathode side where they participate in reducing oxygen gas to oxygen ions. To maintain charge and mass balance, these oxygen ions then migrate through the electrolyte from the cathode to the anode, and react with the oxidized fuel. As long as the spent fuel and oxidants are constantly replenished with new gas and the operating conditions are maintained, the cell can continue long-term operation, typically many years.

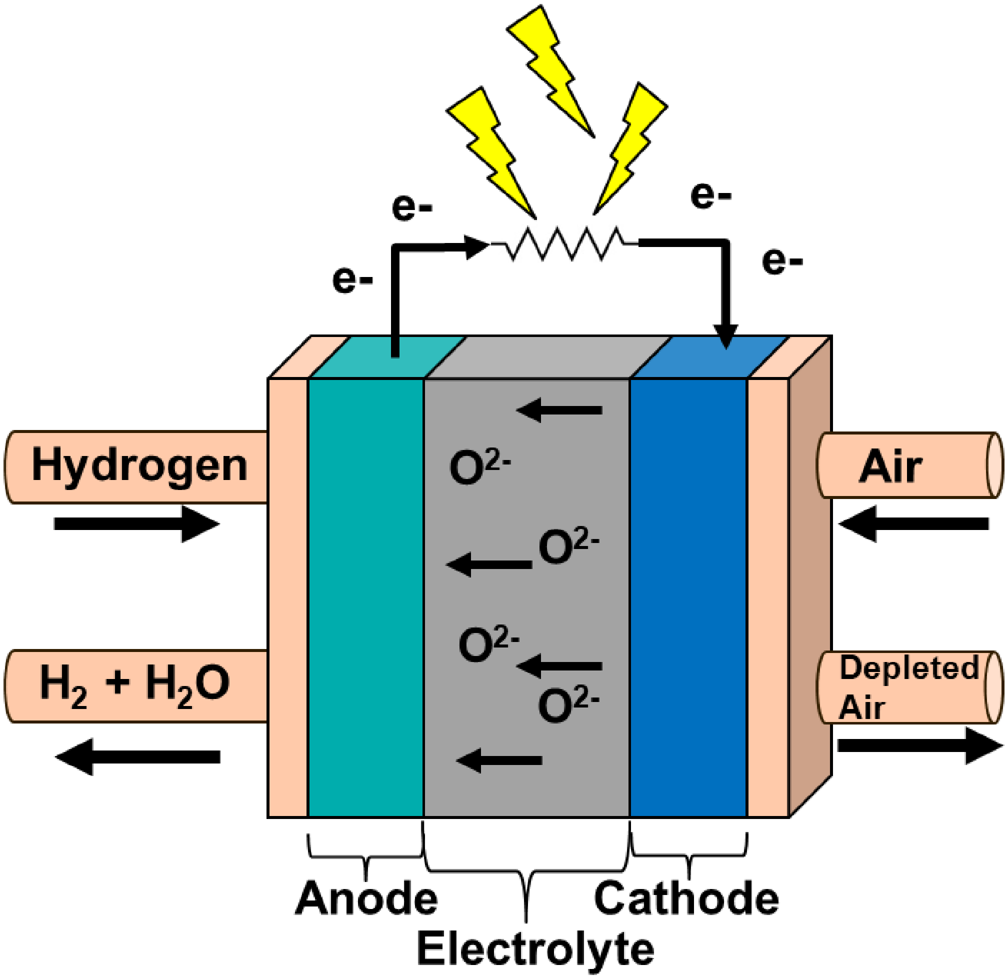

Figure 1:SOFC operating with hydrogen gas as its fuel source and air as its oxidant.

The complete cell reaction actually is composed of two half-cell reactions, one which occurs at the anode and the other which occurs at the cathode. Both sides require facile molecular transport of gas, and the transport of electrons and ions to and away from the reaction sites for the half-cell reactions to occur. Each species participating in the reaction is typically transported through a different phase. In an SOFC anode, the phases that must be in contact are the pore phase (gas transport), the metallic phase (electron transport) and the ionic conducting phase (ion transport). When viewed as a 2D cross-section, these Triple Phase Boundaries (TPBs), regions where all three phases intersect and interact, show up as a point. In actuality, TPBs are one dimensional structures (meandering lines) that run throughout the electrode, which can be quantified and compared between cells and even within different regions within the electrode. Measuring the density of TPBs, in units of length per unit volume, provides a quantitative measure of the active regions of composite electrodes such as the cermet anode and composite cathode. In the case of the anode, active layers with higher TPB densities have resulted in better electrochemical performance. One proposed method to increase TPB density involves reducing the feature sizes of the TPB phases, and increasing their surface-to-volume ratios. Other proposed methods include changing the anode composition, as well as more process-intensive changes such as novel electrode architectures [24-25].

Current SOFC systems most commonly use a planar anode-supported cell. This type of cell consists of a porous Ni-YSZ cermet substrate ranging from thicknesses of 200-1000 microns, which also provide structural support for the cell. The cell also consists of a YSZ electrolyte a few microns thick, and a cathode (typically a hole and oxygen ion conducting perovskite oxide) with a thickness of tens of microns. In order to improve the electrochemical catalysis of the cell, the TPB densities near the electrode-electrolyte interfaces are improved by sandwiching TPB-dense ‘active layers’ for both electrodes with respect to the electrolyte. The active layers consist of smaller features and finer microstructures, as well as composite phases (such as Lanthanum Strontium Manganite-YSZ) to increase TPBs.

2.1.2 SOFC performance losses

Polarization, or the voltage loss within the cell, is a function of electrochemical device’s current density; as the device is operated at higher current densities and power outputs, it will run at lower thermodynamic efficiencies. In order to produce durable and reliable energy electrical power, one crucial objective is to reduce the total polarization. In SOFCs, there are three main polarization components--ohmic polarization, activation polarization and concentration polarization. Fig. 2 below shows the current density-voltage (I-V) characteristics of a typical full cell, and the polarization losses that occur as a function of current density.

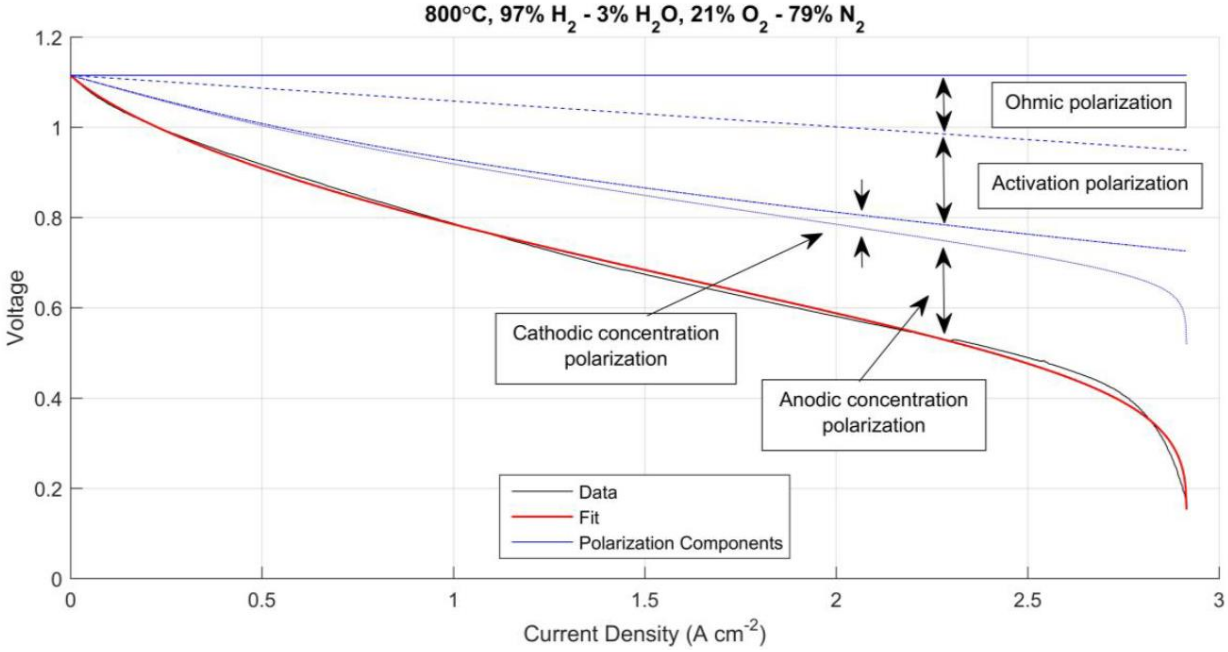

Figure 2: Example of an I-V scan of a SOFC full cell, indicating the polarization losses and their magnitude with respect to current density. At lower current densities, the majority of losses are due to the anodic activation polarization and concentration polarization [26].

Ohmic polarization is the resistance offered by the various components to the transport of charge carriers. This polarization follows Ohm’s law, and has a linear relationship with the current density. This can be seen most prominently in the middle region of a fuel cell’s I-V performance, where a constant slope can be measured. The linear coefficient that determines the ohmic behavior is the resistivity, which is intrinsic to each material component. The total ohmic polarization and ohmic resistance can be calculated with Equations 1 and 2 shown below,

$$\eta_{Ohmic} = R_{Ohmic} i \tag{1}$$

$$R_{Ohmic} = \rho_a l_a + \rho_e l_e + \rho_c l_c + R_{contact} \tag{2}$$

Where i is the current density through the cell, ρ is the intrinsic resistivity of the component, l is the average thickness of the component and $R_{contact}$ is the area-specific contact resistance from each interface present in the cell. The subscripts a, c and e denote the anode, cathode and electrolyte respectively. Intrinsic resistivity is the reciprocal of the electrode or electrolyte conductivity, which is dependent on the speed at which the main charge carrier species can transfer through the material. Although the electrolyte is unable to conduct electrons, it is able to transport oxygen ions, meaning its ionic conductivity, and therefore ionic resistivity ρ_e, can be measured. The generally accepted ionic conductivity of YSZ at 800°C is 5 S/m, which is much slower than the electronic conductivity of Ni in the anode and that of the perovskite oxide used in the cathode [27]. The largest contribution to ohmic polarization present in most fuel cells is due to electrolyte resistivity; for commercial cells, this is mitigated by fabricating thin electrolytes through methods such as spin-coating or lamination. The total impedance can be corrected for ohmic polarization, leaving behind activation and concentration polarization contributions.

Activation polarization is the second type of resistance found in the cell; it originates from the sluggish charge-transfer reactions, or half-cell reactions along the electrode-electrolyte interfaces. The voltage loss attributed to these charge-transfer reactions is categorized as activation polarization. The rates half-cell reaction rates are partly determined by the number of electrochemically active sites, which is a function of the electrode's microstructure and material composition. Other factors that can affect activation polarization is the rate of intrinsic reaction which in turn depends on the operating temperature and the oxidant and fuel gas composition at the cathode and anode respectively.

The third major polarization loss is the concentration polarization, which is a resistance related to the mass transport within the porous electrodes. The half-reaction continuously consumes reactants and produce products, leading to concentration gradients throughout the electrode. At high current densities, the rate of reaction may be significant enough that the diffusion of gases is insufficient to supply the requisite reactants to the electrochemically active sites, and remove the byproducts from the electrochemically active sites in the electrode scaffold.

For the symmetric cells in this study, humidified hydrogen is the primary gas used while testing. The mass transport for this setup is a function of the gas composition and electrode microstructure. However, it has been determined that due to the specific architecture of the symmetric cells used in this study, discussed in the next section, the concentration polarization losses and the resistance associated with it are insignificant compared to the other polarization losses and resistances.

2.1.3 Electrochemical Impedance Spectroscopy

Among various electroanalytical methods, Electrochemical Impedance Spectroscopy (EIS) is one of the most frequently used characterization techniques for evaluating the performance of electrochemical devices such as SOFCs [1,2]. Measurements are performed by characterizing the impedance spectra of the electrochemical cell by varying the frequency of an alternating input signal. The input signal can be voltage or current controlled, but it will be denoted as an alternating-current (AC) source, which a bias will be denoted as direct current (DC) in this work. By applying a small AC perturbation to the cell (as input), a AC response signal can be measured (as output). Thus, if an AC voltage signal ($\vec{\boldsymbol{V}}$) is used to perturb the cell, an AC current signal ($\vec{\boldsymbol{I}}$) is measured. The entire impedance spectra can be plotted using Ohm's law (Equation 3), which is usually represented in a Nyquist plot which displays the negative reactance (X_f) versus the resistance(R_f) of the cell's AC response at the tested frequencies (Equation 4), as well as a Bode plot which displays negative reactance of the cell's AC response versus frequency (Equation 5).

$$Z_{frequency} = \overrightarrow{\boldsymbol{Z_f}} = \frac{\overrightarrow{\boldsymbol{V_f}}}{\overrightarrow{\boldsymbol{I_f}}} = R_f + iX_f \tag{3}$$

$$Nyquist(f) = (R_f, -X_f) \tag{4}$$

$$Bode(f) = (f, -X_f) \tag{5}$$

A schematic for EIS measurement and Nyquist plot for a full SOFC is depicted below in Fig. 3. In Fig. 3b the left x-intercept on the real axis corresponds to the high-frequency AC response at the cell's characteristic frequency, and measures R_{Ohmic}, the ohmic resistance of the cell, current collectors and lead wires. The right x-intercept on the real axis is the low-frequency AC response of the cell, and corresponds to the total resistance of the cell, including ohmic resistance, activation polarization resistance and concentration polarization resistance. By subtracting the left intercept from the right intercept, the ohmic resistance can be omitted from the total resistance, leaving behind the cell's polarization resistance, or the losses due to slow charge-transfer and mass-transfer processes in the electrodes. While EIS does allow measurement of the cell's ohmic and polarization resistance, it is not simple to separate the other polarization processes from one another.

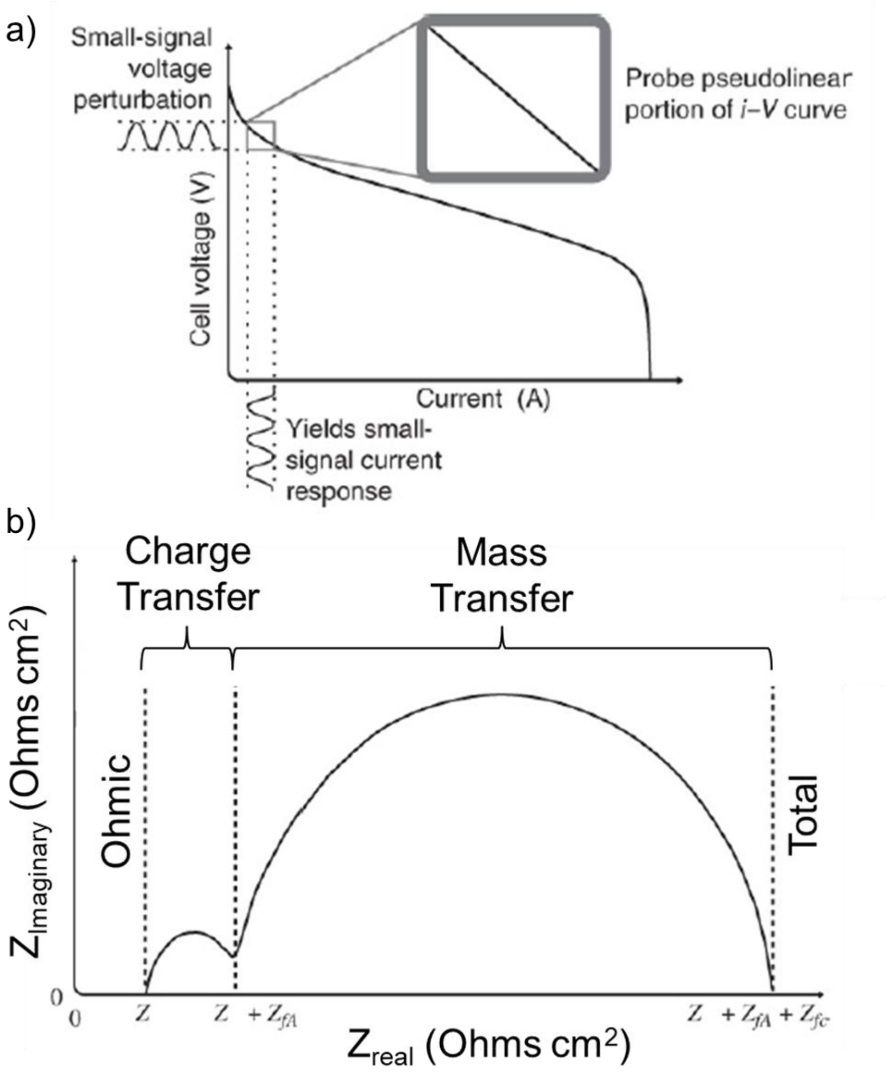

Figure 3: a) Schematic of an EIS potentiostatic measurement and b) the entire EIS spectra over the tested frequency range, showing ohmic and total resistance. Although this work models the other polarizations as two semicircles, in reality the shape may be a superposition of semicircles and is difficult to deconvolute polarization processes [1].

2.1.4 Distribution of Relaxation Times

In recent works, the use of the distribution of relaxation times (DRT) transformation has been applied to EIS spectra to identify and separate individual cell processes which contribute to polarization losses [24,25]. While DRT does provide more insight into the characteristic frequencies at which losses occur, it cannot be solely relied on as the transformation itself is highly sensitive to data quality and the selection of multiple regularization parameters [26]. The exact derivation is outside of the scope of this work, but a general schematic is shown in Fig. 4. The equivalent circuit of the cell can be defined with multiple circuit elements, with each element having a resistance and characteristic frequency. The transformation is performed by convolving a Radial Basis Function (RBF) with each element with respect to frequency, and performing the summation to obtain the function $g(\tau)$, which is the DRT. In this work, DRT timescales (reciprocal of frequencies) are plotted with respect to frequencies to identify an appropriate ECM which accurately describes the real processes which occur in the cells. The relevant parameters and the DRT transformation code used are included within Appendix 1.

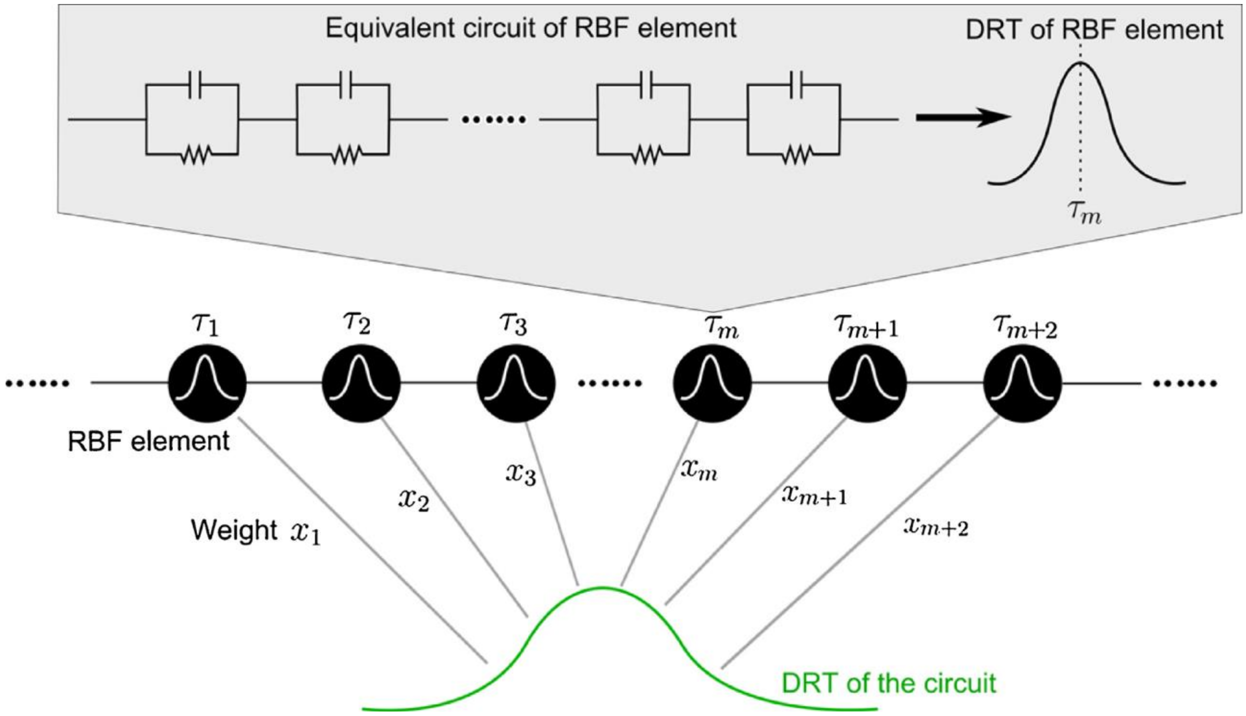

Figure 4: Schematic of DRT using RBF discretization [26].

2.1.3 Symmetric Solid Oxide Fuel Cells

The performance of a planar SOFC can be measured by using I-V scans to measure power density as an overall metric of cell performance. However, it is difficult to separate the effects of the polarization contributions from both the anode and cathode. Previous research related to this work from our group has been able to demonstrate that infiltration of nanoparticle electrocatalysts into SOFC anodes have improved overall cell performance especially at lower temperatures, but there are open questions related to the mechanisms of the performance improvements that have been realized [14,15]. These include questions about nanoparticle coarsening, the role of temperature and humidity, and the optimum nanoparticle density. To address this, symmetric cells were designed, fabricated and tested in order to further understand the effects of infiltration on the anode. Prior works in other groups have also utilized these types of cells to compare and measure cell performance [27-29]. These symmetric cells are electrolyte supported, and have two electrodes with identical composition, screen-printed on each side. The schematics of the cross section of both a full cell as well as a symmetric, fuel electrode/YSZ/fuel electrode SOFC before the reduction of NiO to Ni can be seen in Fig. 5.

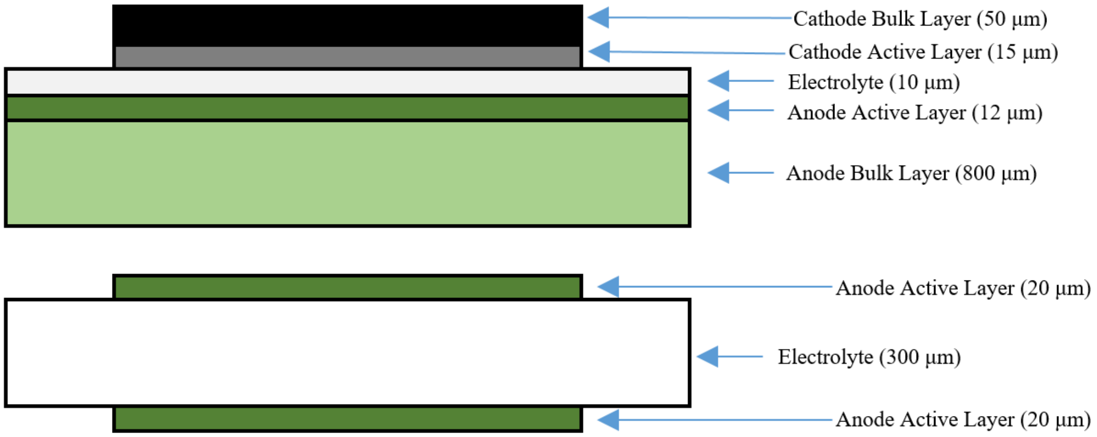

Figure 5: Two schematic fuel cell cross sections. Above is a schematic cross section of an anode supported SOFC. Below is a schematic cross section of a electrolyte supported symmetric cell.

In this work, both electrodes consist of candidate anode materials for the anode active layer (AAL) which are infiltrated with nanoparticle catalysts, or left pristine and uninfiltrated. The screen-printed electrodes are tens of microns thick, minimizing the contributions from concentration polarization on the cell. The only significant impedances that the cell would experience would be activation polarization and ohmic polarization, the latter of which can be characterized and manually subtracted from the total resistance using EIS. Additionally, the symmetric cell has identical electrodes, allowing the cell to be run in a single chamber setup, as shown in Fig. 6. The fuel electrode does not have to isolated from the oxygen electrode, unlike the conventional SOFC which require unique gases for the cathode and the anode. Although the drawback is that the cell has Nernst voltage of 0 (as $p_{O_2,anode} = p_{O_2,cathode}$), EIS can still be conducted under zero DC bias, giving a clear picture of how infiltration affects the activation polarization associated with the AAL.

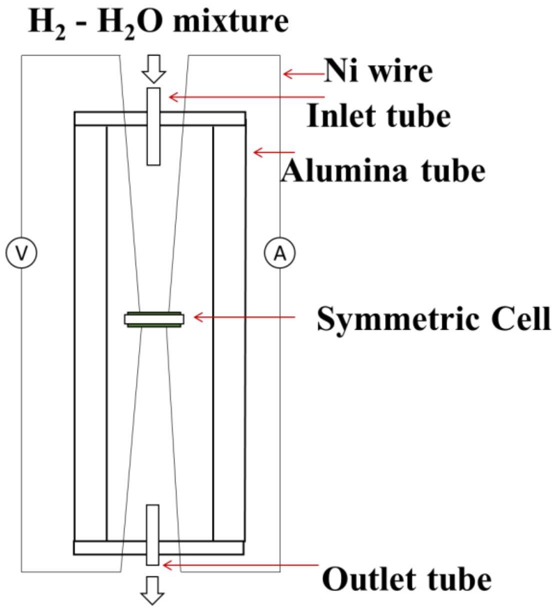

Figure 6: Electrochemical test setup for the symmetric cell.

2.1.4 Infiltration of nanoparticle electrocatalysts into symmetric cell anode layer materials

Liquid infiltration is a relatively simple and cheap processing method which introduces nanoparticles into porous electrodes, on both anodic and cathodic sides [27-29, 31-36]. The infiltration setup in our work is shown below in Fig. 7, performed under vacuum. However, much of the work has been performed with respect to infiltrating metal catalysts into a single ceramic phase electrode; although these infiltrated SOFCs show much better initial performance compared to pristine samples, prolonged operation causes rapid cell degradation and loss of the improved performance [36-38]. This is attributed to the infiltrated electrocatalyst particles coarsening and unable to maintain a stable connected metal network on top of the scaffold, resulting in loss of connected TPBs over time. As nickel is known to have high electrocatalytic activity, good chemical stability with YSZ in reducing environments and is relatively cheap, the study of nickel infiltration into composite Ni-YSZ cermet electrodes is still of relevant interest to improving overall cell performance. Here, the infiltrant does not introduce any new chemical compositions into the composite scaffold, allowing improvement of performance to be directly correlated to the introduction of particles with smaller feature size and the increase in electrochemically active reaction sites, and not the increase in electrocatalytic activity due to the introduction of a new catalyst.

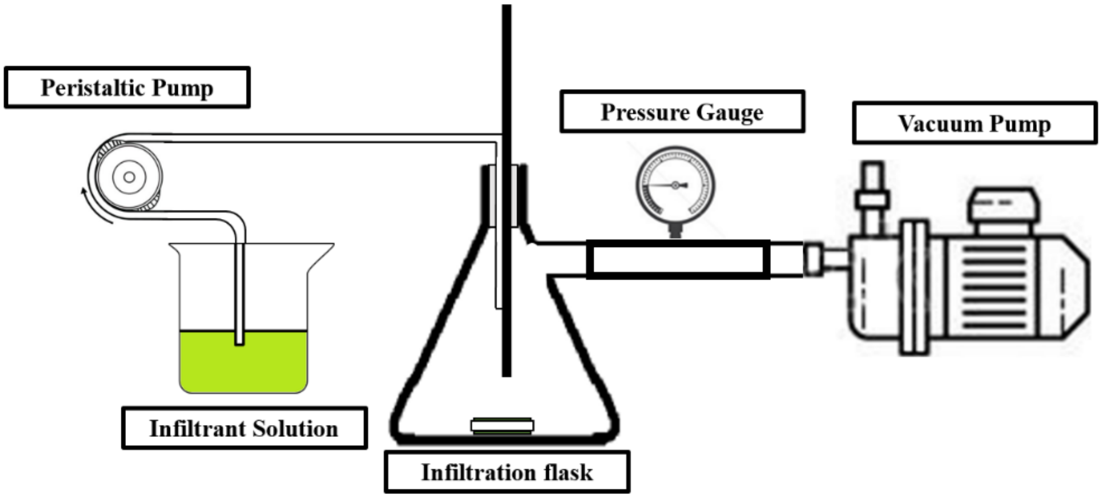

Figure 7: Schematic of the cell infiltration setup.

2.1.5 Mixed Ionic and Electronic Conducting phases within anode layer materials

Another direction in improving SOFC anode performance is the introduction of MIEC phases in the AAL. Although infiltrated nickel nanoparticles do improve anode performance in SOFCs, they face drawbacks over long operations. As these nanoparticles have high surface energy, the thermodynamic loss of free energy leads to agglomeration and coarsening of the nanoparticles, decreasing the overall TPB density and thus the electrochemical reaction sites. Another disadvantage is that although nickel nanoparticles deposit onto the Ni-YSZ scaffold, the nanoparticles all form hemispherical deposits on the YSZ grains. Although isolated grains do increase both reaction sites and TPBs, isolated TPBs have no electronic pathway to the bulk metal scaffold. The electrons released from the Hydrogen Oxidation Reaction have nowhere to go, leaving the half-reaction in equilibrium and rendering the reaction site “inactive”. In other words, liquid infiltration of nickel randomly deposits nickel nanoparticles onto a scaffold, where only some participate in the overall cell reaction; the overall infiltration solution is not fully utilized.

To address this, the introduction of an MIEC material into the AAL was explored. MIECs transport both electrons/holes and ions. The MIEC allows isolated TPBs formed from nanoparticle deposits to become electrochemically active sites as electrons traverse through the connected MIEC phase to the bulk metal scaffold. In this work, MIEC phases that have been explored include infiltrated GDC and co-infiltrated Ni-GDC as a solution to connect isolated nickel phases and suppress the coarsening of nickel grains and nanoparticles. The other pathway explored for incorporating MIECs into the active layer is introducing minority electron charge carriers into the ionic scaffold of the AAL. This is done by doping a transition metal (e.g. Ti or Fe) into the YSZ. Although doping with a transition metal has the potential to decrease the ionic conductivity there by increasing the ohmic polarization associated with the electrode, the increase in minority electronic charge carriers throughout the entire scaffold should essentially allow all nanoparticles to become electrochemically active, and more fully utilize all of the infiltrated electrocatalyst particles.

2.1.6 Modelling the infiltrated symmetric cells using an equivalent circuit

Although EIS is one of the most promising methods for understanding complex electrochemical systems, it is imperative to relate the impedance data to the individual polarization processes as described above, which control the cell performance. One of the methods used to better understand the physical origin of these processes is through the construction of an Equivalent Circuit Model (ECM), allowing meaningful physical parameters to be represented as different circuit elements, each with their own effect on the impedance spectra. The selection of different parameters is deliberate and necessary to accurately fit the electrochemical data and allow a more meaningful mechanistic analysis, which has been the subject of substantial work in the field [24,25]. Although the EIS spectra can be fit with an infinite set of circuit elements, by fitting the spectra with three to five components, it becomes much simpler to deduce and analyze which element is associated with which physical process. In addition to ECM architecture, the DRT transformation has also been employed in many recent works to better identify the more subtle cell processes found in EIS datasets [16, 39, 40].

To evaluate cell performance, DRT analysis was performed on the acquired EIS spectra. In general, a decrease in the magnitudes within DRT spectra is correlated with lower polarizations found within the cell. The spectra also show significant “peaks” at certain frequencies, which is the total resistance due to physical processes occurring at those frequencies. By associating the various reactions to these timescales, the spectra can associate physical processes with the DRT peaks, allowing a better ECM to be fit to the acquired EIS, bridging the gap between the simulated and experimental data. The caveats behind DRT analysis include the high sensitivity to the EIS data acquired, and the smoothing of the DRT transformation, which can produce a variety of different results from the same dataset [26, 39-42].

2.2 Problem Statement

Although it has been shown through other studies that infiltration of electrocatalysts can improve a cell's initial performance, it is not clear which kinetic processes are affected (made more facile) through infiltration. Further, by increasing the number of cycles of infiltration and thus the amount of infiltrated electrocatalysts, the porosity of the electrodes is decreased. Thus there is a tradeoff between introducing new TPBs and thus a larger number of sites for electrochemical reaction and a decrease in activation (or charge-transfer) polarization, and an increase in concentration polarization due to reduced porosity. If the kinetic steps can be identified and tradeoff point identified, a practical goal can be achieved, i.e. determination of the optimum amount of infiltrated electrocatalysts. Thus studying the electrochemical effects of infiltration and the tradeoff between charge transfer and concentration polarization through infiltration studies is the motivation for this work.

Another objective of this work is to better utilize the infiltrated electrocatalysts. The other disadvantage with infiltrated metal electrocatalysts is the coarsening they experience when in close proximity with other metal phases. The goal of this research is to improve connectivity of the infiltrated nanoparticles while also keeping them more isolated from one another. If more active electrochemical sites are present with fewer cycles of infiltration, this could potentially reduce the rate of coarsening, allowing the cermet anode to maintain higher performance for longer operating lifetimes.

3. ENHANCEMENT OF ELECTROCATALYSIS THROUGH NANOPARTICLE INFILTRATION INTO NI-YSZ CERMET ANODES FOR SOLID OXIDE FUEL CELLS

3.1 Abstract

The infiltration of nanoparticle electrocatalysts into solid oxide fuel cell (SOFC) electrodes has been proven to produce a high density of electrochemically active sites, and reduce charge transfer polarization losses for SOFC electrodes. This is crucial for intermediate temperature operation, as these losses increase greatly at lower temperatures. Nickel-yttria stabilized zirconia (Ni-YSZ) cermets are low-cost, and exhibit excellent stability, but their main disadvantage stems from nickel coarsening and performance loss over their operational lifetimes. Infiltration of electrocatalyst nanoparticles has been shown to mitigate nickel coarsening and the consequent anode degradation. In this study, the effects of these infiltrants are observed in a standard Ni-YSZ electrode. In addition to nickel, mixed ionic and electronic conducting (MIEC) phases were infiltrated into Ni-YSZ scaffolds and their performances were characterized using electrochemical impedance spectroscopy (EIS). Cross-sectional microscopy of fractured cells was used to compare electrode microstructure and particle statistics. A model is proposed for how the nanoparticle electrocatalysts improve the anode performance.

3.2 Introduction

High temperature SOFCs operating over long timescales have been observed to experience extreme phase coarsening and instability by end-of-life. Operation at a lower temperature allows broader materials selection as well as slower cell degradation rates [5,43-48]. Previous work has shown that while lower operating temperatures do slow degradation kinetics, the electrocatalytic activity of the cell becomes sluggish as well, leading to larger charge transfer polarization [49,50]. Thus, it is imperative to address the larger charge transfer polarization at lower temperatures to maintain high performance. One direct way to decrease charge transfer polarization in the electrodes is to increase the number of electrochemically active sites in the electrodes [17].

Liquid phase infiltration of nanoparticle electrocatalysts into porous substrates has been shown to be an effective method to improve SOFC electrodes and subsequent cell performance. Some electrocatalysts help decrease feature size within the cermet scaffolds, provide new electrochemical sites, and reconnect isolated grains within the scaffold. Alternatively, other electrocatalysts can improve the SOFC tolerance to contaminants in the reactant gases [10,17,51,52]. Both of these infiltrant functions can reduce polarization resistance in the electrodes, especially at lower operating temperatures. Previous works have also employed metal infiltration into YSZ skeletons, and have also addressed anode connectivity issues [53-55]. In the present work, since electrocatalysts have been infiltrated into a pre-existing Ni-YSZ scaffold, connectivity issues are not as relevant as the in the work of Gross et al [53], McIntosh et al [54] and Costa-Nunes et al [55].

Ni-YSZ cermets have long been state-of-the-art anode electrodes in SOFCs due to their improved performance and stability at high temperatures. Previous work has shown that infiltration of nickel within Ni-YSZ networks can improve cell performance by increasing the TPB length with the introduction of nickel nanoparticles [14,52,56]. Separately, GDC has also been used as an infiltrant due to its MIEC conductivity in reducing environments, showing significant improvements in cell performance for GDC-infiltrated scaffolds [57-59]. In this work we demonstrate how repeated cycles and different infiltrant solutions affect Ni-YSZ electrode performance using symmetric cells. Results show that multiple infiltration cycles initially improve cells; however, further increasing infiltration cycles lead to diminishing returns, i.e. the performance improvement either levels off or worsens with additional cycles. Possible reasons for the polarization improvements are also explored.

MIECs have been shown to improve overall cell performance as an infiltrant, but not as an electrode's ionic phase. In other words, imparting MIEC characteristics into the YSZ ionic phase should increase polarization of the cell, since by imparting larger electronic conductivity into YSZ requires decreasing the ionic conductivity of YSZ as well. However, the previous observation has not considered the infiltration of electrocatalysts which would increase not only the TPB density, but also expansion of the TPBs into triple phase zones (TPZ) as seen in analogous work on SOFC cathodes [60].

In this manuscript we present and interpret electrochemical measurements using EIS on symmetric Ni-YSZ/YSZ/Ni-YSZ cells. The variables examined are the infiltrants, number of infiltration cycles and operating conditions. Additionally, this work presents how the ionic conducting phase of the AAL interacts with electrocatalyst infiltration and its effect on cell performance. The use of symmetric cells allows isolation of the anode charge transfer processes from not only oxygen electrode processes found in full cells, but also the anode concentration polarization due to the thickness of the anode support. Microstructural characterizations of pristine and tested cells, equivalent circuit diagrams, and the DRT analysis are compared to elucidate how infiltration improves the polarization processes of the cell.

3.3 Experimental and Analytical Approach

3.3.1 Materials synthesis

A Titania-doped YSZ (TiYSZ) ionic phase was formed in solid state solution by calcining 3% TiO_2 doped into YSZ. This was done by mixing the appropriate precursors in ethanol and ball milling the resulting slurry. The slurry was dried and calcined at 700°C in air for 9 hours. X-ray diffraction (XRD) of powder samples indicate peak shifts of TiYSZ compared to YSZ without Ti doping, indicating complete incorporation of TiO_2 into the YSZ lattice. The TiYSZ was used in place of YSZ as the ionic conducting phase in the AAL in some subsequent experiments.

3.3.2 Cell fabrication

The anode slurry consisted of a 50-50 weight ratio of NiO-YSZ (J. T. Baker, Tosoh) with V6 (Heraeus) as binder and LP1 (Croda) as dispersant dissolved in alpha-terpineol (Alfa-Aesar). Symmetric cells were fabricated by screen printing the cermet (Ni-YSZ or Ni-TiYSZ) onto commercially purchased 8YSZ electrolyte substrates (Fuel Cell Materials) and sintered at 1400°C for 2 hours. Cells were then reduced at 800°C under humidified forming gas for 7 hours to reduce the NiO to nickel. The reduction step increases the porosity of the scaffold and allows easier infiltration of nanoparticles. The 3 M infiltration solutions containing nickel or GDC were prepared by dissolving precursors containing $Ni(NO_3)_2$ or $(Gd(NO_3)_3)_{0.1}(Ce(NO_3)_3)_{0.9}$ in 50 mL of ethanol at 90°C, respectively. The 3 M Ni-GDC nitrate solution was similarly prepared by adding the nitrate precursors that results in a 1:1 molar ratio of Ni to GDC into an ethanol solvent. The infiltration procedure involved saturating each electrode with infiltrant solution under vacuum. After each round of infiltration, the cells were heated to 320°C to evaporate the solvent and decompose the nitrate salts into metal oxides. This intermediate heating step was necessary as it reopens the pores for additional infiltration. The processing variables studied include (i) the number of infiltration cycles, (ii) the infiltrated electrocatalyst material and (iii) the ionic conducting phase in the AAL. Group A represented cells comprising Ni-YSZ scaffolds, while Group B represented cells comprising Ni-TiYSZ scaffolds. Groups 1, 2, and 3 represented cells infiltrated with metal nitrate solutions which decomposed to result in infiltrants of Ni, GDC, or Ni-GDC, respectively. For example, group A1 represents cells with a Ni-YSZ anode scaffold that was infiltrated with Ni. A visual representation of the cell parameters is shown below in Table 1, including the infiltration cycles tested for each cell group.

Cell Group	**Ni-YSZ electrodes on YSZ supports**	**Ni-TiYSZ electrodes on YSZ supports**
1.Ni Infiltration	**A1(0-5)**	**B1 (0-2)**
2.GDC Infiltration	**A2 (0,1)**	**N/A**
3. Ni-GDC Infiltration	**A3 (0,1)**	**N/A**

Table 1: Cell group nomenclature to distinguish different cell tests.
Numbers in parenthesis indicate number of infiltration cycles.

3.3.3 Electrochemical testing

Nickel meshes were affixed with nickel paste onto both electrodes of the symmetric cell as electrical contacts. Nickel wire was used as voltage and current leads for the cell and the entire device was placed in a single chamber setup. All cells were heated to 800°C under humidified forming gas to prevent the re-oxidation of nickel. Forming gas was first passed through a bubbler at 25°C to achieve a total flow rate of 300 mL/min (92%N_2/5%H_2/3%H_2O) and fed into the electrochemical test chamber. EIS was performed from 600°C to 800°C under a total gas flow rate of 300 mL/min and gas compositions of 3% and 50% H_2O, and balance hydrogen**.** The desired chamber gas composition was obtained by changing the bubbler temperature. Flow rates into the test chamber were maintained at 300 mL/min. The furnace temperature and water bubbler temperature were both monitored before commencing electrochemical measurements. The cell was equilibrated for 30 minutes after reaching target operating conditions. EIS spectra were acquired using a Parstat 4000 workstation with a frequency sweep of 10^5-10^{-1} Hz with a

50mV RMS perturbation. Equivalent circuit models were fit using R-RQ-RQ circuit based on previous work to isolate and identify the main polarization processes [49,50,57]. These processes were correlated with the spectra's DRT to compare process time constants and magnitudes.

3.3.4 Scanning Electron Microscopy (SEM)

Pristine and tested symmetric cells were fractured and their cross sections were coated with 10nm of Au and contacted with copper tape. The electrodes were imaged using a Zeiss Supra 55 SEM at 15kV using an In-lens detector at 6-8mm working distance to obtain nanoparticle deposition and morphologies from fractured cross-sections. Other cross-sections were also vacuum infiltrated with epoxy and polished to compare overall cell porosity and microstructure.

3.3.5 DRT analysis

The DRT is obtained from convolving EIS data into the time domain, obtaining peaks which are proportional to the cells' polarization resistances centered around different timescales. More information can be found in work by Leonide et. al [49]. The equivalent circuit model is used to sharpen the DRT analysis to further elucidate how the kinetics of the various electrochemical processes in the electrodes change with infiltration and different operating parameters.

3.4 Results and Discussion

3.4.1 Electrochemical characterization of Ni-infiltrated cells

Fig. 5 shows the Nyquist plots, corrected for ohmic resistance, of A1 cells with varying infiltrant cycles under 3% humidity (balance hydrogen) at 800°C and 700°C. From the Nyquist plots, infiltration appears to improve cell performance, as seen from the decreasing polarization resistance; these are the magnitudes of the low frequency intercepts on the Nyquist plots. However, multiple infiltration cycles result in diminishing improvements, eventually stagnating overall cell performance. Additionally, infiltration of nickel appears to impart greater cell improvements at lower temperatures. Fig. 8 compares relative polarizations of different A1 cells at different operating conditions. In this work, relative polarization is the ratio of the cell polarization when compared to the group's baseline uninfiltrated cell, under identical test conditions. Although all cells showed improvement under all operating conditions after infiltration, there is an optimal number of infiltration cycles (around 3 or 4 in Ni-infiltrated Ni-YSZ) before additional cycles begin to increase polarization resistance. However, all infiltrated A1 cells showed a more modest level of improvement over the uninfiltrated cell at 800°C and 50% humidity compared to other test conditions, implying that infiltration is most effective at lower temperatures and lower humidity levels in the fuel. This is in line with the general observation that at higher temperatures and humidity conditions, all charge transfer processes are more facile. This is also in accord with observations in prior work [61] and will be discussed later in this chapter.

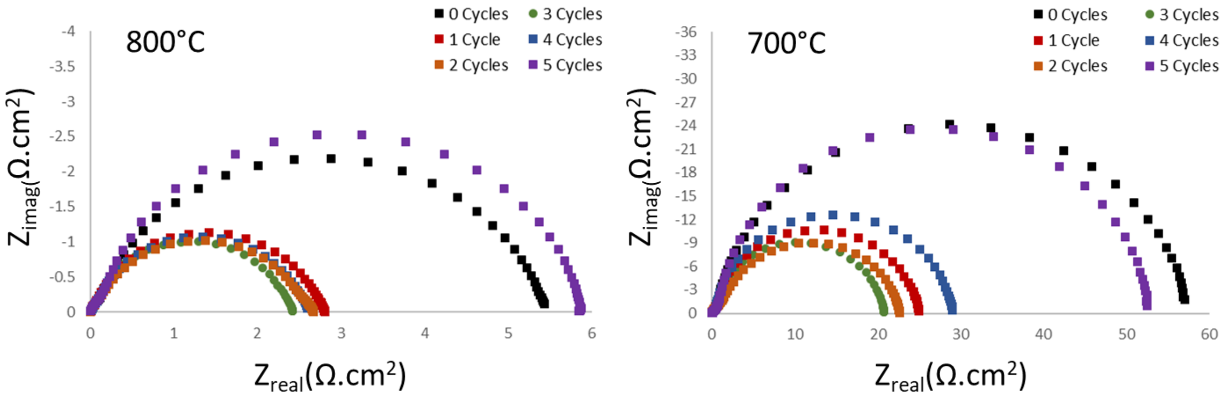

Figure 8: Nyquist plots of symmetric cells as a function of number of infiltration cycles of nickel at 3% humidity and 800°C (left) and 700°C (right).

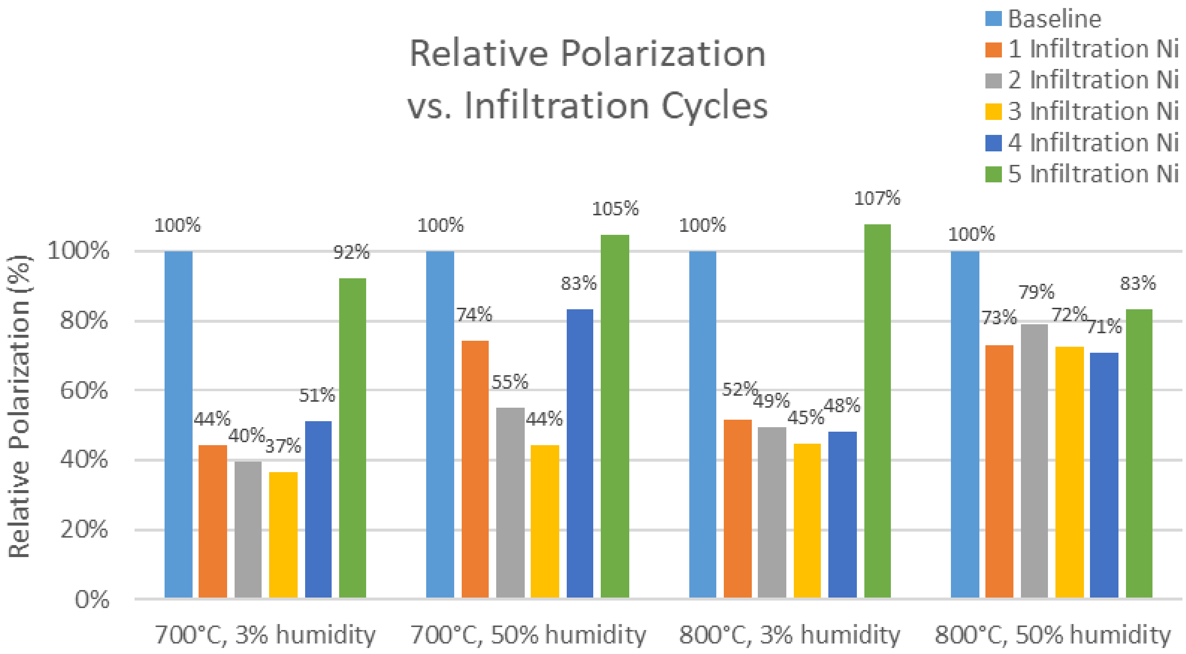

Figure 9: Relative polarization resistances of Ni-YSZ symmetric cells (A1) with respect to different infiltration cycles of $Ni(NO_3)_2$ under different operating conditions.

Fig. 10 shows the relative polarizations of B1 cells under the same operating conditions as above. Infiltration improves overall cell performance, however, the optimal number of nickel infiltration cycles is one for Ni-TiYSZ scaffolds. Under all test conditions, one cycle of infiltration shows significant improvement over the baseline cell without the need for additional infiltrations. Fig. 11 compares the A1 and B1 cells' relative polarizations, showing uninfiltrated and optimally infiltrated cells with the uninfiltrated A1 cell as the baseline. The increase in polarization resistance for the Ni-TiYSZ scaffold indicates that the cermet alone performs worse than Ni-YSZ cermets, yet infiltration allows the Ni-TiYSZ scaffolds to perform on par with Ni-YSZ scaffolds, with even fewer cycles of infiltration.

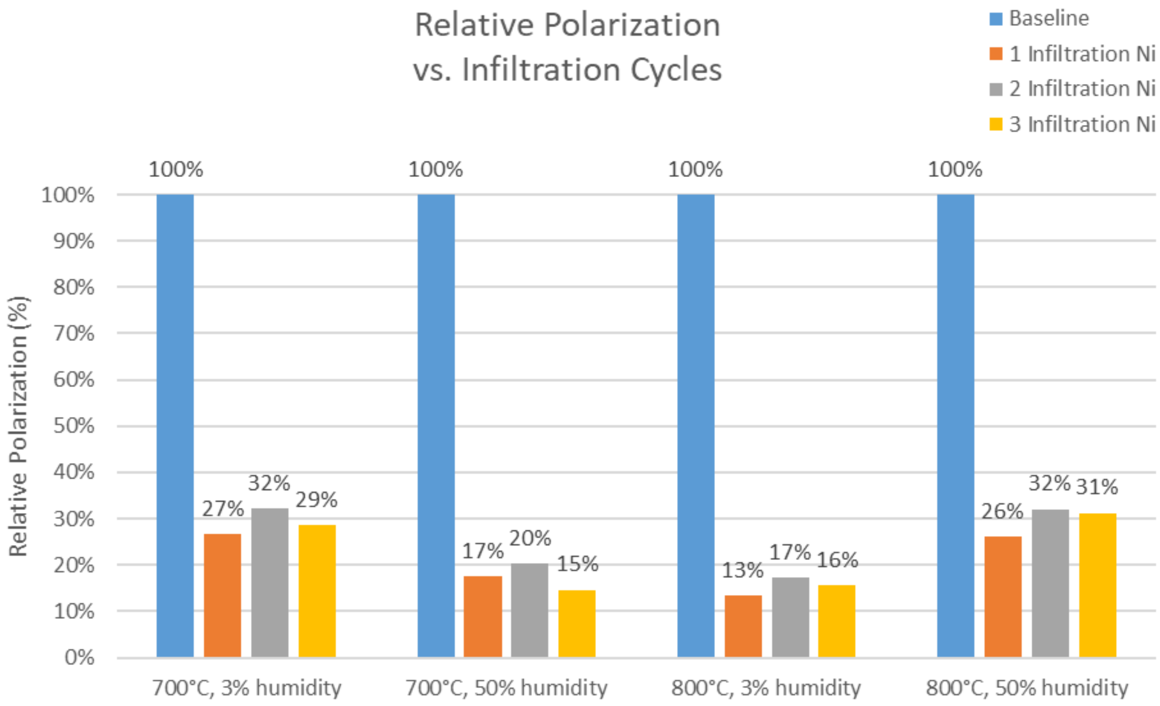

Figure 10: Relative polarization resistances of Ni-TiYSZ symmetric cells (B1) with respect to different infiltration cycles of Ni(NO_3)$_2$ under different operating conditions.

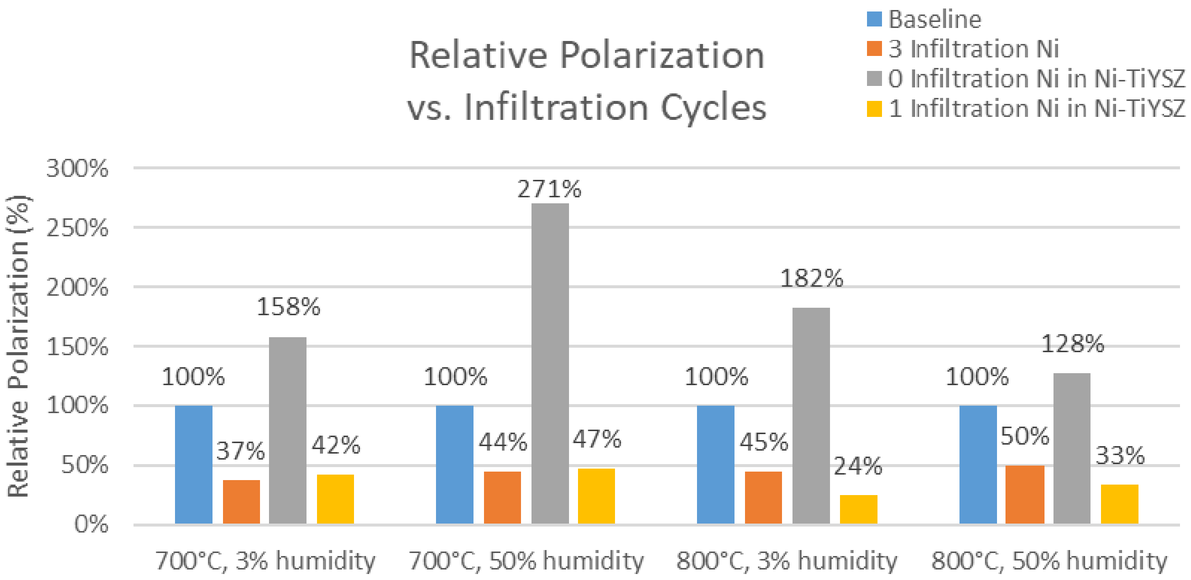

Figure 11: Relative polarization resistances comparing Ni-YSZ and Ni-TiYSZ cells, uninfiltrated and infiltrated with Ni(NO3)2 under different operating conditions.

3.4.2 Electrochemical characterization of GDC and Ni-GDC-infiltrated cells

Table 2 shows total and relative polarizations of GDC and Ni-GDC infiltrated within the Ni-YSZ and Ni-TiYSZ symmetric cells, with a Group A2 uninfiltrated cell as the baseline. For all cells containing any GDC infiltrant, the best cell performance is observed with one cycle of infiltration among all cell groups, with the exception of A3 cells. However, all cells infiltrated with some GDC loading showed an increase in performance by at least one order of magnitude.

Testing Temperature	**AAL cermet composition**	**Infiltrant**	**Infiltration cycles**	**Polarization resistance/Relative polarization resistance compared to uninfiltrated Ni-YSZ (Ω.cm^2/%) under different humidity conditions**	
				3% H_2O – 97% H_2	**50% H_2O – 50% H_2**
800°C	Ni-YSZ	N/A	0	5.48/100%	1.95/100%
		Ni	3	1.21/22.1%	0.97/49.7%
		GDC	1	0.32/5.9%	0.02/0.9%
		GDC	2	0.36/6.6%	0.02/1.1%
		Ni-GDC	1	0.21/3.8%	0.01/0.6%
		Ni-GDC	2	0.21/3.8%	0.02/0.8%
	Ni-TiYSZ	Ni	3	1.56/28.5%	0.78/40%
700°C	Ni-YSZ	N/A	0	56.91/100%	10.57/100%
		Ni	3	20.8/36%	4.69/44%
		GDC	1	0.86/1.5%	0.22/2.1%
		GDC	2	1.25/2.2%	0.12/1.2%
		Ni-GDC	1	0.27/0.5%	0.12/1.2%
		Ni-GDC	2	0.42/0.7%	0.16/1.5%
	Ni-TiYSZ	Ni	3	25.69/45%	4.14/39%

Table 2: Total and relative polarizations resistances of Ni-YSZ and Ni-TiYSZ cells infiltrated with Ni, GDC and Ni-GDC electrocatalysts, compared to a baseline cell under different operating conditions.

3.4.3 Microstructural analysis

Fig. 12 shows SEM fractured cross-sections of nickel-infiltrated A1 cells. The bottom right number indicates the number of infiltration cycles. On infiltrated cells the infiltrated nanoparticles appear hemispherical and can be seen on the ionic conducting phase, i.e. YSZ or TiYSZ. Although initially infiltration increases nanoparticle density on the scaffold, it appears that the density decreases with additional infiltration cycles, and instead nanoparticle size increases, indicating coarsening of the infiltrated phase. Previous work in our group has shown that although NiO can deposit on the entire Ni-YSZ scaffold, during the reduction process, any Ni deposited on bulk Ni will form a thin film on said bulk phase due to zero surface energy between Ni and Ni [56]. In other words, all rounded Ni nanoparticles are only found to be deposited on the YSZ surface. Secondary electron SEM images presented in Fig. 9 from our prior work [56] clearly show this.

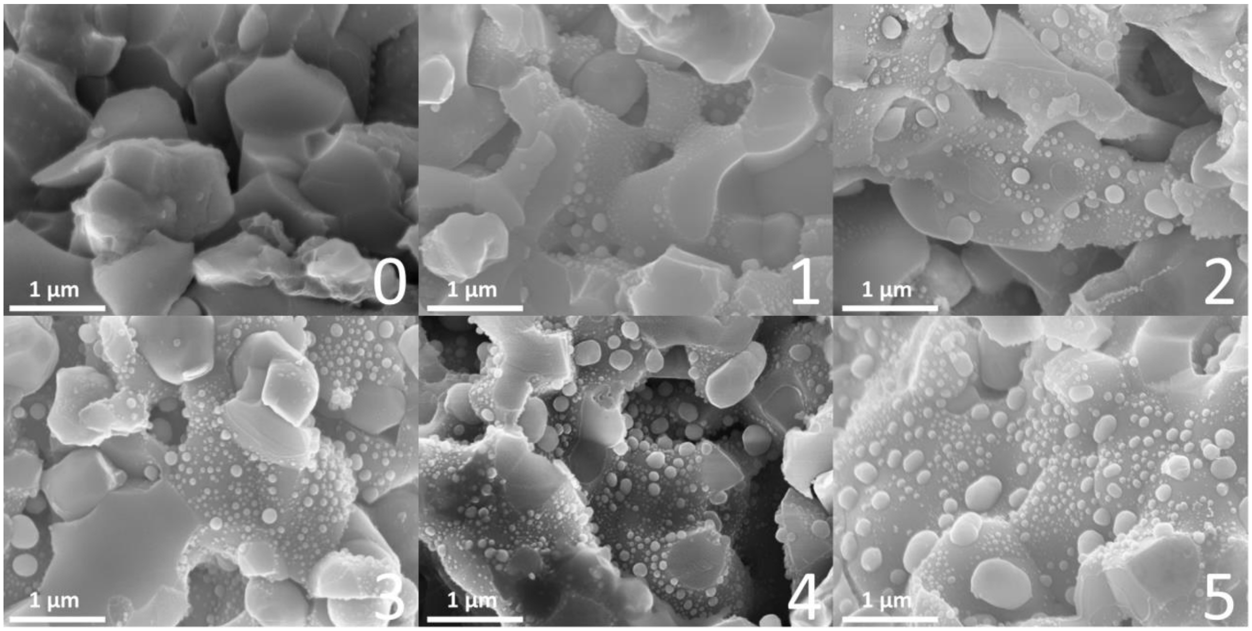

Figure 12: SEM fracture cross-sections at 40k magnification of the Ni-YSZ cells infiltrated with nickel nanoparticles. Cycles of infiltration are shown on the bottom right of each image.

Fig. 13 shows the SEM cross-sections of GDC and Ni-GDC infiltrated A2 and A3 cells. As before, the number on the bottom right corner indicates the number of infiltration cycles. The GDC morphology is drastically different from Ni nanoparticles. The GDC phase appears to form a thin yet porous film over both the Ni and YSZ phase of the Ni-YSZ scaffold. The Ni-GDC morphology also appears to form a porous thin film on the scaffold, but with more porosity than the GDC infiltrant. This may be due to the infiltrated nickel coalescing into the bulk metal phase to reduce surface energy, and reducing the overall GDC nanoparticle loading. This hypothesis also would explain why nickel infiltration in experiments described earlier showed an absence of nanoparticles deposited on nickel surfaces.

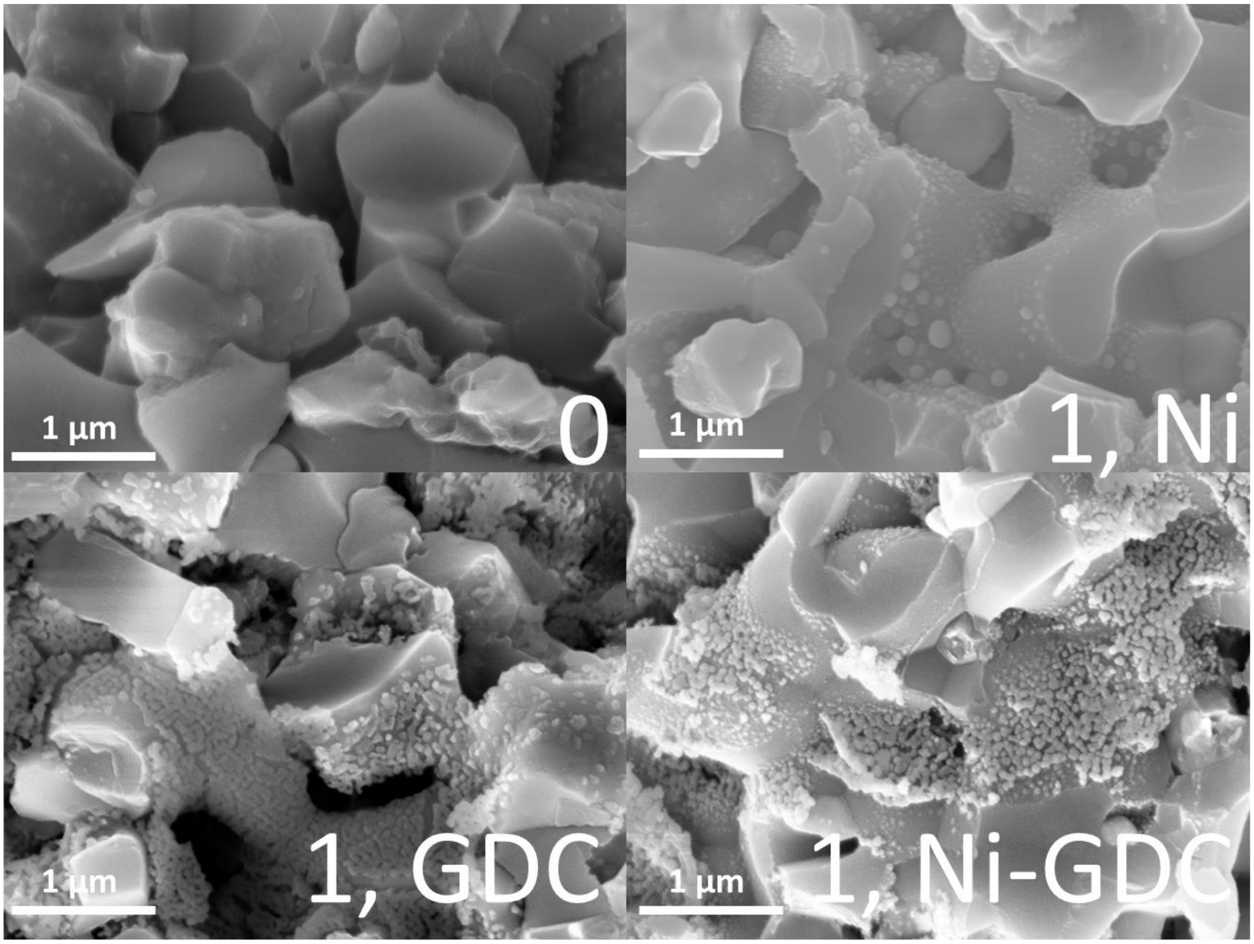

Figure 13: SEM fracture cross-sections 40k magnification of the Ni-YSZ cells infiltrated once with Ni, GDC and Ni-GDC nanoparticles.

3.5 Discussion

3.5.1 Electronic pathways in the active layer

The infiltration of nanoparticle electrocatalysts is expected to improve the cell performance through the introduction of phases with higher surface-to-volume ratios, and increasing the overall

TPB length thereby increasing the overall density of reaction sites in the electrode. However, SEM cross-sections show that many nickel nanoparticles do not make contact with the bulk Ni in the Ni-YSZ scaffold, yet still result in improved performance as seen by the lower polarization resistance in infiltrated scaffolds.

There are two possible mechanisms that could explain this behavior. The first is that all TPBs where they are formed between isolated Ni particles, YSZ, and the pore phase can be active over a certain distance away from the actual TPB line. Thus the TPB line should really be thought of as a three phase zone (TPZ). Depending on the infiltrated particle density, these TPZs can overlap and enable isolated nickel particles to be electrochemically active. This has been observed in Horita's work on the cathodic side [60].

The second possible mechanism for isolated nickel nanoparticles to contribute to electrochemical reaction involves electronic transport through the predominantly ionic conducting phase in the anode active layer, namely YSZ. Even if the deposited particles were farther away from the metal (Ni) phase in the scaffold, the ionic phase with minority electronic charge carriers can shuttle electrons to the bulk percolated metal (Ni) network. YSZ doped with TiO_2 is known to possess a higher electronic conductivity than YSZ [62-65]. When the B1-group of cells are infiltrated with Ni nanoparticles, they performed as well as the A1 cells with a lower number of infiltration cycles, thereby providing evidence for the second mechanism.

The latter pathway is applicable to GDC infiltrated cells as well. The GDC electronic conductivity is much greater than that of the cermet's ionic phase, greatly extending the TPZs as the infiltrant morphologies cover both nickel and YSZ grains. Previous work has shown that GDC infiltrated into Ni-YSZ symmetric cells has been shown to significantly improve anode charge transfer [57-59]. Whereas in these papers GDC infiltration results in hemispherical particles deposited onto the scaffold, the GDC in this work results in a porous film on the scaffold. Additionally, the infiltration of GDC has been found to reduce the polarization resistance in Ni-YSZ scaffolds by around 95%. It is evident that GDC is a much better electrocatalyst than Ni especially at high humidity levels in the fuel. Presumably its excellent mixed conductivity under SOFC anode conditions also plays a role in obtaining very low polarization resistances.

3.5.2 Effects of humidity on nanoparticle electrocatalysts

In addition to the 3% humidity condition, a 50% humidity condition was also tested to observe the effect of infiltrated nanoparticles under varying humidity conditions. As shown in Table 2, infiltration appears to improve the cell performance by decreasing the polarization resistance under both the humidity conditions tested. However, GDC infiltration appears to greatly decrease the polarization resistance under both humidity conditions under which the cells were tested. The mechanistic reasons for the dramatic decrease in polarization resistance in GDC infiltrated electrodes and the behavior as a function of gas composition are still being explored.

3.5.3 Limits to nanoparticle infiltration

As discussed above, infiltration has improved cell performance, but multiple infiltration cycles result in diminishing improvements in performance and eventually increase the cell polarization resistance. A DRT analysis of the EIS spectra showed that two main polarization processes contributed to the charge transfer of the cell. Fig. 14 compares the DRT analysis performed on EIS spectra obtained from infiltrating of A1 cells at 700^{o}C and 50% humidity. The DRT analysis suggests the presence of a high frequency (HF) response at ~2000 Hz and medium frequency (MF) response at ~100 Hz. These processes are attributed to charge transfer occurring at electrochemically active sites such as the TPBs, and oxygen vacancy transport, respectively

[59]. Infiltration appears to initially decrease the magnitude, and increase the frequency of these processes; this suggests the presence of nanoparticles decreases the polarization resistance and increases the rate of electrochemical reactions. However, the addition of further infiltration cycles led to smaller improvements in peak processes. In fact, after four infiltration cycles, the peaks revert to higher magnitudes and lower frequencies, suggesting an inversion in cell performance.

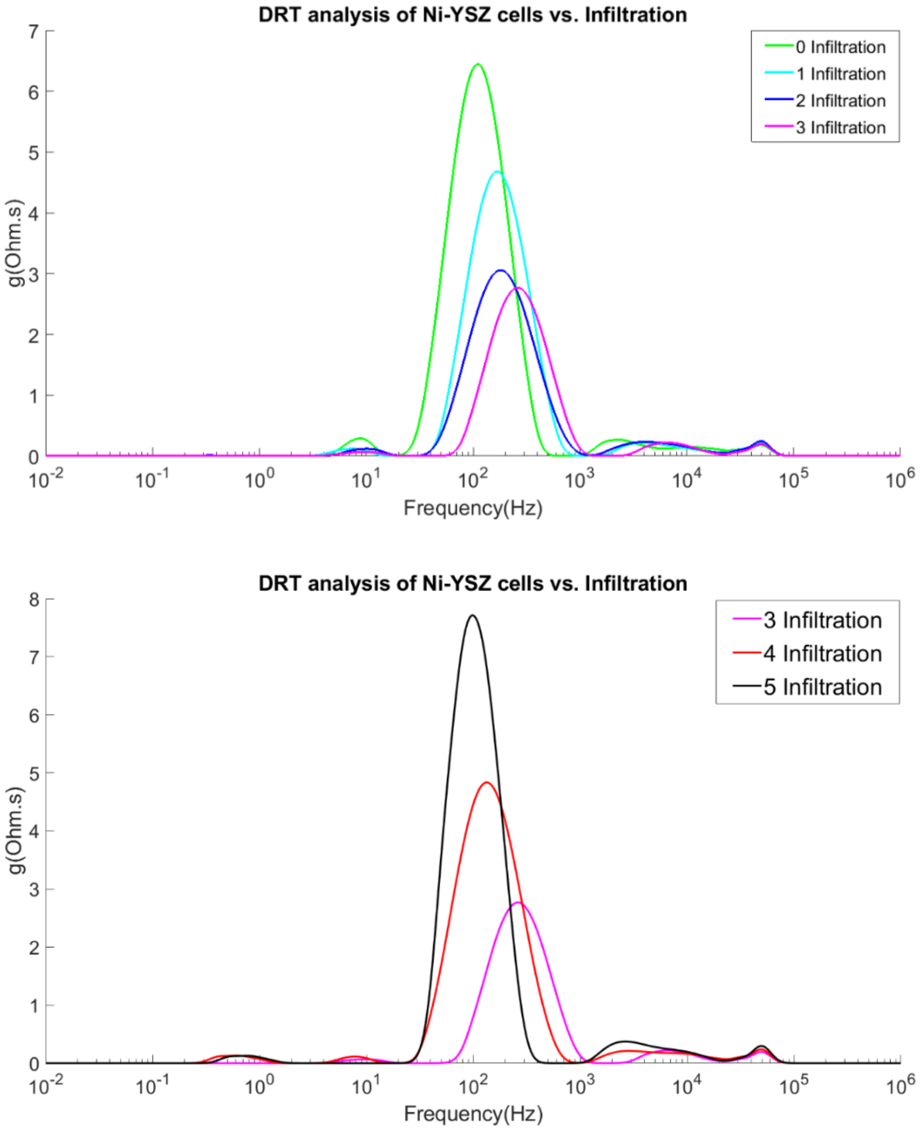

Figure 14: DRT analysis showing improvement of the cell performance of group A1 cells at 700C, 50% humidity with increasing infiltration cycles of nickel (above) and subsequent inversion with additional infiltration cycles(below)

The explanation for this behavior is that the first nickel infiltration cycle deposits the first nanoparticles onto the YSZ grains, most of which range from 5-50 nm in size. This infiltration cycle introduces a high nanoparticle density in the electrode scaffold, resulting in a high TPB density. Although additional infiltration cycles do increase the nanoparticle density, some particles are in close enough proximity to coalesce. As $Ni(NO_3)_2$ deposits onto pre-existing nanoscale NiO particles rather than the ionic conducting phase, the infiltrant loading increases the Ni nanoparticle sizes and aggregates previously isolated Ni particles. The increasing size of the nanoparticles at higher number of infiltration cycles also decreases TPB density and average particle surface-to-volume ratio. The inversion in polarization resistance can be attributed to the overall increase in average nanoparticle size and the decrease in nanoparticle density.

3.5.4 Effect of GDC loading on Ni-YSZ cells

As in the case of Ni-infiltration, infiltration of GDC nanoparticles improves cell performance by decreasing feature sizes and increasing electrochemically active sites; the electrocatalyst appears to dramatically decrease the cells' polarization resistance (by 95%) as seen in Table 2. The DRT analysis of GDC-infiltrated cells in Fig. 15 shows almost complete suppression of the main HF and MF polarization peaks. The remaining peaks are seen around 6000 Hz and 40000 Hz. This is seen not only in GDC-infiltrated cells, but in Ni-GDC-infiltrated cells as well. It is unknown whether these remaining peaks are due to processes that were eclipsed by the main charge transfer processes in Ni-YSZ cermets, or if the peaks are attributed to new processes related to the infiltrated GDC electrocatalyst in the Ni-YSZ scaffold.

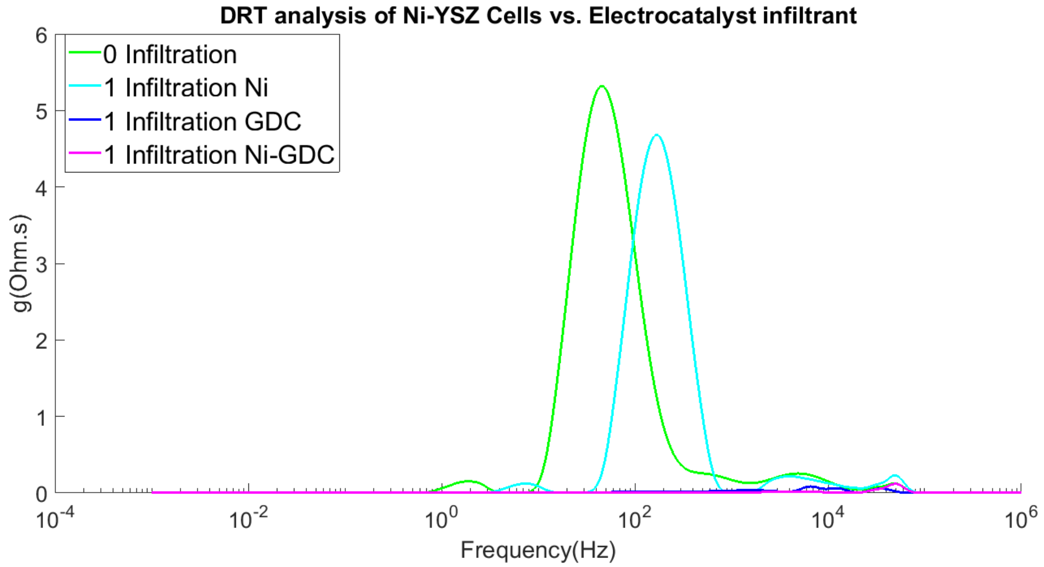

Figure 15: DRT analysis showing varying infiltrants of Ni, GDC and Ni-GDC versus a baseline cell.

3.6 Conclusions

Ni-YSZ cermet anodes on electrolyte supported symmetric cells were infiltrated with nanoparticle electrocatalysts to improve the electrocatalytic performance of the anode. Aqueous solutions of metal nitrates were repeatedly infiltrated into the reduced Ni-YSZ thin electrodes on symmetric cells and said cells were electrochemically tested under EIS. Fractured cross-sections showed hemispherical individual nickel particles deposited on YSZ grains, while GDC-infiltration resulted in a thin, porous, film covering both nickel and YSZ grains. The effects of infiltration were also compared by observing changes in the DRT analysis of the EIS spectra of the cells.

Despite nickel nanoparticles not physically contacting the metal network, infiltrated cells exhibited a decrease in polarization resistance under almost all operation conditions tested. Cells were also exposed to a maximum of 50% humidity, well below the threshold for critical nickel wetting on YSZ surfaces. In other words, nanoparticles contributed to the faradaic reaction in the electrodes due to the close proximity to the metal network, either through the active and overlapping region of TPBs of the infiltrated nanoparticles and bulk metal phase or electronic transport in the ionic phase.

These experimental results also show the addition of GDC suppresses the main charge transfer peaks in the EIS spectra of cells with Ni-YSZ scaffolds, greatly improving the performance of the cells. The remaining polarization peaks appear to be high frequency processes, but it is unknown if these peaks are present due to the GDC or if they only appeared due to the suppression of these peaks in cells with pristine Ni-YSZ scaffolds.

4. THE ROLE OF MIXED IONIC AND ELECTRONIC CONDUCTION IN ANODE ELECTROCATALYSIS

4.1 Abstract

Mitigating activation polarization in the anode is one of the major challenges in intermediate-temperature operation of solid oxide fuel cells (SOFCs). Liquid phase infiltration of nanoscale electrocatalysts has been shown to result in significant reductions in activation polarization in SOFC anodes. In this study, we explore liquid-phase infiltration of nickel, GDC, and Ni/GDC electrocatalysts into two different types of cermet anodes: one with a conventional Ni-YSZ composition, and the other with a Ni-MIEC cermet anode where the YSZ has been doped with 3 mol% TiO_2 to impart electronic conductivity. The principal goal of this study is to explore the role of electronic transport in the MIEC phase in effective utilization of the infiltrated nanoscale electrocatalysts. The role of temperature, infiltration cycles and the type of electrocatalysts have been experimentally studied in symmetric cells using EIS. DRT analysis has been used to elucidate the contributions of various charge transfer processes.

4.2 Introduction

The broad adoption of SOFC power systems to address our need for clean energy requires improved metrics of the current state-of-the-art systems, including lower cost, and higher durability and performance [43,45,48]. Although conventional nickel-yttria stabilized zirconia (Ni-YSZ) cermet anodes perform well at 800°C, their performances start to degrade at lower temperatures because sluggish charge transfer processes begin to dominate the overall polarization [49].

The polarization losses most commonly found in SOFC systems are divided into three categories; activation polarization, ohmic polarization and concentration polarization. At lower temperatures, activation polarization is the largest contributor at low current densities. While concentration polarization is negligible until high current densities are reached (inducing mass transfer limitations), activation polarization and ohmic polarization increase exponentially with decreasing operation temperature. The ohmic polarization, resulting from ionic diffusion through the electrolyte layer, can be minimized by using thin electrolytes. Reducing activation polarization, which is related to the intermediate charge transfer and gas conversion within the electrodes, is more complicated. One approach to combat this is to introduce smaller feature sizes, leading to higher TPB density and thus increasing the total amount of reaction sites in the electrodes [17]. However, in order to increase the overall reaction rate at the anode, the additional TPBs formed by infiltration need to be active, i.e., a connected electronic pathway must exist for the infiltrated electrocatalysts to contribute to the faradaic current and improve cell performance.

Liquid infiltration has been an extensively used method to introduce nanoparticles onto the pore surface of anodes [10,17,52]. The role of these nanoparticles can vary from mitigating sulfur poisoning to improving coking resistance or increasing TPB density by introducing new reaction sites [14,51,52,56]. While liquid infiltration has been used to introduce nanoscale metal catalyst phases into ceramic ionic-conducting electrode scaffolds, their long-term performance was not found to be sustainable due to the coarsening of the metal phase and the resulting decrease of connectivity [53-55]. In recent years, infiltration into percolated Ni-YSZ cermet scaffolds have been employed to retain the advantages provided by the already established ionic and electronic networks [52,59,66,67].

Imparting electronic conductivity to the YSZ phase by doping to create an MIEC phase in the anode can alleviate issues related to the connectivity of the electronic pathways of the additional TPBs produced by infiltration. In prior work we have demonstrated that the additional electronic transport imparted by the MIEC results in reduced polarization resistance [67]. Ni electrocatalysts introduced through liquid infiltration cannot be fully utilized if they are too distant from the metal phase in the Ni-YSZ scaffold. Introducing a small amount of minority electronic charge carriers by doping the YSZ by a transition metal oxide such as TiO_2 led to the formation of Ni-MIEC anode scaffolds. Infiltrating Ni nanoparticles into symmetric cells with Ni-MIEC electrodes improves the performance of cells by making all the added TPBs due to infiltration electrochemically active.

In this study, the role of MIEC phase is explored using two different approaches. In the first approach, metallic and MIEC electrocatalysts were infiltrated by liquid-phase infiltration into conventional Ni-YSZ cermet scaffolds. The second approach consisted of infiltrating metal nanoparticles into Ni-MIEC cermet scaffolds. All cells were characterized by EIS over a temperature range of 700-800°C in a fuel gas composition of 50% humidity (balance hydrogen). Equivalent circuit models were fitted to the EIS data to elucidate how different components of the cell polarization changed under different conditions. Complex nonlinear least squares fitting was performed using a MATLAB^{TM} script developed in this work.

4.3 Experimental and Analytical Approach

4.3.1 Materials synthesis

Mixed ionic and electronic conductivity was introduced into YSZ by adding 3 mol. % TiO_2. A suspension of TiO_2 and 8YSZ powders in the correct stoichiometry was formed in ethanol and ball milled for 24 hours to ensure proper powder mixing. After drying the powders in a drying oven, the contents were calcined at 900°C for 5 hours. Subsequently, the particle size was reduced by SPEX milling for 30 minutes. The Ti-doped YSZ, which is expected to be a MIEC phase, replaced the 8YSZ powder used in conventional anodes. A slurry of Ni and Ti-doped YSZ (henceforth referred to simply as Ni-MIEC) was used to prepare these modified anodes.

Infiltration solutions of 3 M concentration, containing nickel or GDC were prepared by dissolving precursors containing $Ni(NO_3)_2$ or $(Gd(NO_3)_3)_{0.1}(Ce(NO_3)_3)_{0.9}$ in 50 mL of ethanol at 90°C. The 3 M Ni-GDC nitrate solution was similarly prepared by adding the nitrate precursors that results in a 1:1 molar ratio of Ni to GDC into an ethanol solvent. GDC under reducing atmospheres behaves as an MIEC, and is thus an ideal MIEC electrocatalyst for infiltration.

4.3.2 Cell fabrication

Symmetric, fuel electrode/YSZ/fuel electrode cells were fabricated by screen printing fuel electrode cermet slurry onto the surfaces of commercially obtained electrolyte substrates. After the cells were dried and sintered at 1400°C, they were placed in a reducing chamber at 800°C and 50% humidity (balance hydrogen) was circulated in the chamber to pre-reduce the cermet NiO to Ni, and to introduce additional porosity in the microstructure. Aqueous solutions of 3 M Ni, Ni-GDC and GDC were then infiltrated into reduced symmetric cells under vacuum. For samples with multiple infiltration cycles, the cell was heated to 320˚C in air to decompose the nitrate salts without oxidizing the Ni network in the cermet electrodes prior to the next infiltration.

4.3.3 Electrochemical testing

For electrochemical testing of these symmetric cells, Ni meshes were affixed to each electrode. The cell was placed inside a single chamber testing apparatus, and EIS data was acquired from a 700°C to 800°C range in humidified hydrogen under 50% humidity. All spectra were acquired using an Ametek PARSTAT 4000 instrument under open circuit conditions with a 50 mV AC signal in the frequency range 0.1 Hz to 100 kHz.

4.3.4 Scanning Electron Microscopy (SEM)

Processed and tested symmetric cells were fractured, their cross sections coated with 10 nm of Au, and contacted with copper tape. The electrodes were imaged using a Zeiss Supra 55 SEM at 15 kV using an in-lens detector at 6-8 mm working distance to obtain nanoparticle deposition and morphologies from fractured cross-sections. Fracture cross-sections taken from the same cell were also vacuum infiltrated with epoxy, and polished to compare overall cell porosity and microstructure.

4.3.5 DRT modelling

The underlying anodic electrochemical processes were examined by DRT analysis of the acquired EIS spectra. The most optimal model to fit the data was chosen to be the transmission line model (TLM), which simplifies the entire electrode to a single MIEC column [68] (described in earlier work by Nielsen et. al [68]). More recently, Park et. al used this model for cells with GDC infiltrated anodes [66]. Equation 6 and 7 describes the general equation for a TLM element:

$$Z = \frac{R_O R_E}{R_O + R_E}\left(L + \frac{2\lambda}{\sinh\left(\frac{L}{\lambda}\right)}\right) + \lambda\frac{R_O^2 + R_E^2}{R_O + R_E}\coth\left(\frac{L}{\lambda}\right) \tag{6}$$

and

$$\lambda = \sqrt{\frac{\zeta}{R_O + R_E}} \tag{7}$$

In Equation 8, R_O and R_E are the ionic and electronic resistivity per unit length of the cermet electrode (with units $\Omega.\text{cm}^{-1}$), L is the average thickness of the electrode (which is calculated as 25μm for this study), and λ is the AC penetration depth. Prior work by Nielsen et. al has expressed λ as Equation 9 shown above [68]. As the electronic resistivity is much smaller than the ionic resistivity found in the electrode compositions in the tested cermets ($R_E \ll R_O$), the TLM element impedance reduces to:

$$Z_{TLM} = \lambda R_O \coth\left(\frac{L}{\lambda}\right) \tag{8}$$

$$\lambda = \sqrt{\frac{\zeta}{R_O}} \tag{9}$$

4.4 Results and Discussion

4.4.1 MIEC phase formation and electrode microstructure

Fig. 16 shows powder x-ray diffraction (XRD) spectra of the precursors, as well as the pre-calcined and calcined product. The XRD spectrum of the calcined sample shows a shift in YSZ peaks to higher 2θ values, indicating a reduction in lattice parameters. No second phase peaks are observed, indicating complete dissolution of the TiO_2 into the YSZ lattice.

Fig. 17 shows a SEM micrograph of a polished cross-sections of a tested symmetric Ni-YSZ cell next to that of a symmetric Ni-MIEC cell. No significant difference in microstructures was noted between the two cells. We can therefore be assured that the differences in electrochemical performance between cells are not due to microstructural differences.

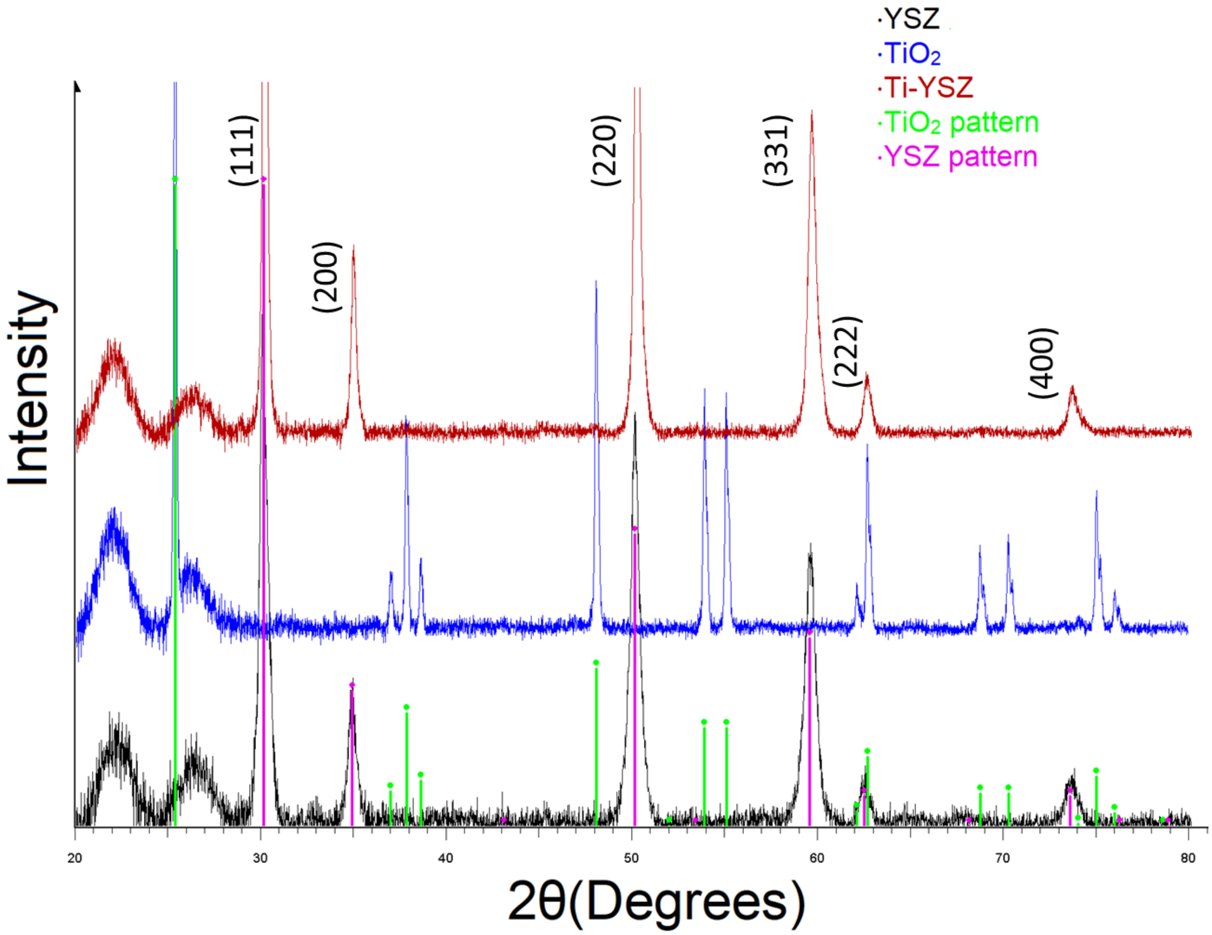

Figure 16: XRD spectra of TiO_2 and YSZ precursors, before and after calcination.

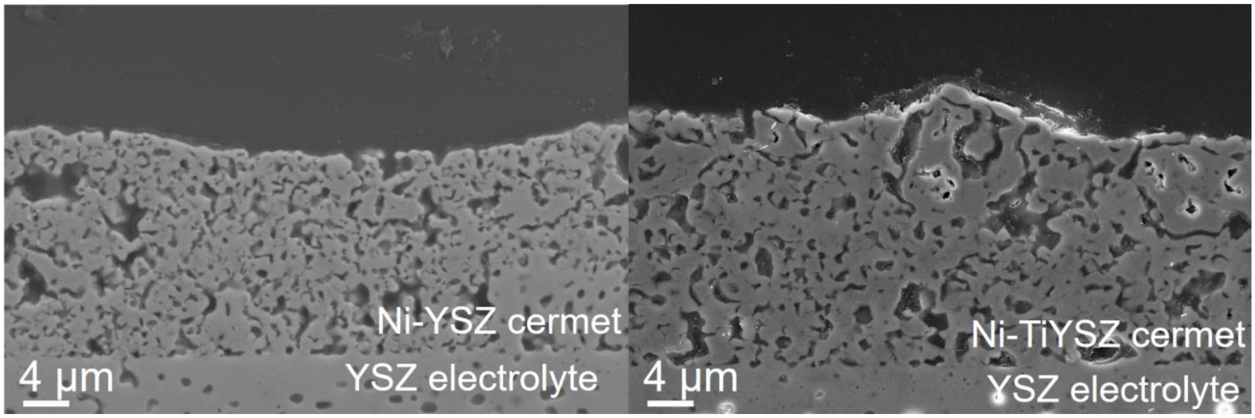

Figure 17: Polished Ni-YSZ cermet electrode (left) and a polished Ni-MIEC cermet electrode (right).

4.4.2 Ni-infiltrated Ni-YSZ symmetric cells

The anode electrode cermets were modified by varying infiltration cycles, infiltrant electrocatalysts, and the cermet electrode composition. The goal was to investigate the effects of infiltration and the role of mixed conduction in the ionic conducting phase of the cermet electrode on performance. Cross-section SEM micrographs of electrodes of Ni infiltrated Ni-YSZ cells as a function of number of infiltration cycles (0 (uninfiltrated) to 5 infiltration cycles) are shown in Fig. 18. All infiltrated cells show the presence of rounded particles which have been previously identified to be the roughly hemispherical nickel nanoparticles on the YSZ grains of the Ni-YSZ cermet [56].

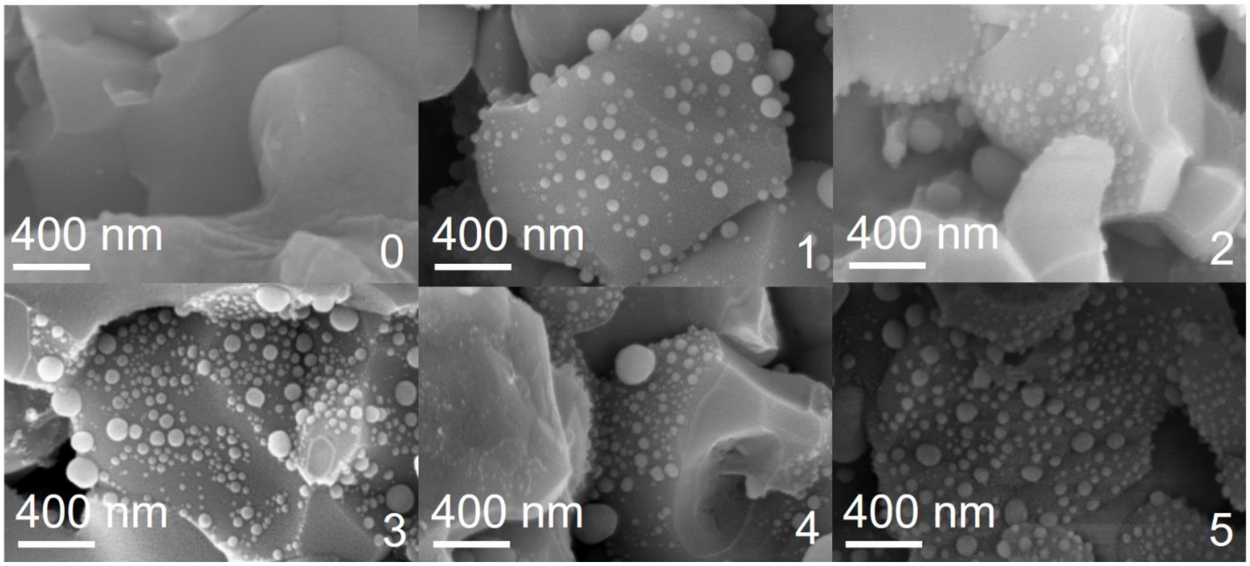

Figure 18: SEM fracture cross-sections of the Ni-YSZ cells infiltrated with nickel nanoparticles. The number of infiltration cycles are shown on the bottom right of each image.

The changes in the surface area coverage of YSZ/MIEC by Ni nanoparticles, Ni nanoparticle density, and added TPB length as a function of infiltration cycles are shown in Fig. 19. Fig. 19a shows the surface area fraction of YSZ/MIEC grains adjacent to pores that are covered with Ni nanoparticles as function of infiltration cycles. Fig. 19b shows the number density of Ni nanoparticles on the YSZ/MIEC grains adjacent to the pores as a function of infiltration cycles. Fig. 19c shows the added TPBs in the samples as a function of infiltration cycles.

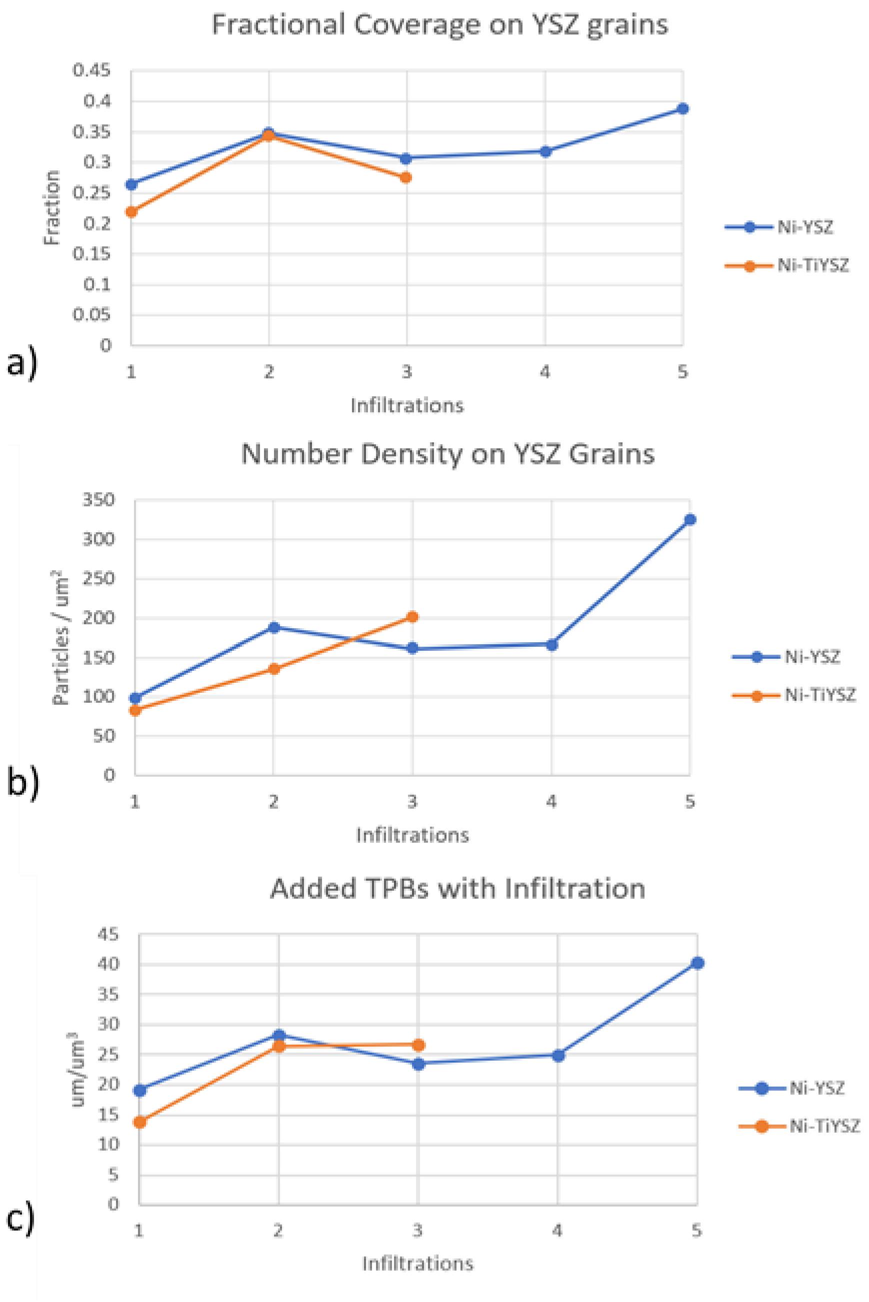

Figure 19: a) Surface area fraction of YSZ/MIEC grains adjacent to pores covered by Ni nanoparticles, b) number density of Ni nanoparticles on YSZ/MIEC surface adjacent to pores, and c) Added TPB density, as a function of infiltration cycles.

The EIS measurements acquired at 700°C and 800°C with a gas composition of 50% H_2 - 50% H_2O are shown as Nyquist plots in Fig. 20 with the ohmic resistance subtracted from the total resistance, to more easily compare anodic polarization resistances of the cells. The general shapes of these polarization curves appear to be two semicircles, with one much larger than the other. A key observation is that for the first three infiltration cycles, the magnitude of the anodic polarization resistance decreased with increasing number of infiltration cycles. However, a further increase in the number of infiltration cycles led to an inversion with increasing anodic polarization resistance with increasing number of cycles. It should be noted that for Ni infiltrated Ni-YSZ anodes, not all infiltration-added TPBs are active since unconnected Ni nanoparticles on YSZ that are far away from the TPBs of the Ni-YSZ cermet are inactive due to a lack of a connected electronic pathway.

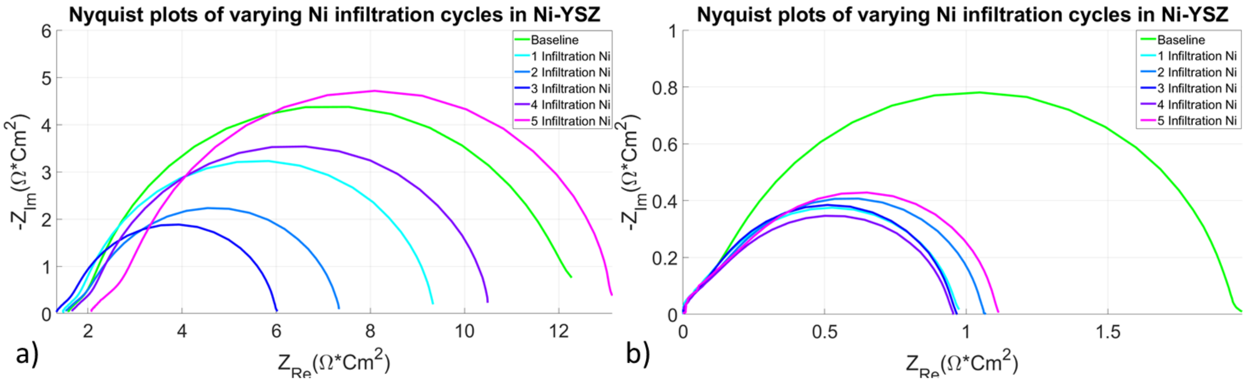

Figure 20: EIS performance at 700°C (a) and 800°C (b) for Ni infiltrated Ni-YSZ cells.

4.4.3 GDC and Ni-GDC-infiltrated Ni-YSZ symmetric cells

In a second set of experiments, GDC was introduced as an MIEC infiltrant phase, and Ni-YSZ cermet scaffolds were infiltrated with a single infiltration cycle. SEM images of fracture cross-sections of the Ni-YSZ cermet in Fig. 18 show the GDC and Ni-GDC nanocatalyst particles.

While Ni nanoparticles form hemispherical deposits on the YSZ, the GDC deposits as a thin porous film over the entire cermet scaffold. It has been previously reported that when Ni-GDC is co-infiltrated into the fuel electrode, the Ni nanoparticles are surrounded by GDC which forms a connected film over the YSZ [14, 56]. These connected GDC and Ni-GDC nanocatalysts make differentiation of the nanoparticle phases difficult in SEM images. The goal of these infiltrations was to see if providing a connected electronic pathway in the infiltration microstructure would reduce anode polarization and improve performance.

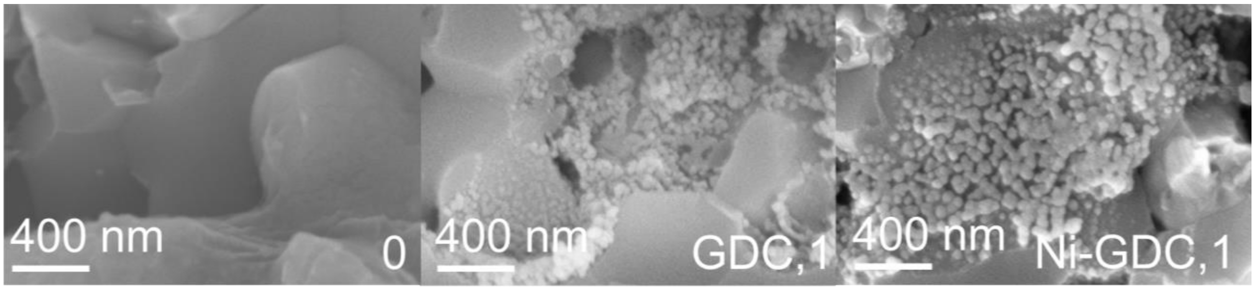

Figure 21: SEM fracture cross-sections of the Ni-YSZ cells infiltrated with nickel nanoparticles. Infiltrant solution and cycles of infiltration are shown on the bottom right of each image

The EIS data and the resultant DRT analysis of the tested GDC and the Ni-GDC infiltrated cells (with a single infiltration) are displayed in Fig. 19 at 700°C and 800°C, with the performances of a baseline (uninfiltrated) and a Ni infiltrated cell for comparison. Infiltration of Ni-GDC or GDC results in a significant decrease in polarization. The overall polarization resistances of the one-time infiltrated cells are less than 10% of the polarization resistance of the baseline cells. However, no further reduction in the polarization resistance was seen with additional infiltration cycles (data not presented), indicating that a single infiltration cycle is sufficient, when a connected MIEC infiltration microstructure can be formed.

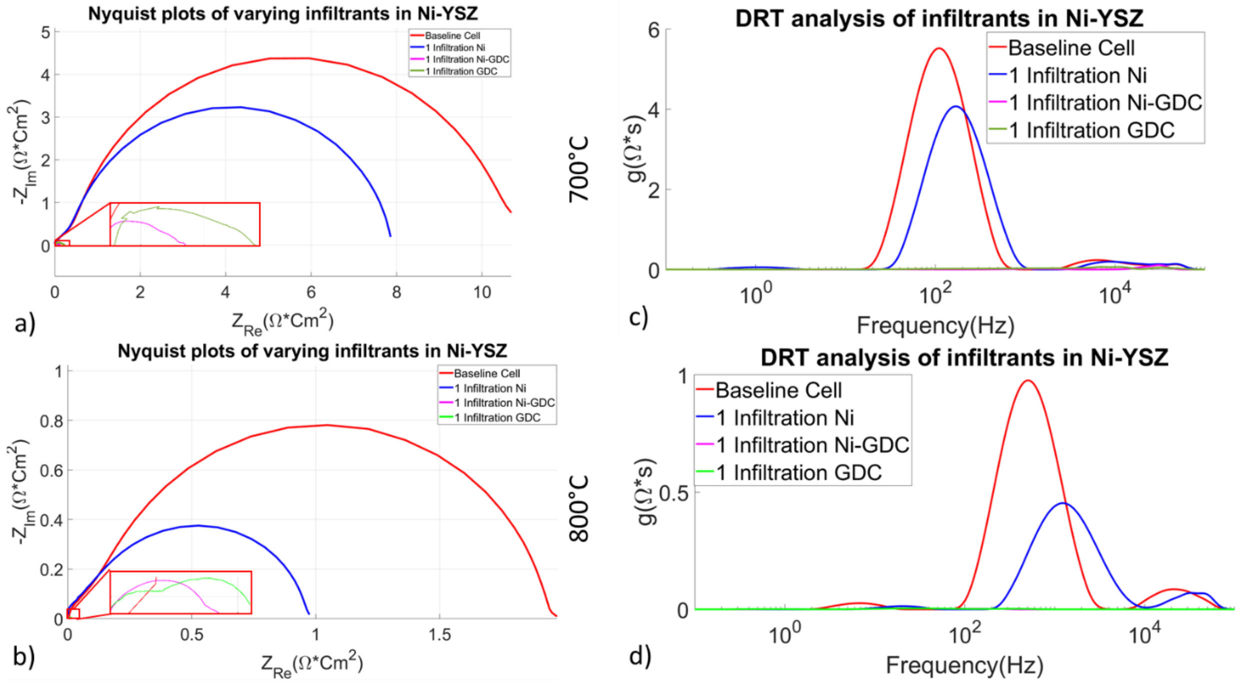

Figure 22: EIS performance at 700°C (a) and 800°C (b) for Ni, Ni-GDC and GDC infiltrated Ni-YSZ cells. Corresponding DRT analysis is shown at 700°C (c) and 800°C (d).

Fig. 22 shows that the presence of the connected MIEC phase completely suppressed peaks in the 10-1000 Hz (medium frequency) range. This result is consistent with recent work by Barnett and co-workers, who showed that charge transfer in Ni-YSZ anodes can be minimized by GDC infiltration as seen by complete suppression of medium frequency peaks [59]. They reported that remaining relevant processes manifest as small fringe peaks for the infiltrated cells and, based on their frequency range, indicate that gas diffusion and gas conversion are responsible for cell polarization once charge transfer is minimized in the cermet electrode.

4.4.4 Ni-infiltrated Ni-MIEC symmetric cells

In the third set of experiments, Ni nanocatalyst particles were infiltrated into Ni-MIEC scaffolds to see if the electronic conductivity of the MIEC phase could activate all the additional TPB boundaries formed by Ni nanoparticles deposited on the TiO_2 doped YSZ grains. SEM fracture cross-sections of electrodes of pristine and 1 and 2 cycle Ni-infiltrated Ni-MIEC cells are shown in Fig. 23. The images show Ni nanoparticles which appear as randomly distributed hemispherical particles across the MIEC grains in the scaffold, similar to Fig. 15. The average nanoparticle size and added TPB values from the infiltrated nanoparticles are shown in Fig. 16. Fig. 16 shows that the added TPB density of a Ni infiltrated YSZ after 3 cycles of infiltration (which had the lowest polarization resistance) is reasonably comparable to a Ni infiltrated Ni-MIEC sample after 1 infiltration cycle. Any significant performance differences between these samples cannot be attributed solely to differences in total added TPB density.

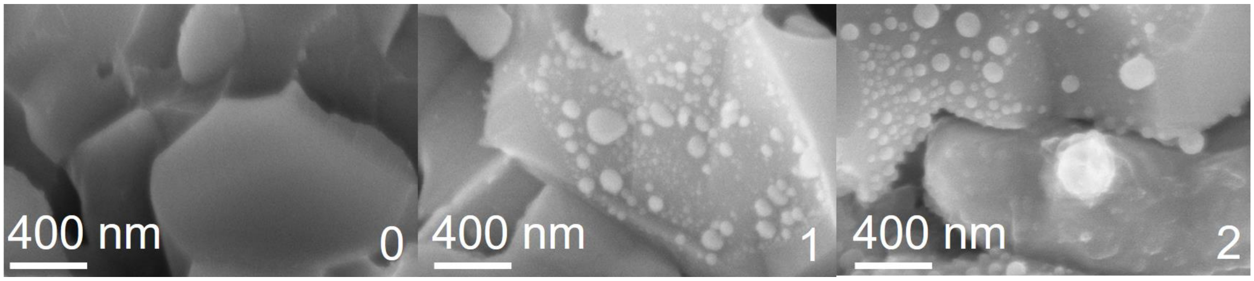

Figure 23: SEM fracture cross-sections of the Ni-MIEC cells infiltrated with nickel nanoparticles. Cycles of infiltration are shown on the bottom right of each image.

The EIS spectra and DRT analysis of Ni-infiltrated Ni-MIEC cells are presented in Fig. 24. The figure shows that at 700°C, 3 cycles of infiltration leads to the lowest polarization resistance, while at 800°C, 1 cycles of infiltration leads to the lowest polarization resistance. In general, the improvement after 1 cycle of infiltration was much more significant compared to changes after subsequent cycles. Again, this indicates that if a connected electronic pathway can be provided by the MIEC, all added TPBs can be activated. Thus 1 cycle of infiltration for the Ni-MIEC case is chosen for the comparison between samples.

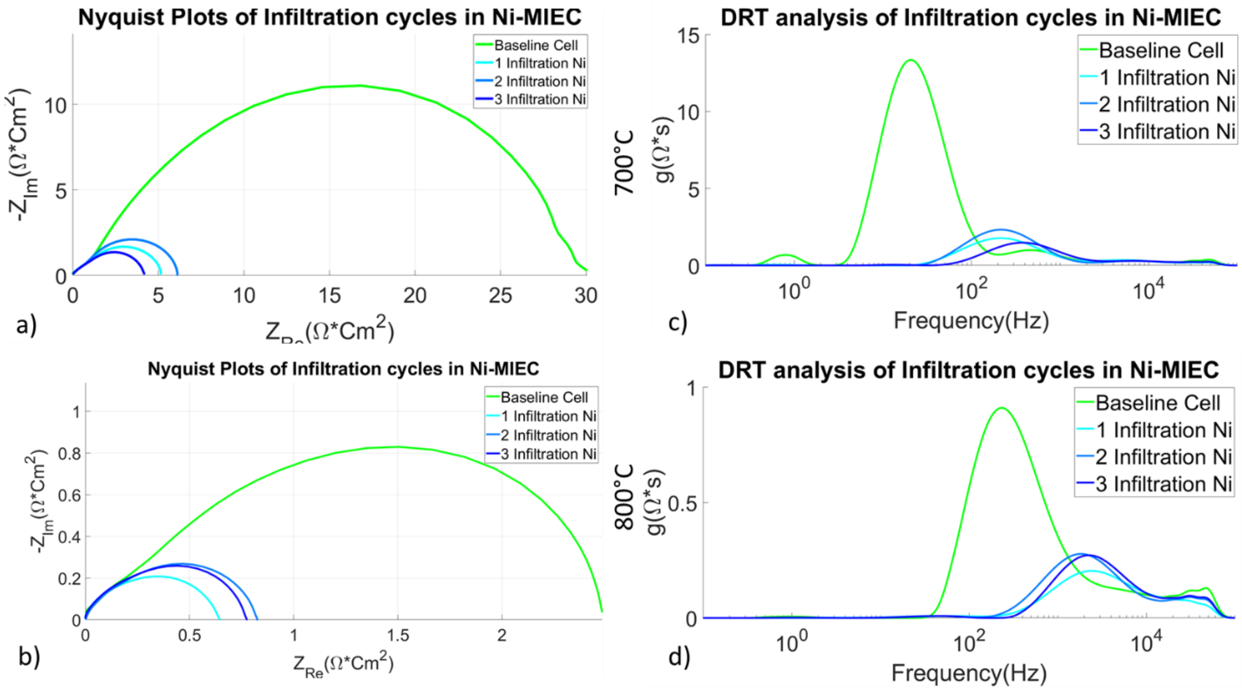

Figure 24: EIS performance at 700°C (a) and 800°C (b) for Ni infiltrated Ni-MIEC cells. Corresponding DRT analysis is shown at 700°C (c) and 800°C (d).

Table 3 shows polarization resistance for each optimally infiltrated cell tested at 700°C and 800°C. At the same temperature, single infiltration into anode compositions containing MIECs perform just as well, or better, than optimally infiltrated anodes without MIECs. The total decrease and percent decrease in polarization resistance is much larger for cells infiltrated with GDC or Ni-GDC, indicating a strong correlation between nanoparticle performance and the presence of mixed conductivity within the infiltrants. This is in accord with prior work from our group [14,52,56,67]. Additionally, the table also shows the presence of mixed conductivity within the ionic scaffold can improve the utilization of metal nanoparticles, as shown by the optimally infiltrated Ni-MIEC cell.

Testing Temperature	**AAL cermet composition**	**Infiltrant**	**Infiltration cycles**	**Polarization resistance ($\Omega.cm^2$)**	**Percent change compared to pristine baseline(%)**
800°C	Ni-YSZ	N/A	0	1.95	0%
		Ni	3	0.97	-50.2%
		GDC	1	0.02	-98.9%
		Ni-GDC	1	0.01	-99.5%
	Ni-MIEC	N/A	0	4.86	149.2%
		Ni	1	0.65	-66.7%
700°C	Ni-YSZ	N/A	0	10.58	0%
		Ni	3	4.69	-55.7%
		GDC	1	0.22	-97.9%
		Ni-GDC	1	0.12	-98.9%
	Ni-MIEC	N/A	0	29.76	181.3%
		Ni	1	5.14	-51.4%

Table 3: Total polarization resistances of Ni-YSZ and Ni-MIEC cells optimally infiltrated with Ni, GDC and Ni-GDC electrocatalysts, and the percent decrease in polarization versus the baseline uninfiltrated cell.

4.4.5 Equivalent Circuit Model analysis of Ni-infiltrated cells

A side-by-side comparison of the baseline and optimally infiltrated Ni-YSZ cermets is shown in Fig. 25. It should be noted that the baseline Ni-MIEC cermet has worse performance than the baseline Ni-YSZ. The possible reasons for this will be discussed later in this section. However, Ni infiltration greatly improves the performance of the Ni-MIEC sample. The DRT analysis from the EIS of Ni-infiltrated Ni-YSZ cells are presented in Fig. 26, indicating that the most sluggish processes are present in the 100 to 1000 Hz region. Prior work in Ni-YSZ anodes in electrolyte supported cells suggest interfacial grain boundary diffusion and gas diffusion processes occur at close to 10^4 Hz and 1 Hz respectively [66]. In this work, the Warburg element, associated with concentration polarization, is neglected due to high flow rates of 300 cc/min. Furthermore, processes ranging from 10-1000 Hz have been analyzed in this model, which can be captured by the TLM element.

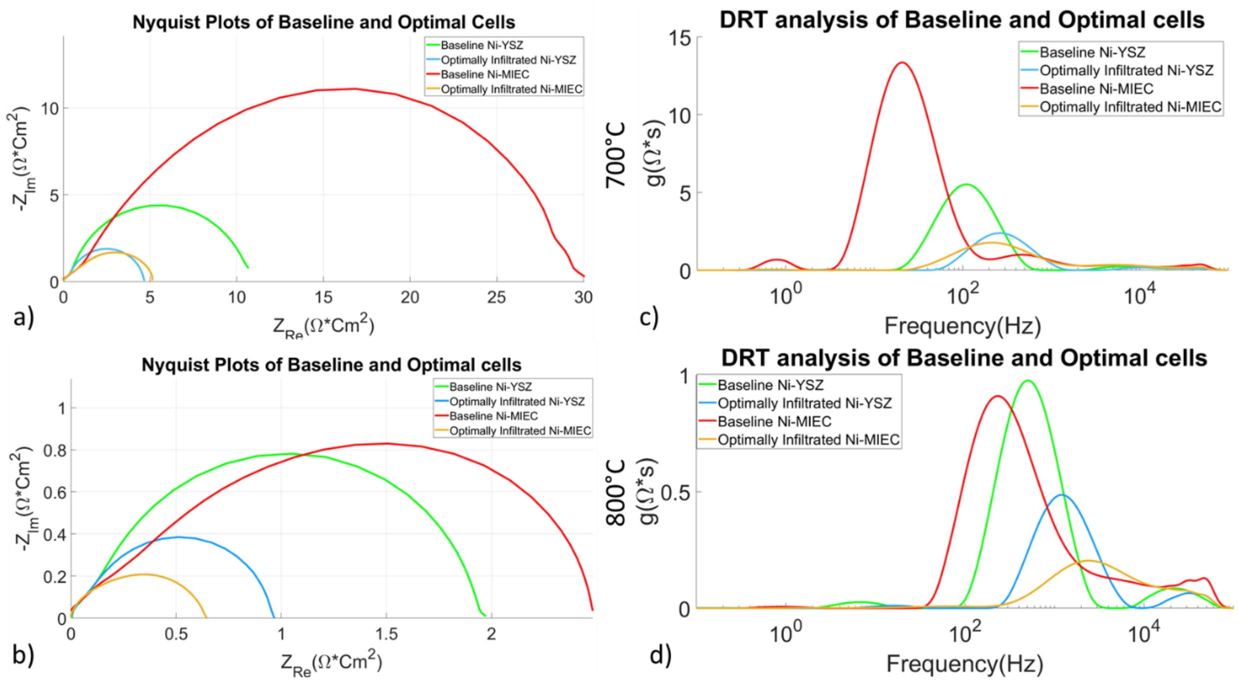

Figure 25: EIS performance at 700°C (a) and 800°C (b) for optimal Ni infiltrated Ni-YSZ and Ni-MIEC cells. Corresponding DRT performance is shown at 700°C (c) and 800°C (d).

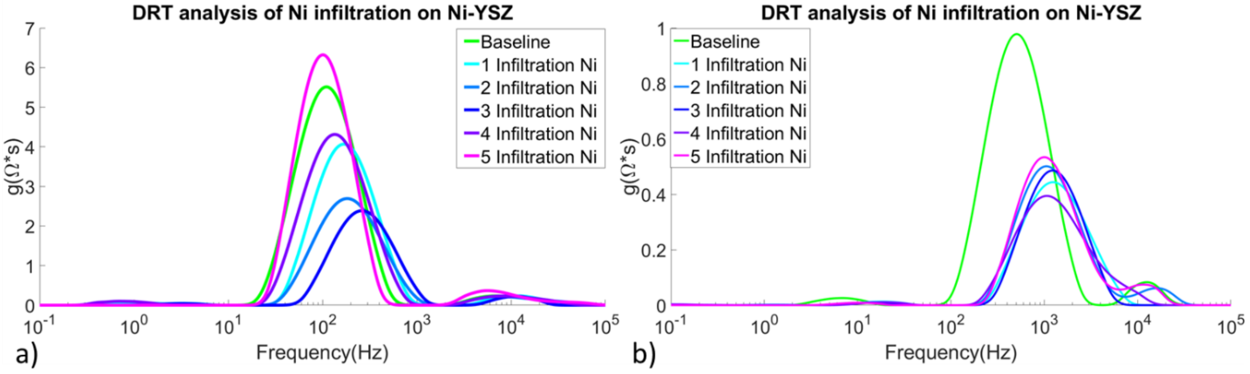

Figure 26: DRT analysis at 700°C (a) and 800°C (b) for Ni infiltrated Ni-YSZ cells.

The TLM model is shown schematically in Fig. 27. By assuming that the entirety of the cermet electrode behaves like an MIEC column, the main polarization process can be modelled using the TLM element in the DRT analysis. It is assumed that the majority of the polarization is due to the sluggish charge transfer, so the equivalent circuit model presented for these cells consist of a single transmission line element.

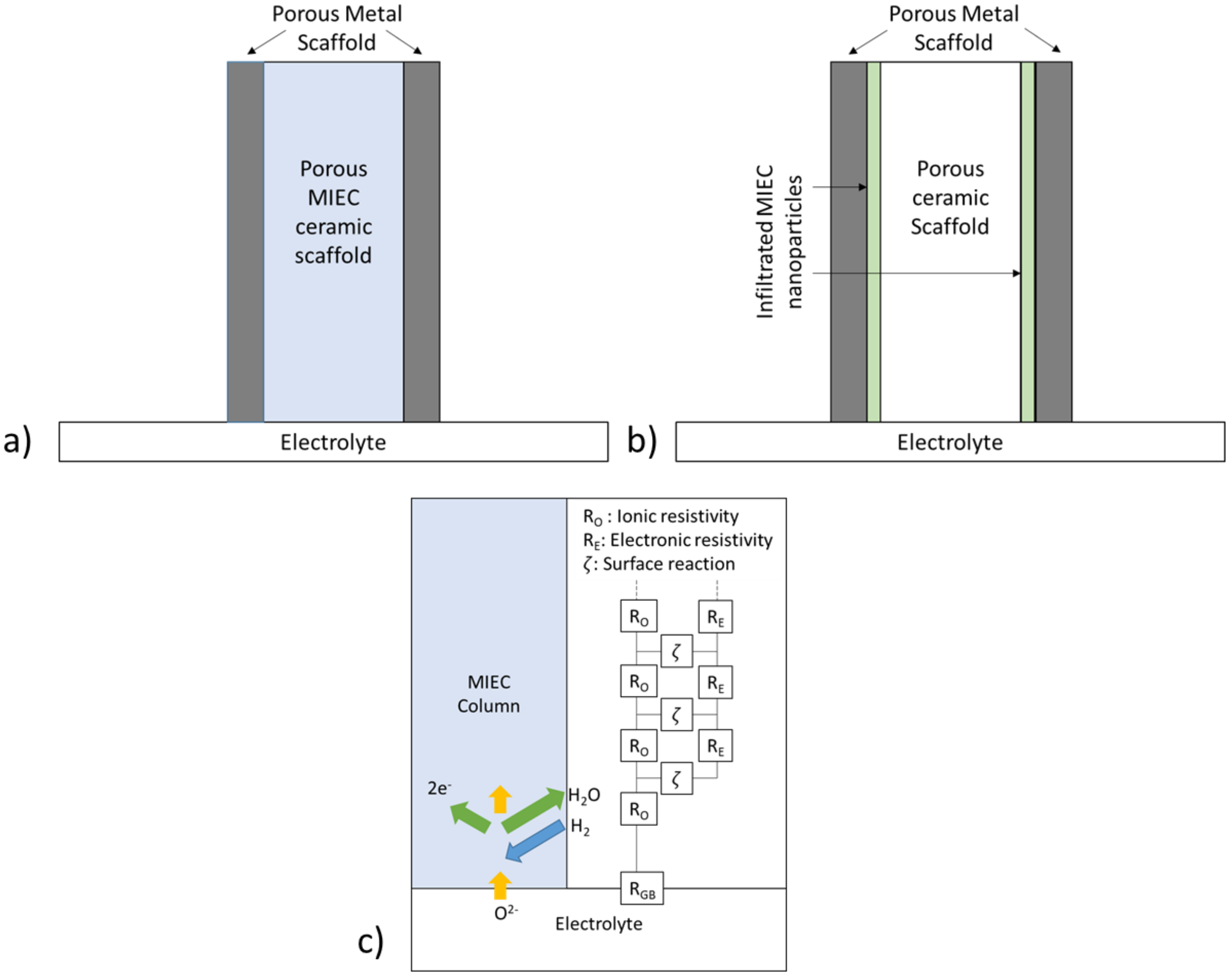

Figure 27: Simplified model of MIEC incorporation within electrodes, and the corresponding circuit diagram. a) represents a porous transition metal doped ionic scaffold with an electronic scaffold, while b) represents a infiltrated MIEC phase sandwiched between porous ionic and electronic scaffolds. c) represents the transmission line nature of the above columns simplified into a single MIEC column. Impedance within the column is a function of RΩ (Ωcm^{-1}) and ζ (Ω.cm). The surface charge transfer reaction ζ has a corresponding characteristic frequency (frxn) and resistance (Rrxn). (Adapted from Nielsen et. al [68].)

The plots of the TLM variables (f_{rxn}, R_O and R_{rxn}) with respect to cycles of Ni infiltration are shown in Fig. 28. Although R_O remains roughly constant at all infiltration levels, there are noticeable variations in f_{rxn} and R_{rxn} and their correlation to the overall cell performance. The best overall performance correlates to a lower surface reaction resistivity, and a higher surface reaction frequency. One possible reason for this is the introduction of new active TPBs provided by infiltration, allowing more surface reactions to occur. Conversely, both the baseline and the 5-

cycle infiltrated cell show worse performance, which is also reflected in the inversion in both f_{rxn} and R_{rxn}. This further supports the hypothesis that subsequent infiltration cycles do not increase nanoparticle density, but rather increase surface coverage and coarsen and coalesce existing nanoparticles, eventually negating any improvement from additional infiltration. A second possibility is that additional infiltration results in Ni preferentially depositing uniformly onto existing Ni grains in the cermet scaffold.

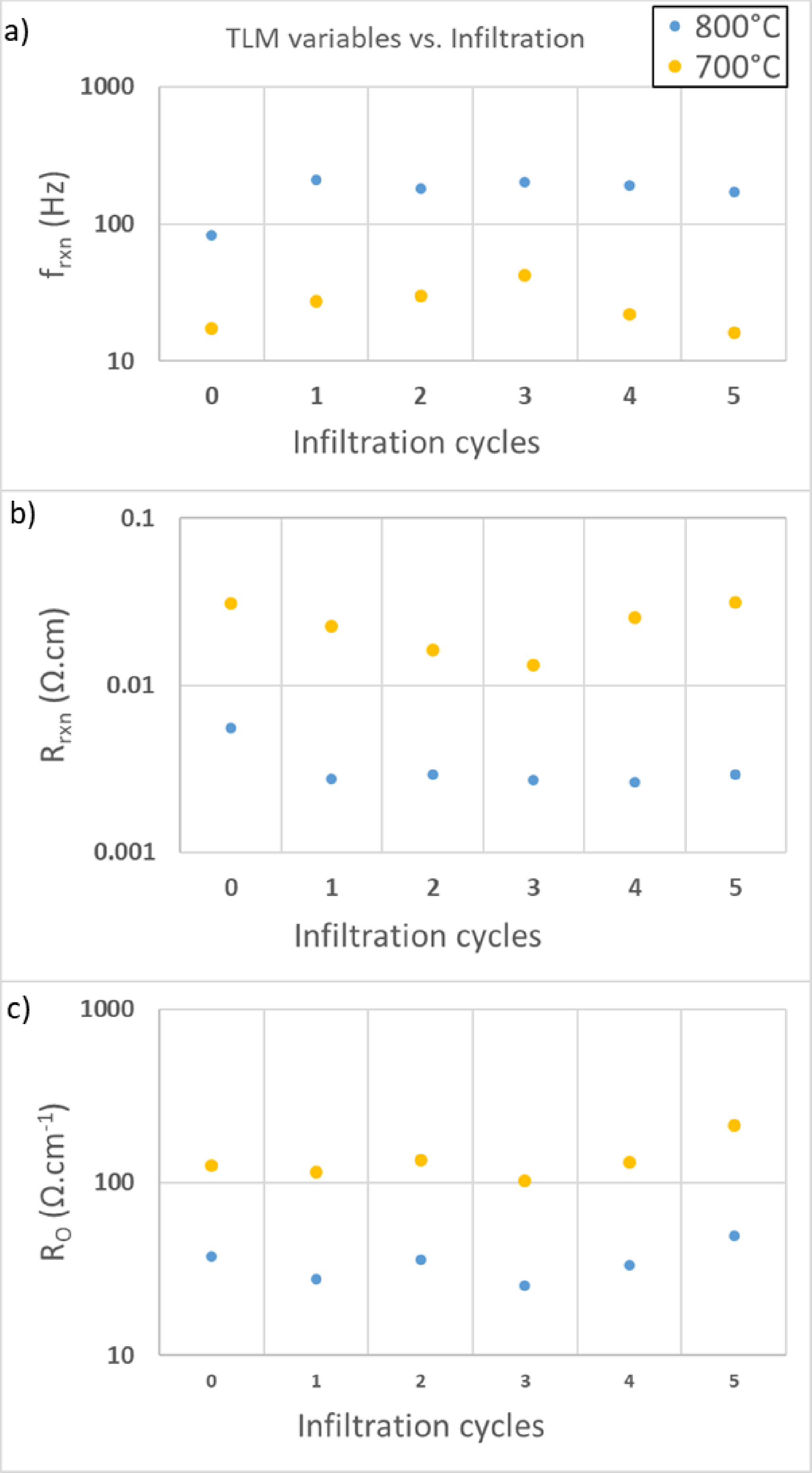

Figure 28: TLM variables frxn (a), Rrxn (b) and RO (c) as a function of infiltration cycles at 700°C and 800°C for Ni infiltrated Ni-YSZ cells.

By looking at the trends in the TLM element for infiltrated Ni-MIEC in Fig. 29, infiltration increases f_{rxn} and decreases R_{rxn}, while R_O remains fairly constant, aside from its value for a single infiltration. This suggests that more nanoparticles contribute to the half-cell reactions in Ni-MIEC electrodes than in conventional Ni-YSZ fuel electrodes, effectively allowing more nanoparticles to become active TPB sites. This would have no effect on the oxygen ion diffusion, which is primarily through the bulk ionic phase and explains the relatively fixed value of R_O. Fig. 30 compares the TLM elements between tested Ni-infiltrated Ni-YSZ and Ni-MIEC cells, as a function of infiltration cycles. The baseline Ni-MIEC cells have lower f_{rxn} and higher R_O compared to baseline Ni-YSZ cells, which can be attributed to the lower ionic diffusivity in the 3TiYSZ. The order of magnitude increase in R_O can be the reason why the baseline Ni-MIEC cell performs much worse than the baseline Ni-YSZ cell. However, infiltration into the Ni-MIEC shows larger improvements compared to infiltration into Ni-YSZ, which is reflected in the increases in f_{rxn} and decreases in R_{rxn}. The R_O varies slightly among the tested Ni-YSZ cells, yet remains constant within Ni-MIEC cells.

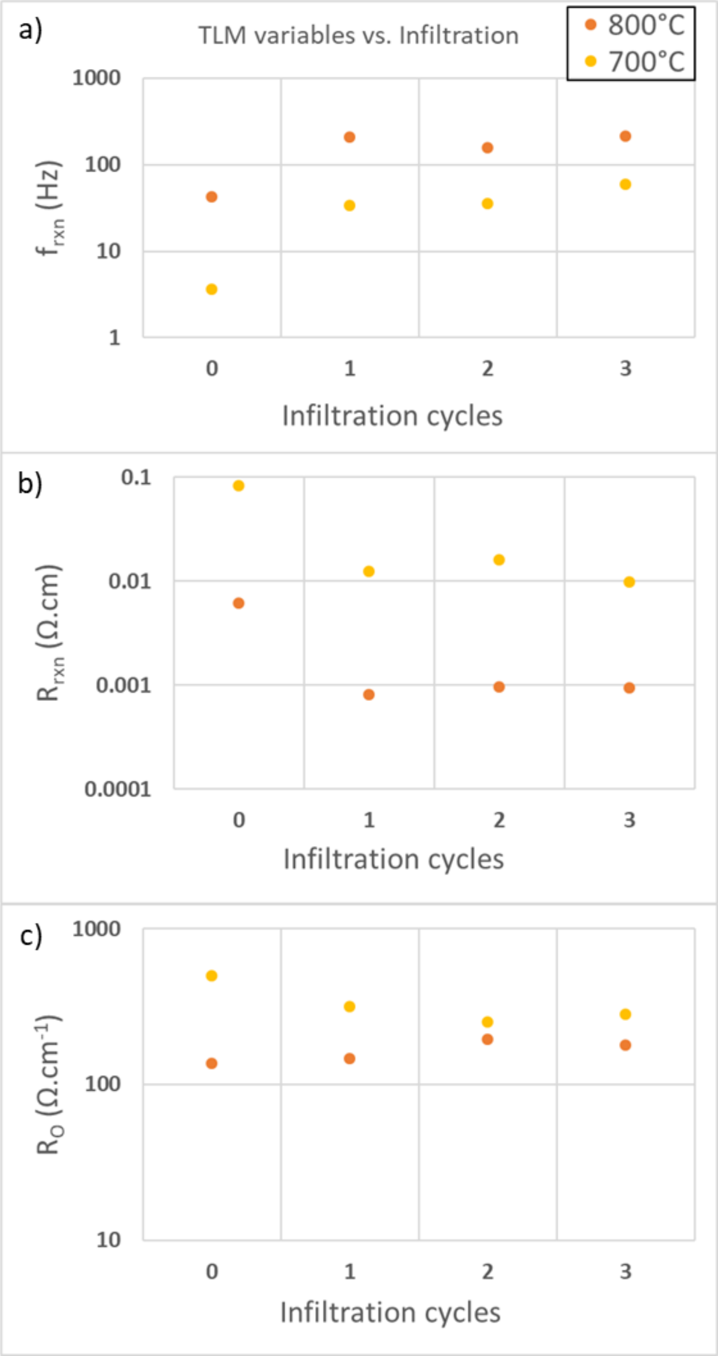

Figure 29: TLM variables frxn (a), Rrxn (b) and RO (c) as a function of infiltration cycles at 700°C and 800°C for Ni infiltrated Ni-MIEC cells.

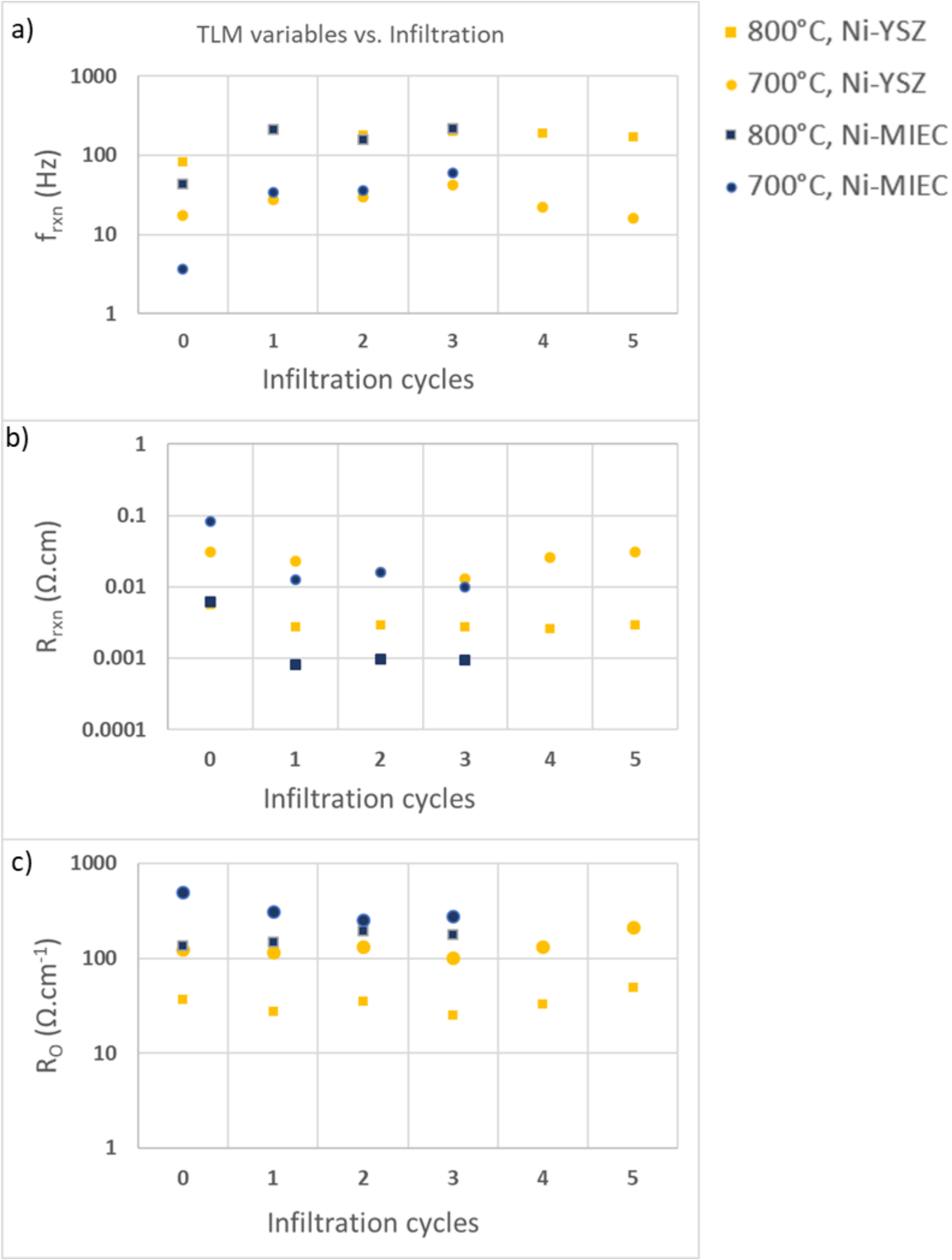

Figure 30: TLM variables frxn (a), Rrxn (b) and RO (c) comparing Ni infiltrated Ni-YSZ and Ni-MIEC cells.

4.4.6 Electronic pathways present in MIEC scaffolds

The preceding observations indicate that the cell performance improvement via infiltration is mostly attributed to the increase in the active TPB density throughout the cermet electrode, but improvement is still limited by the number of inactive reaction sites, too far away from a bulk scaffold. The large improvement in Ni-MIEC cells via infiltration, as well as the trends shown in the transmission line element, indicate an increase in surface reaction conductivity and frequency. In other words, the mixed conductivity appears to facilitate electron transfer from isolated TPBs, allowing all the infiltrated nanoparticles to partake in the faradaic reaction. Although the ionic conductivity of the cermet decreases, the electronic transport introduced into the predominantly ionic-conducting bulk phase increases the rate of charge transfer reactions and improves the overall performance of the cell.

4.4.7 Effect of GDC in Ni-GDC and GDC infiltrated cells

In order to examine the trends in the charge transfer polarization among all three infiltrants, the TLM variables f_{rxn}, R_{rxn}, and R_O have been plotted as a function of the number of infiltration cycles for 700°C and 800°C operation in Fig. 31. Although it is expected that the center frequency of the surface reaction is higher with the additional TPBs, the plots indicate infiltration does not always speed up the interfacial reaction. However, R_{rxn} and R_O decrease significantly once any amount of GDC is infiltrated into the cell. The decrease in $\mathrm{R_{rxn}}$ could represent the overall faradaic reaction rate increasing, as the GDC forms not only TPBs, but also double phase boundary (DPB) regions (2-dimensional surfaces), as the film can conduct electronic and ionic carriers and can be electrochemically effective in contact solely with the pore phase. Another observation to note is that the sustained decrease in R_O could mean the oxygen ions have more pathways to active reaction sites, allowing cell reactions to occur in parallel through both TPBs and DPBs, resulting in lower overall resistivity.

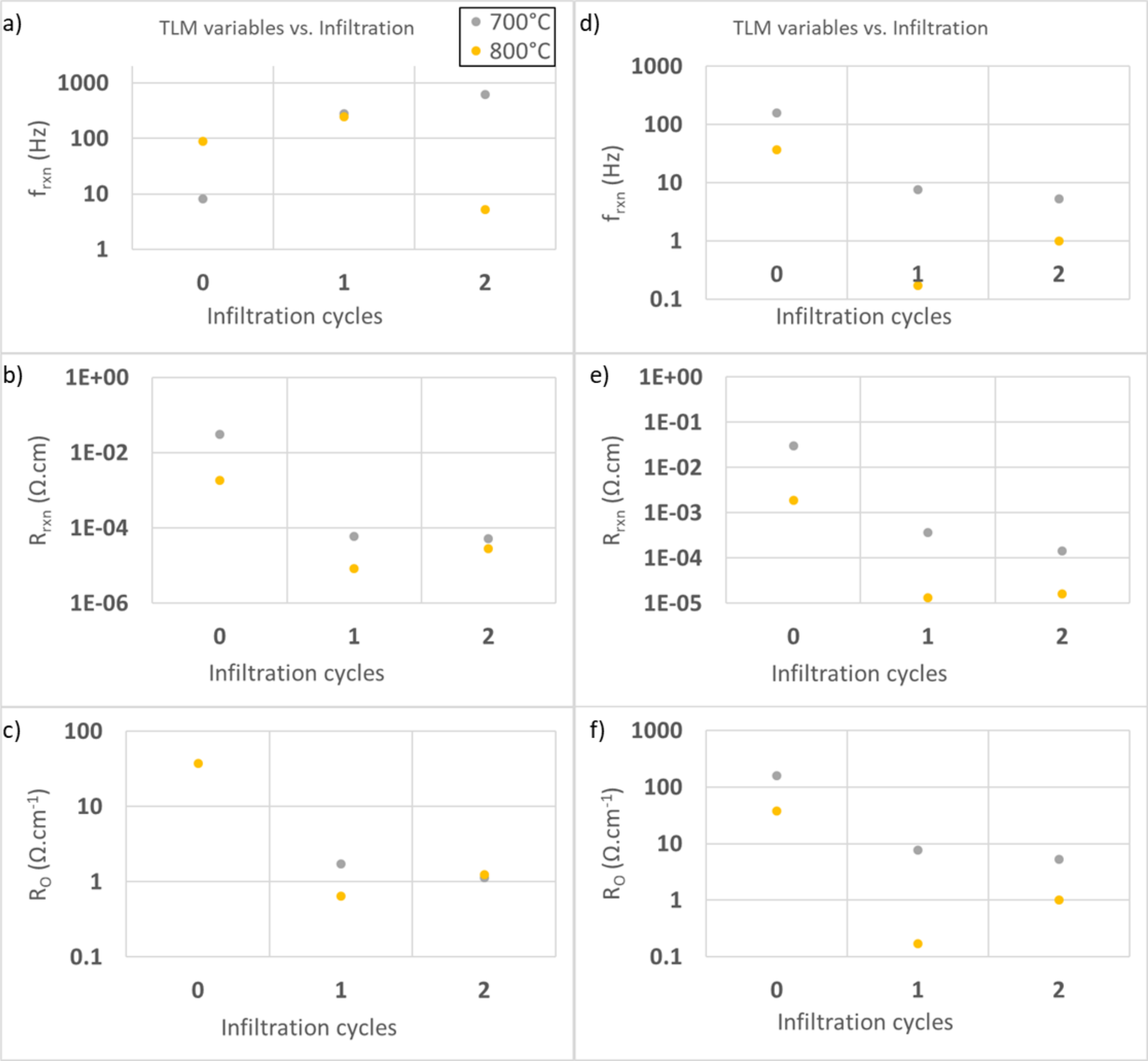

Figure 31: TLM variables frxn (a), Rrxn (b) and RO (c) as a function of infiltration cycles at 700°C and 800°C for GDC infiltrated Ni-YSZ cells. The same TLM variables respectively (d, e, f) are shown for Ni-GDC infiltrated Ni-YSZ cells.

4.4.8 Electronic pathways in MIEC infiltrants

In a similar fashion to the MIEC composition for the ionic scaffold, the GDC and Ni-GDC infiltrated electrocatalysts provide mixed conductivity through the porous film coating. The transfer of both electrons and oxygen ions under reducing conditions indirectly increases the reaction rate, as the nanoparticle deposits connect both isolated Ni grains as well as isolated Ni nanoparticles. It is clear that at lower temperatures, the surface charge-transfer frequencies in infiltrated cells substantially increase, along with both decreasing values R_{rxn} and R_O. The decrease in both resistivities suggests that the effect of GDC increases overall charge transfer reactions in the cermet electrode by better connecting the two bulk networks as well as deposited nanoparticles. Interestingly, Ni-GDC infiltration results in slightly better performance than GDC infiltration alone after one cycle. While GDC infiltrants improve anode performance, they do not introduce as many active TPB sites compared to Ni infiltrants. Future work will attempt to better quantify the contributions of Ni and GDC infiltrants separately within cermet scaffolds.

4.5 Conclusions

The results show that Ni electrocatalyst infiltration can alone improve cell performance, but incorporation of MIEC phases can greatly enhance cell performance over mainly electronic and ionic conducting phases. The infiltration of GDC onto a pre-existing cermet scaffold can improve cermet electrodes under reducing conditions. Results have shown a tenfold improvement under different temperature conditions. MIEC ionic scaffolds infiltrated with solely Ni electrocatalysts require fewer infiltration cycles to reach optimal performance when compared to infiltration into scaffolds with purely electronic (Ni) and ionic (YSZ) phases. While infiltrated Ni-MIEC electrodes greatly improve over pristine electrodes, the tradeoffs found within infiltrated Ni-MIEC and Ni-YSZ cells are similar. Therefore, improvements in the ionic scaffold composition should be explored. Inactive nanoparticle catalysts are present in the Ni-YSZ scaffold due to the lack of electronic charge carriers far away from the bulk metal phase. When applying a transmission line model element to the charge transfer polarization, it is clear that MIEC incorporation to the infiltrant can increase the surface reaction kinetics (f_{rxn}) as well as decrease the surface reaction and oxygen ion resistivity (R_{rxn}, R_O), while MIEC incorporation to the ionic phase decreases only the surface reaction resistivity (R_{rxn}).

5. EXPLORING THE ROLE OF HUMIDITY, TEMPERATURE AND ALTERNATE TRANSITION METAL DOPANTS ON ANODE ELECTROCATALYSIS

5.1. Introduction

Although the studies above have been performed on cells at differing temperatures, the humidity during these studies was held at 50% (balance hydrogen). This was primarily chosen as an intermediate condition, chosen to represent conditions intermediate between very low (hydrogen-rich) and very high (hydrogen-poor) fuel conditions. While this does provide some insight into the performance of AAL cermet electrodes under load, testing under other humidity conditions could bring new insights, especially concerning the behavior of infiltrated nanoparticles under different H_2O/H, i.e. pO_2 levels.

While TiO_2 has been used as a dopant to introduce electronic transport in YSZ in our previous work, it has commonly been used in other work as a sintering aid [69-71]. In other words, other researchers may be conflating the effect of better sintering of the YSZ in the anode, with the introduction of electronic transport due to the transition metal doping into the ionic-conducting YSZ scaffold at the sintering temperature. To confirm the role of electronic transport in the YSZ on anode electrocatalysis, another batch of Ni-MIEC cells were fabricated and tested under varying operating temperature and humidity levels, but with a transition metal oxide dopant other than TiO_2 in the YSZ. This MIEC consisted of 3FeYSZ, i.e. 3 mol% Fe_2O_3 – 97 mol% YSZ. Iron(III) Oxide is also a sintering aid that is used for AAL fabrication in other infiltration studies [72-75]. Although other transition metal oxides form solid solutions with the cubic YSZ, these two oxides, TiO_2 and Fe_2O_3, appear to be the most frequently used. They are also relatively cheap compared to alternatives such as Pr and W [22,76-78]. Therefore, Fe and Ti are interesting transition metal cation dopants in YSZ, to verify if the electronic transport imparted to the predominantly ionic conducting phase of the cermet, namely YSZ, can improve its performance.

It has been shown that while conventional SOFC anodes are able to operate over tens of thousands of hours, infiltrated metal nanoparticles will coarsen over the first 100 hours of operation [55,79,80]. This coarsening not only results in lower TPB density in the electrode, but also lower electrical conductivity [53-55, 81]. Two factors are known to contribute to the coarsening of nanoparticles; the operating temperature of the cell, which accelerates at higher temperatures, and the increase of humidity during cell operation. Both greatly affect the smaller nanoparticles infiltrated into the electrode cermets, which generally have smaller feature sizes. While Nickel is not directly affected by the water vapor content in the fuel, the pO_2 is dictated by the ratio of the partial pressures of H_2 to H_2O in the anode gas. Based on Gasper et. al's work, the numerical calculations shown in Fig. 32 evaluate the contact angle of Ni adjacent to YSZ as a function of oxygen activity on the Ni surface, both as a function of pH_2O (balance H_2) [14]. While humidity allows the nanoparticles to become connected temporarily, it also accelerates the coalescence of Ni particles into one another. This greatly affects the smaller nanoparticles, which tend to have the highest TPB to volume ratio as well as higher surface energy compared to larger nanoparticles. While coarsening has been observed in many infiltration studies, the true mechanism behind the coarsening is still unclear.

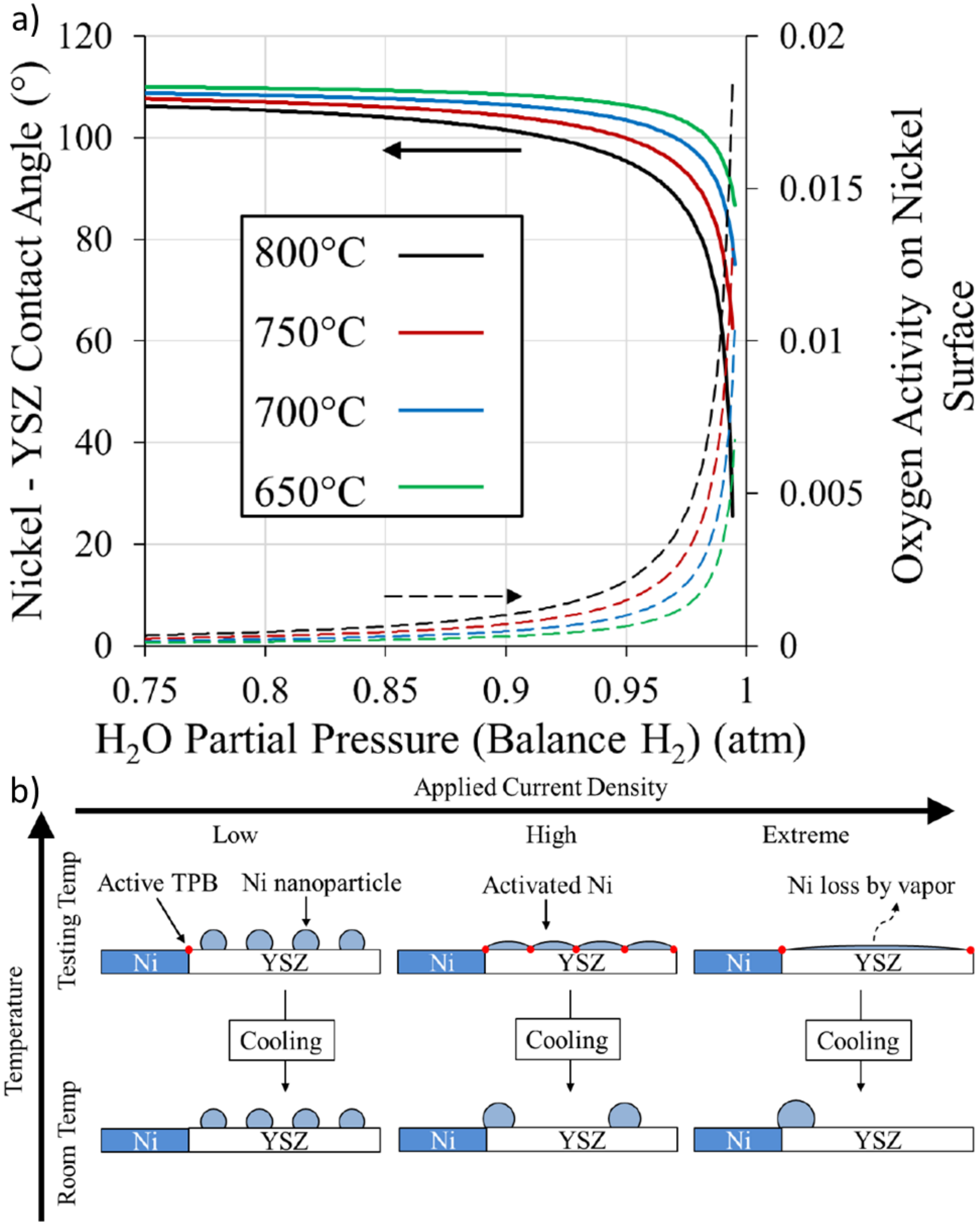

Figure 32: The effect of humidity and current density on Ni/YSZ contact angles, a) as humidity conditions increase locally in the cell microstructure, Ni/YSZ contact angles decrease and Ni wetting occurs. This is shown in b) where higher current densities can increase local humidity due to the formation of water vapor, which can wet Ni nanoparticles. Extreme currents and humidity may cause coalescence of Ni, and Ni nanoparticle coarsening [14].

As mentioned in earlier chapters and prior work, the optimization studies were originally performed to mitigate nanoparticle coarsening and see how nanoparticle loading affects particle morphologies, including the nanoparticle density, average nanoparticle size, nickel nanoparticle coverage on the YSZ surface and overall added TPB length per unit volume [67, 81]. However, it was discovered through the infiltration of GDC and Ni-GDC into cermet electrodes that 1 cycle of infiltration was sufficient to show optimal performance under 50% humidity, whereas infiltration of Ni required 3 cycles in order to optimally decrease the polarization resistance under the 3% and 50% humidity levels and operating temperatures from 700°C to 800°C. While it was initially hypothesized that GDC film enveloped and anchored Ni nanoparticles and prevented coarsening, fracture SEM depicted Ni nanoparticles as only partially covered by GDC, or located on top of the GDC film altogether. An alternate hypothesis was considered based on the development of MIEC in GDC in reducing environments, activating a large DPB [57, 81]. This DPB greatly extended the distance across which oxygen ions can be transported, as well as served to connect electrically distant and physically separated Ni nanoparticles to the percolated Ni/YSZ grains in the main scaffold. *It is expected that* in a conventional Ni-YSZ electrode without GDC, these isolated nanoparticles would normally be electrochemically inactive. Additionally, while GDC did not successfully anchor the Ni nanoparticles to the YSZ scaffold, the development mixed conduction provided better performance with less Ni loading.

The other important observation was that imparting mixed conductivity into the AAL would allow electronic and ionic conductivity through the ionic scaffold. While this could potentially reduce the ionic conductivity and increase overall ohmic resistance, the infiltrated scaffolds would have required less Ni loading. Lesser loading and the resulting larger distance between the isolated but electrochemically active nickel nanoparticles, could mitigate coarsening found in the cell with conventional Ni-YSZ cermet electrodes, and extend the lifetime of infiltrated Ni. But the key for this approach to succeed is imparting sufficient electronic conductivity to the ionic conducting phase of the cermet electrode; i.e. replace or augment the ionic conducting YSZ with a mixed ionic and electronic conducting (MIEC) phase.

To measure the effects of different operating conditions, introduction of MIEC phases, and infiltrant loading on the AAL, additional cells were fabricated, infiltrated and characterized. The scope of this chapter is to better understand the mechanism that mitigates anode activation polarization resistance and improves overall anode cermet performance.

5.2. Experimental and Analytical Approach

5.2.1 Materials synthesis

Similar to the studies performed in previous chapters, mixed ionic and electronic conductivity was introduced into YSZ by adding 3 mol. % Fe_2O_3. A suspension of stoichiometric amounts of Fe_2O_3 and 8YSZ powders in ethanol was ball milled for 24 hours to ensure proper powder mixing. After drying the powders in a drying oven, the contents were calcined at 900°C for 5 hours. Subsequently, the particle size was reduced by SPEX milling for 30 minutes. The Fe-doped YSZ, which is expected to be a MIEC phase, replaced the 8YSZ powder used in conventional anodes. A slurry of Ni and Fe-doped YSZ (henceforth referred to simply as Ni-FeYSZ) was used to prepare these modified anodes.

Infiltration solutions of 3 M concentration, containing nickel or gadolinium-doped ceria (GDC) were prepared by dissolving precursors containing $Ni(NO_3)_2$ or $(Gd(NO_3)_3)_{0.1}(Ce(NO_3)_3)_{0.9}$ in 50 mL of ethanol at 90°C. The 3 M Ni-GDC nitrate solution was similarly prepared by adding the nitrate precursors that results in a 1:1 molar ratio of Ni to GDC in an ethanol solvent. GDC under reducing atmospheres behaves as an MIEC, and is thus an ideal MIEC electrocatalyst for infiltration.

5.2.2 Cell fabrication

Symmetric cells with the configuration, fuel electrode/YSZ/fuel electrode, were fabricated by screen printing fuel electrode cermet slurry onto the surfaces of commercially obtained YSZ electrolyte substrates. After the cells were dried and sintered at 1400°C, they were placed in a reducing chamber at 800°C and a gas of 3% humidity (balance hydrogen) was circulated in the chamber to pre-reduce the cermet NiO to Ni, and to introduce additional porosity in the microstructure. Aqueous solutions of 3 M Ni and GDC were then infiltrated into reduced symmetric cells under vacuum. For samples with multiple infiltration cycles, the cell was heated to 320˚C in air to decompose the nitrate salts without oxidizing the Ni network in the cermet electrodes prior to the next infiltration.

5.2.3 Electrochemical testing

For electrochemical testing of these symmetric cells, Ni meshes were affixed to each electrode. The cell was placed inside a single chamber testing apparatus, and EIS data was acquired as a function of temperature and humidity levels in the fuel gas. Initially, the cells were tested in the temperature range of 700°C to 800°C in 50% humidified hydrogen, to observe the effects of infiltration under higher humidity levels. A second set of EIS measurements were conducted at a temperature of 800°C beginning at 50% humidified hydrogen, and decreasing the humidity level sequentially (50%, 37%, 25%, 12% and 3%). EIS measurements were conducted at each humidity level and at a fixed temperature of 800^{o}C. All spectra were acquired using an Zahner Zennium Potentiostat under open circuit conditions with a 10 mV AC signal in the frequency range 0.1 Hz to 100 kHz.

.

5.2.4 Scanning Electron Microscopy (SEM)

Processed and tested symmetric cells were fractured, their cross sections coated with 10 nm of Au, and contacted with copper tape. The electrodes were imaged using a Zeiss Supra 55 SEM at 15 kV using an in-lens detector at 6-8 mm working distance to obtain nanoparticle deposition and morphologies from fractured cross-sections. Fracture cross-sections taken from the same cell were also vacuum infiltrated with epoxy, and polished to compare overall cell porosity and microstructure.

5.2.5 DRT modelling

To best model the data, a TLM element was used in series with a resistor, an RQ element and a finite-length Warburg element. All modelling of the TLM element and the fitting of parameters f_{rxn}, R_O, R_{RQ}, R_W and R_{ct} was performed used a MATLAB^{TM} script developed in-house, and is described in more detail in Appendix 2.

5.3 Results and Discussion

5.3.1 MIEC phase formation and electrode microstructure

Fig. 33 shows powder x-ray diffraction (XRD) spectra of the precursors, as well as the pre-calcined and calcined product. The XRD spectrum of the calcined sample shows a shift in YSZ peaks to higher 2θ values, indicating a reduction in lattice parameters. No second phase peaks are observed, indicating complete dissolution of the Fe_2O_3 into the YSZ lattice.

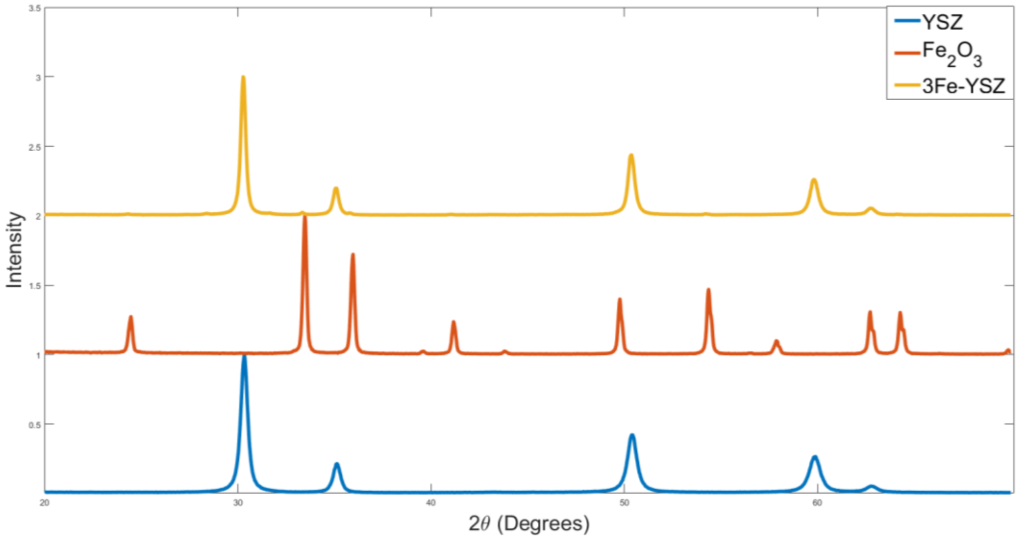

Figure 33: XRD spectra of Fe_2O_3 and YSZ precursors, before and after calcination.

5.3.2 GDC-infiltrated and Ni-GDC-infiltrated Ni-YSZ symmetric cells

GDC and Ni-GDC were infiltrated into the Ni-YSZ cermet electrodes to investigate the effects of MIEC infiltration into conventional cermet anodes. The goal was to see how temperatures, humidity level in the anode gas, and number of infiltration cycles affect overall anode performance. Cross-section SEM micrographs of Ni-YSZ cells infiltrated with GDC and Ni-GDC are shown in Fig. 34. The infiltrated cells all show the presence of a porous film coating the surface of the Ni-YSZ scaffold. While further infiltration does not change the morphology of the film, it does appear that Ni-GDC infiltration forms a more porous film than GDC. Although previous studies measured the electrochemical performance of the infiltrated cells, this study will try to obtain more mechanistic insight into the effects of the GDC porous film.

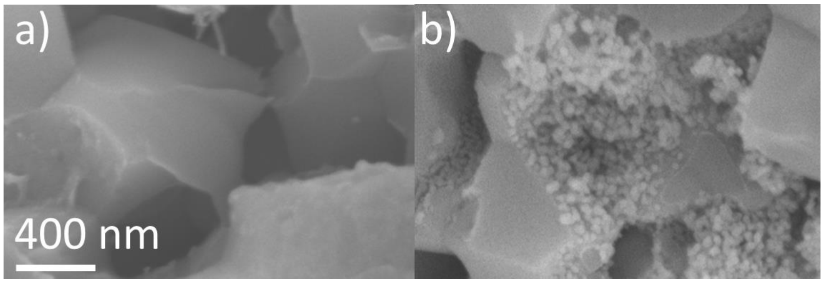

Figure 34: SEM fracture cross-sections of an a) uninfiltrated and b) GDC-infiltrated Ni-YSZ cell

The EIS data and the resultant DRT analysis of the tested baseline Ni-YSZ cell under can be seen in Fig. 35 which show how the polarization effects change with temperature and humidity. For the baseline Ni-YSZ cell, it is clear that the Nyquist plots consist of what appears to be a linear region at high frequencies, followed by a semicircle. Fig. 35a indicates that this semicircle grows larger in magnitude as operating temperature decreases, while Fig. 35b suggests that increasing humidity levels decrease the magnitude of the semicircle. The DRT analysis presented in Fig. 35c and 35d show the polarization processes consist of a large peak centered around 10-1000Hz, and a smaller peak centered around 2000-8000Hz. These peaks can be assigned to various polarization processes based on the transmission line model. The DRT analysis shows that the contributions of the RQ and Warburg elements are negligible because the peaks corresponding to these elements are very small. Thus, the contribution of these elements are insignificant compared to the contribution of the TLM element. As expected, the smallest polarization effects in the cell with the baseline cermet electrode is obtained at the highest temperature and at the highest humidity levels..

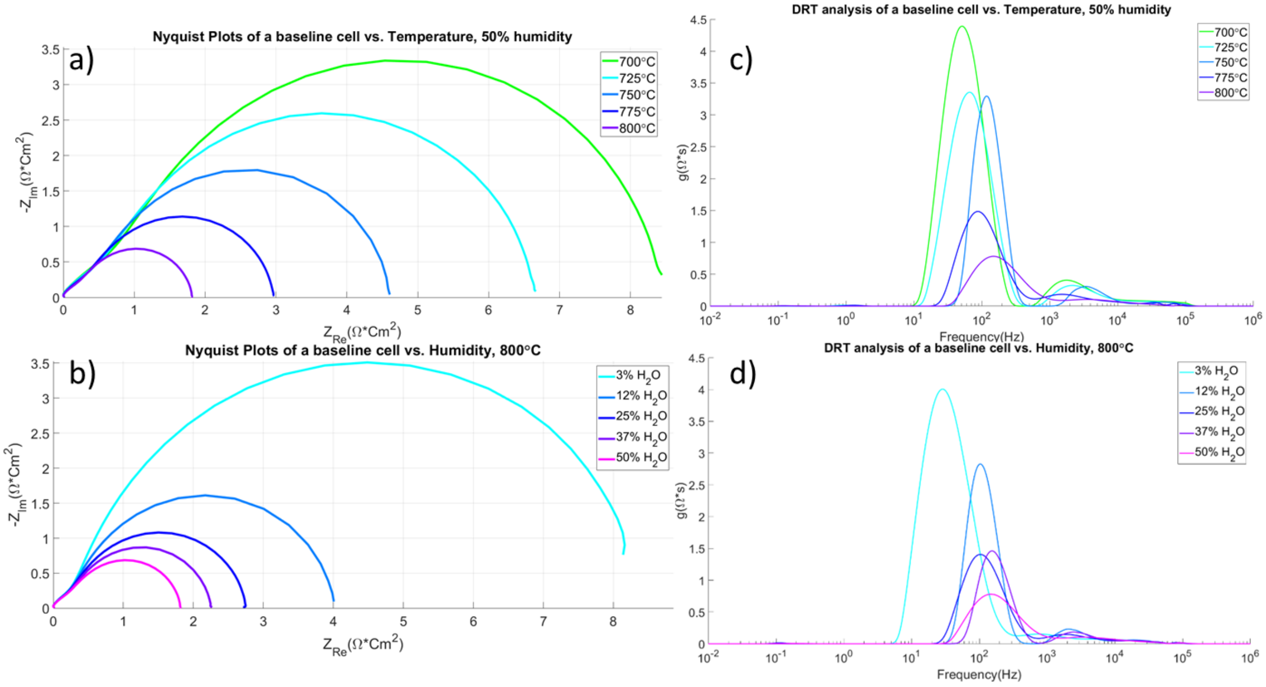

Figure 35: EIS performance with varying temperature (a) and humidity levels (b) for a baseline Ni-YSZ cell, with corresponding DRT analysis for temperature(c) and humidity (d).

The EIS data and the resultant DRT analysis of the GDC-infiltrated cell can be seen in Fig. 36. The cell suggests the presence of two main arcs formed by the polarization effects. Fig. 36a follows a similar trend to the uninfiltrated cell, but the magnitude of the polarization is an order of magnitude smaller. Whereas the humidity level of uninfiltrated cell greatly changes the magnitude of the polarization resistance, Fig. 36b shows the humidity level greatly affects the two arcs; changing the humidity from 3% to 12% results in a 90% decrease in polarization resistance. Further increasing the humidity leads to rapidly decreasing margin of improvements. In particular, increasing the humidity from 37% to 50% appears result in no change in the polarization resistance. The DRT analysis presented in Fig. 36c indicates the presence of four main peaks, two of which can be attributed to the TLM element discussed earlier, while the other two peaks overlapping around 1-10 kHz. As shown in the work of Sonn et al. [25] it appears that one peak is due to polarization due to the grain-boundary pseudocapacitance between the YSZ/YSZ grain boundaries, which is represented as RQ circuit element in the ECM. It is also worth noting this RQ element is also present in the uninfiltrated cell. Expanding on this logic, it is expected that the other peak could be attributed to the ionic resistance GDC/YSZ grain boundary, since it is very closely located in frequency. Further, this second peak is only present in the GDC-infiltrated cell lending further validity to the view that this represents the GDC/YSZ grain boundary resistance.

The reason the RQ peak is so prominent in Fig. 36c is due to the great decrease in the peaks related to the TLM element from, for example, 4 Ω*s to 0.12 Ω*s in the 700°C data. Both the TLM and RQ element are temperature dependent, and their polarization effects increase with decreasing temperature. The DRT analysis in Fig. 36d show the TLM and RQ elements do not vary much from 12% to 50% humidity (in general the magnitudes of the peaks are quite small compared to the uninfiltrated cells), but the low 3% humidity results in significant increases in peak magnitudes. It appears under moderate humidity, both elements are very small and not sensitive to changing humidity levels.

Table 4 compares polarization resistance for each cell tested at the extrema of operating conditions of temperature and humidity level in the fuel. At the same temperature and humidity levels, single infiltration of MIEC nanoparticles into anode compositions is sufficient to reduce the polarization resistance by greater than 80%. The resolution from the Zahner allows more accurate measurement of high frequency-data, and subsequently more precise data acquisition. Thus, it can be seen that these infiltrated cells have an 80% or greater decrease in polarization resistance.

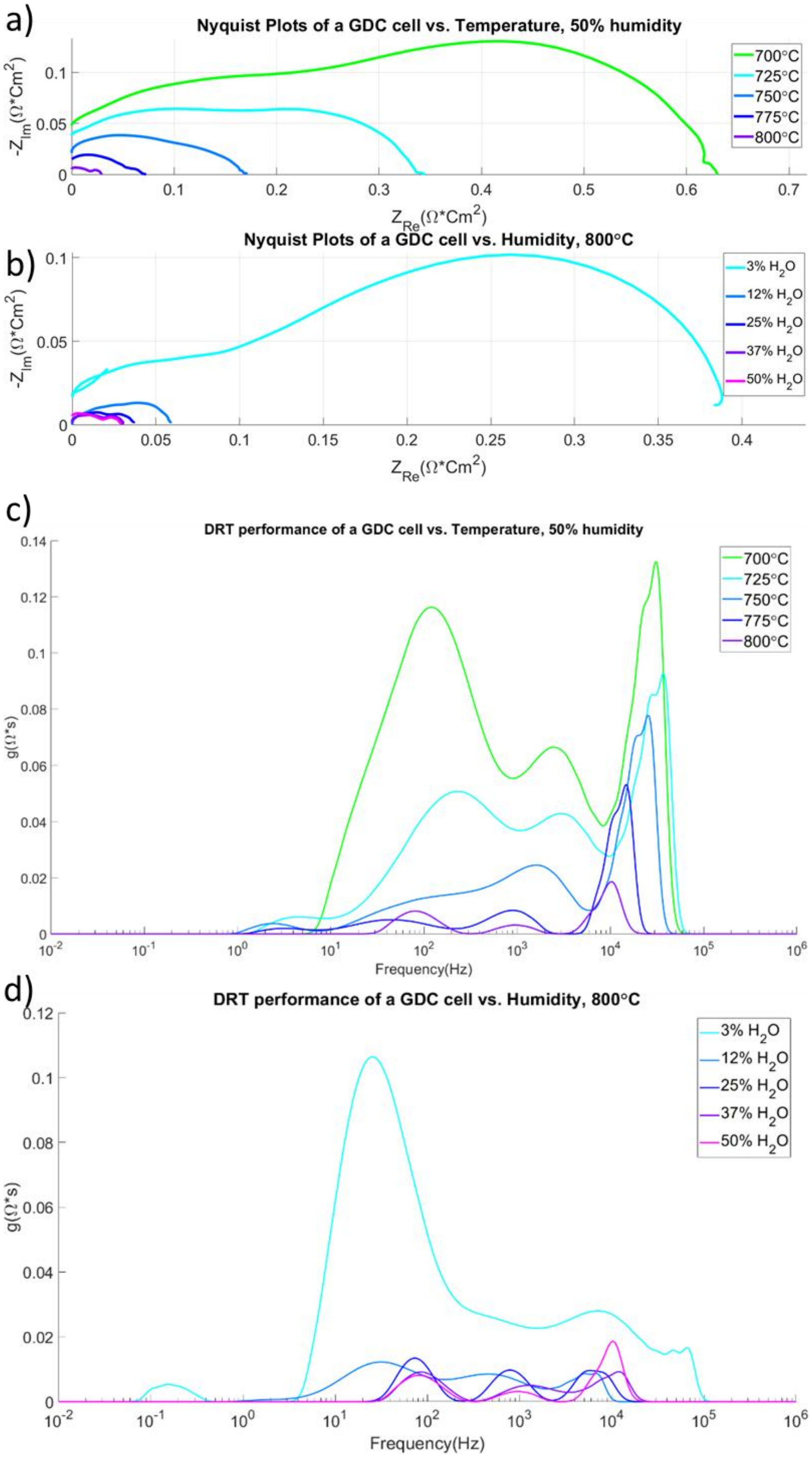
a) Nyquist Plots of a GDC cell vs. Temperature, 50% humidity

b) Nyquist Plots of a GDC cell vs. Humidity, 800°C

c) DRT performance of a GDC cell vs. Temperature, 50% humidity

d) DRT performance of a GDC cell vs. Humidity, 800°C

Figure 36: EIS performance with varying temperature (a) and humidity levels (b) for a GDC-infiltrated Ni-YSZ cell, with corresponding DRT analysis for temperature(c) and humidity (d).

Testing Humidity	Testing Temperature	AAL cermet composition	Infiltrant	Infiltration cycles	Polarization resistance ($\Omega.cm^2$)	Percent change compared to pristine baseline(%)
50% H_2O	700°C	Ni-YSZ	N/A	0	8.50	0%
			GDC	1	0.64	-92.4%
	800°C	Ni-YSZ	N/A	0	1.81	0%
			GDC	1	0.036	-98%
3% H_2O	800°C	Ni-YSZ	N/A	0	8.26	0%
			GDC	1	0.38	-95.3%

Table 4: Total polarization resistances of Ni-YSZ cells optimally infiltrated with GDC and Ni-GDC electrocatalysts, and the percent decrease in polarization versus the baseline uninfiltrated cell.

5.3.3 Ni-infiltrated Ni-FeYSZ Symmetric Cells

The performance of Ni-FeYSZ cermet electrodes were measured in humidity levels ranging from 3% to 50%. The changes in the surface area coverage of Ni nanoparticles, Ni nanoparticle density, and added TPB length as a function of infiltration cycles in tested cells are shown in Fig. 37 for cermet electrodes containing YSZ, TiYSZ and FeYSZ as the ionic conducting phase. Fig. 37a shows the surface area fraction of ionic phase adjacent to pores that are covered with Ni nanoparticles as function of infiltration cycles, Fig. 37b the number density of Ni nanoparticles on the ionic phase adjacent to the pores as a function of infiltration cycles, and Fig. 37c the added TPBs in the samples as a function of infiltration cycles. As with the other anode cermet electrodes, the infiltration of Ni into Ni-FeYSZ increases surface coverage, nanoparticle density and added TPBs with subsequent infiltration cycles, which should correlate with increasing cell performance.

The EIS data and the resultant DRT analysis of the baseline Ni-FeYSZ cell can be seen in Fig. 38. It is clear that the overall shapes of the impedance spectra are most similar to the Ni-YSZ baseline data, however the resistance in Ni-FeYSZ is around twice as large. DRT analysis indicates the majority of the polarization can be attributed to the TLM element, however new peaks around at 0.1-1Hz and 10-100kHz are more prevalent in the Ni-FeYSZ cermet. The general trend is that the polarization effects decrease with increasing humidity, and increasing temperature in uninfiltrated Ni-FeYSZ cermet anodes, as was the case with the Ni-YSZ cermets. The EIS data and the resultant DRT analysis of the optimally infiltrated Ni-FeYSZ cell (which has been infiltrated once) can be seen in Fig. 39. It is clear that the overall polarization resistance shapes are most similar to the Ni-YSZ baseline data, however the resistance in Ni-FeYSZ is around twice as large. DRT analysis indicates the majority of the polarization can be attributed to the TLM element, however new peaks around at 0.1-1Hz and 10-100kHz are more prevalent in the Ni-FeYSZ cermet. The general trend is that the polarization effects decrease with increasing humidity, and increasing temperature in uninfiltrated Ni-FeYSZ cermet anodes.

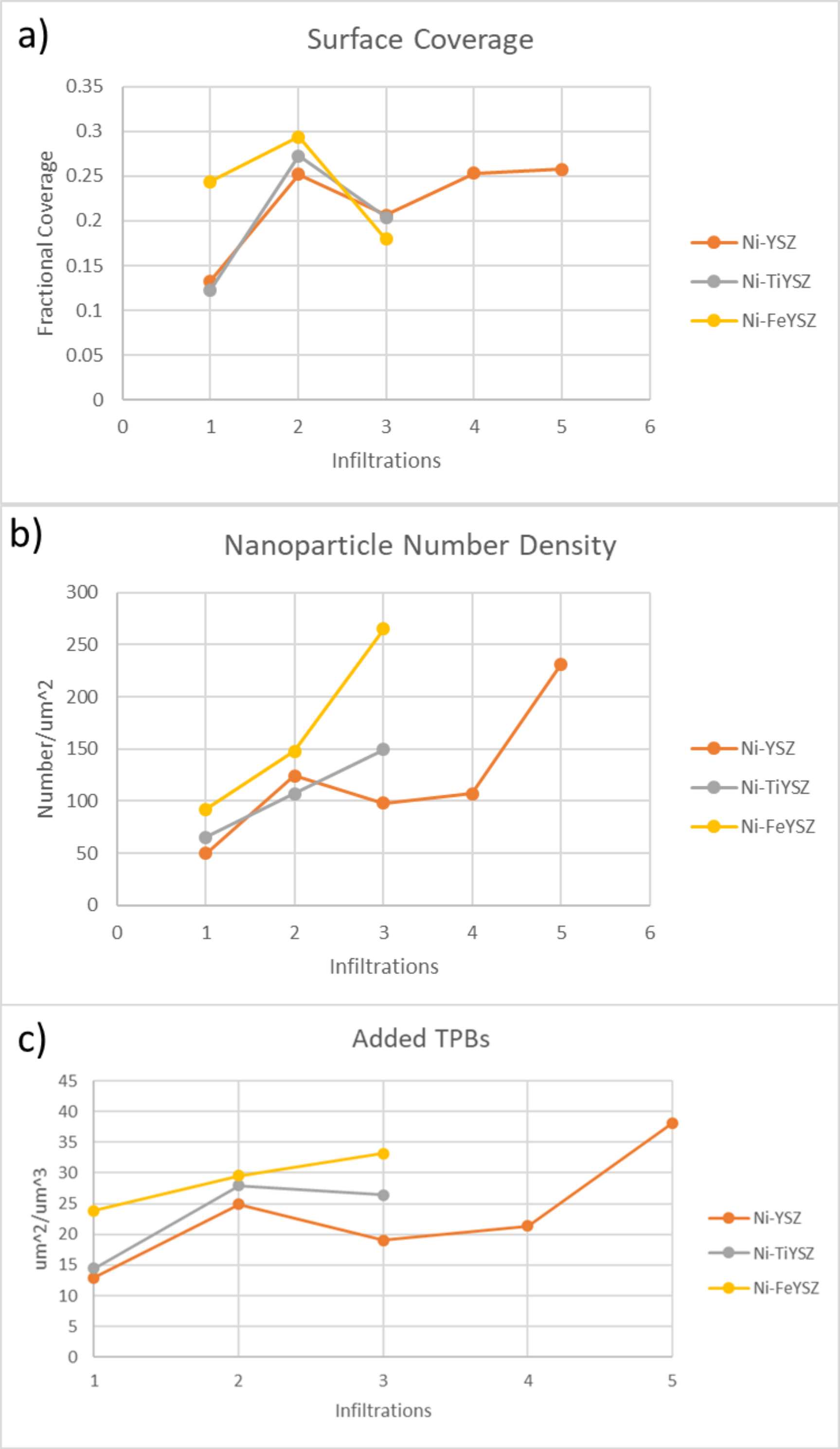

Figure 37: a) Surface area fraction of YSZ/TiYSZ/FeYSZ grains adjacent to pores covered by Ni nanoparticles, b) number density of Ni nanoparticles on YSZ/TiYSZ/FeYSZ surface adjacent to pores, and c) added TPB density, as a function of infiltration cycles.

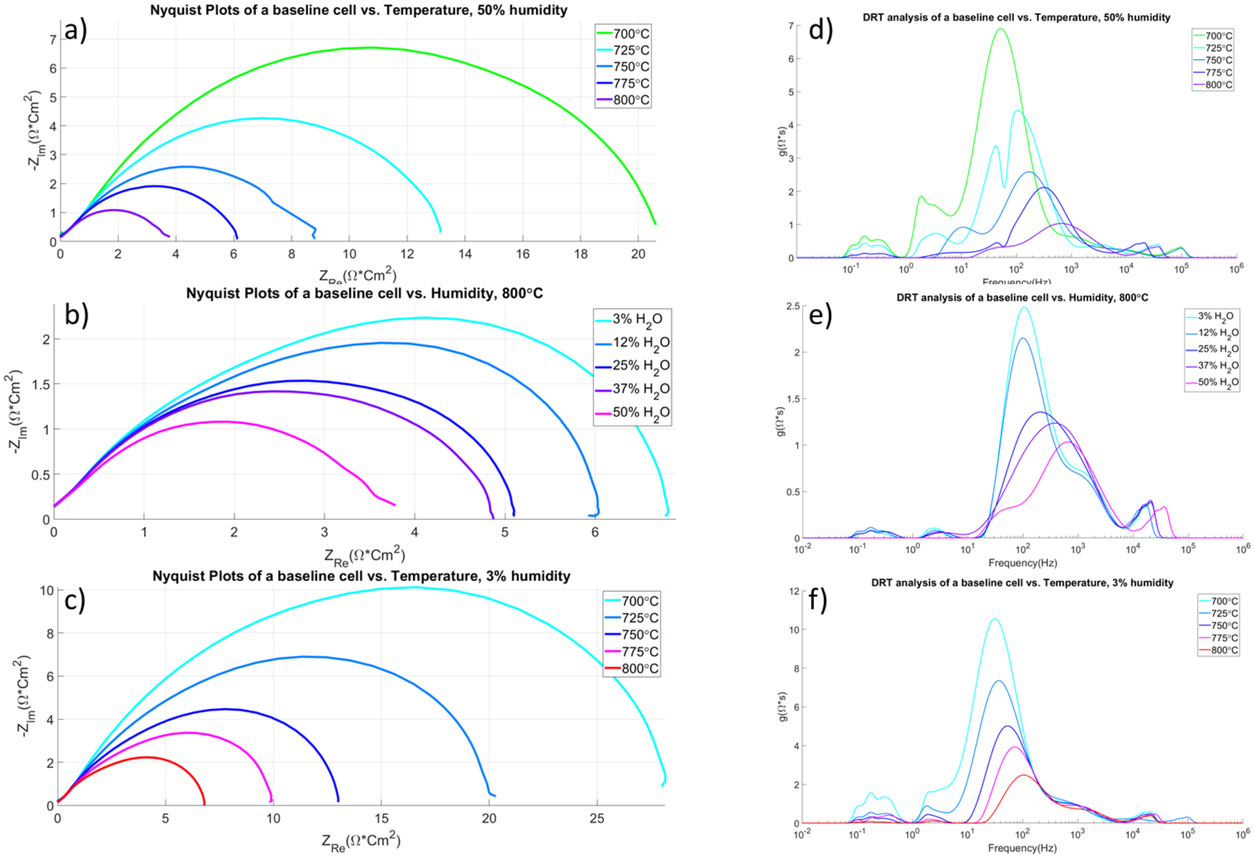

Figure 38: EIS performance with (a) varying temperature at 50% humidity, (b) varying humidity levels at 800°C and (c) varying temperature at 3% humidity for a baseline Ni-FeYSZ cell, with corresponding DRT analysis adjacent to each graph (d-f).

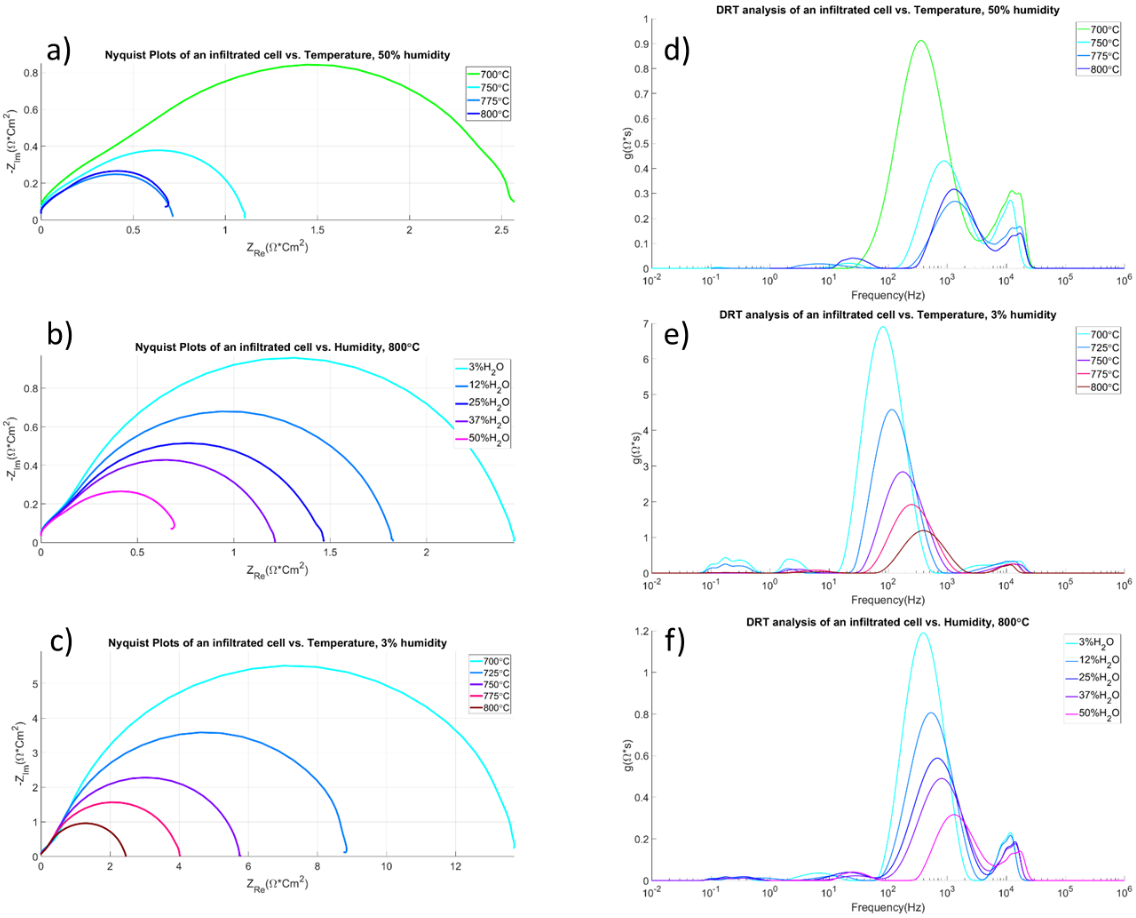

Figure 39: EIS performance with (a) varying temperature at 50% humidity, (b) varying humidity levels at 800°C and (c) varying temperature at 3% humidity for an optimally infiltrated Ni-FeYSZ cell, with corresponding DRT analysis adjacent to each graph (d-f).

Table 5 summarizes the total decrease in polarization resistance for the tested and infiltrated Ni-FeYSZ cells. All EIS data is compared to the baseline Ni-YSZ cell in Table 4, column 5. If we compare the three different infiltration cycles, the effect of infiltration improves the cell under all conditions, except under 50% humidity conditions for the 3-cycle infiltrated cells; the polarization resistance is worse compared to the lesser loading in other tested cells. However, under the lowest level of humidity in the fuel, 3%, more infiltration appears to improve the polarization resistance. Despite the conflicting data, it is clear one single infiltration cycles of Ni provides the optimal results in Ni-FeYSZ, as it provides the most improvement with the least amount of additional steps. Overall, the results for infiltrated Ni-FeYSZ can be compared with infiltrated Ni-TiYSZ from Table 2, which shows the former could be an even better anode cermet candidate at lower temperatures.

Testing Humidity	**Testing Temperature**	**Infiltration cycles**	**Polarization resistance (Ω.cm^2)**	**Polarization resistance in uninfiltrated Ni-YSZ (Ω.cm^2)**	**Percent change compared to uninfiltrated Ni-YSZ (%)**
3% H_2O	700°C	0	28.16	N/A	
		1	13.68		
		2	9.62		
		3	8.02		
	800°C	0	6.79	8.26	-17.8%
		1	2.453		-70.3%
		2	2.07		-75.7%
		3	1.91		-76.9%
50% H_2O	700°C	0	20.76	8.50	+144.2%
		1	2.55		-70%
		2	2.27		-73.3%
		3	9.24		+8.7%
	800°C	0	3.787	1.81	+109.2%
		1	0.71		-60.8%
		2	1.01		-44.2%
		3	1.393		-23.0%

Table 5: Total polarization resistances of Ni-FeYSZ cells infiltrated with Ni and the percent decrease in polarization versus the baseline uninfiltrated Ni-YSZ cell from Table 4.

5.3.4 Equivalent Circuit Model analysis of GDC-infiltrated cells

The plots of the TLM variables (f_{rxn}, R_O and R_{rxn}) with tested Ni-YSZ cells (uninfiltrated, infiltrated GDC) are shown in Fig. 40. As expected, GDC infiltrated cells show trends in these variables indicating better overall cell performance under all tested conditions compared to uninfiltrated cells; these include higher f_{rxn}, lower R_{rxn} and lower R_O. The surface reaction frequency, R_{rxn}, affects the polarization resistances magnitude more than R_O, and lowering both indicate a better overall anode cermet. Fig. 40b and 40e show that the GDC-infiltrated cell shows a decreasing R_{rxn} with temperature, but with a slightly steeper slope; at lower temperatures, GDC may not provide any more improvement than the baseline cell. The humidity level shows that decreasing humidity increases the R_{rxn} in these cells; this suggests the charge transfer reactions involved with GDC also utilize water vapor as a reactant, perhaps in an intermediary step. As for R_O, the inclusion of GDC decreases the oxygen resistivity. Lastly, Fig. 40c suggests that with GDC R_O decreases with increasing temperature.

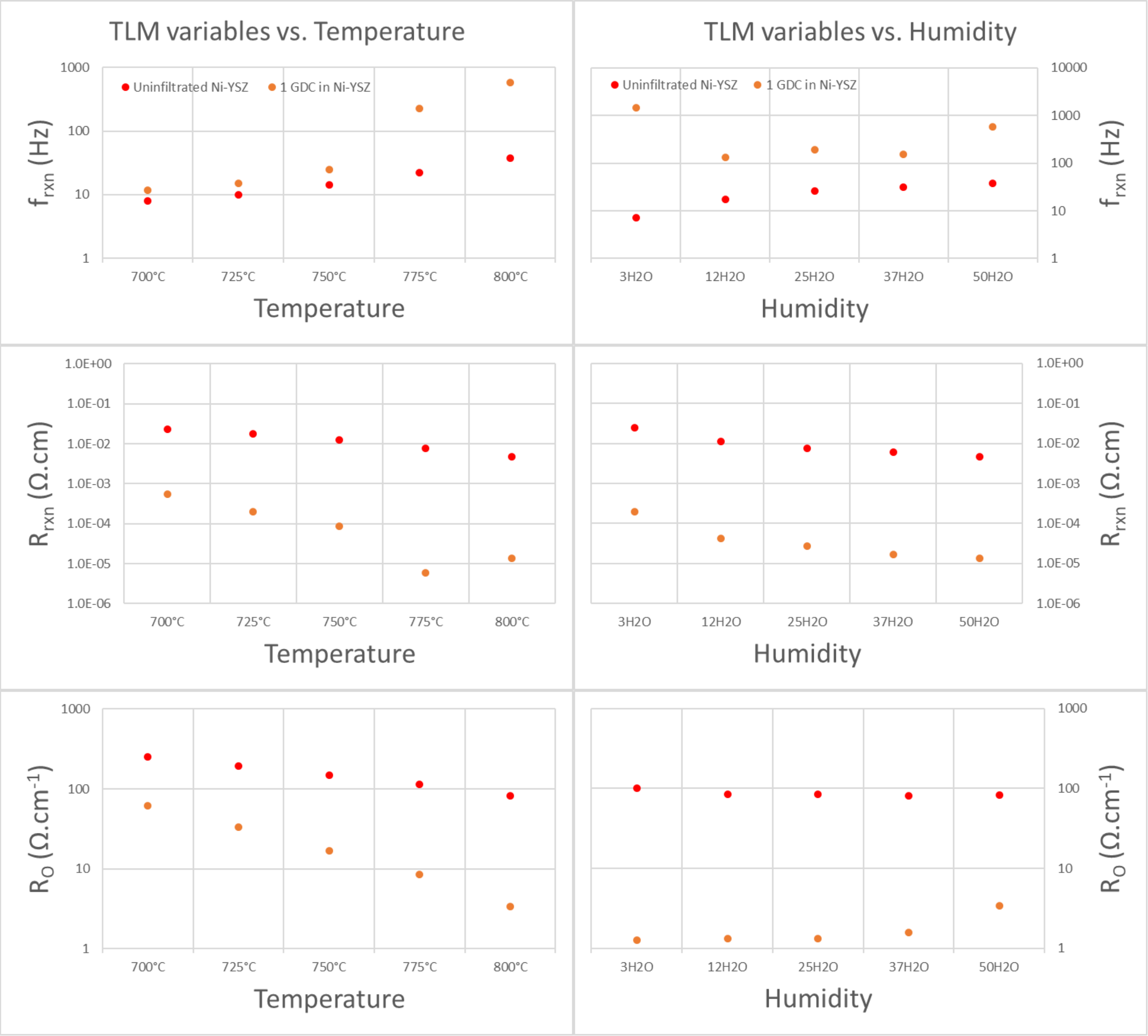

Figure 40: TLM variables f_{rxn} (a), R_{rxn} (b) and R_O (c) as a function of temperature and humidity(d-f) for uninfiltrated and GDC-infiltrated Ni-YSZ cells.

5.3.5 Equivalent Circuit Model analysis of Ni-infiltrated cells

Similar to the TLM elements plotted for Ni-TiYSZ in Fig. 27, the plots of the TLM variables (f_{rxn}, R_O and R_{rxn}) with Ni-infiltrated Ni-FeYSZ are shown in Fig. 41; Figures 41d-f also include the effects of humidity, along with temperature. Again, the use of an MIEC as the cermet ionic phase alongside Ni infiltration greatly improve the cells’ performance. While the single infiltration seems to give the best performance with the least R_{rxn} under most temperature and humidity conditions, the 2-cycle Ni infiltrated cell appears to have similar performance, with better R_O under all temperatures. The increase of R_O and R_{rxn} in the 3-cycle Ni infiltrated cell shows a reversal in the polarization effects. This appears to contradict Fig. 37 and the hypothesis that increasing the TPB density should decrease polarization resistance. As for the effects of humidity on infiltrated cells, the magnitude of R_{rxn} appears to decrease with increasing humidity, while the value of R_O remains fairly constant; there appears to be a visible decrease in R_O when compared to the uninfiltrated cell. Fig. 42 includes TLM elements of the Ni-FeYSZ cells at 3% humidity under varying operating temperatures, after exposure to 50% humidity. While infiltration does improve cell performance, the 3-cycle Ni infiltrated cells appear to have the best performance, with higher f_{rxn} and lower R_O, and R_{rxn} values under this subset of conditions. The phenomena behind these results will also be explored in a later section. Lastly, when compared to the values found in Fig. 42, the infiltrated Ni-FeYSZ cells appear to have lower polarization resistances than their infiltrated Ni-TiYSZ counterparts, indicating Fe_2O_3 may be a more effective transition metal dopant than Ti in YSZ.

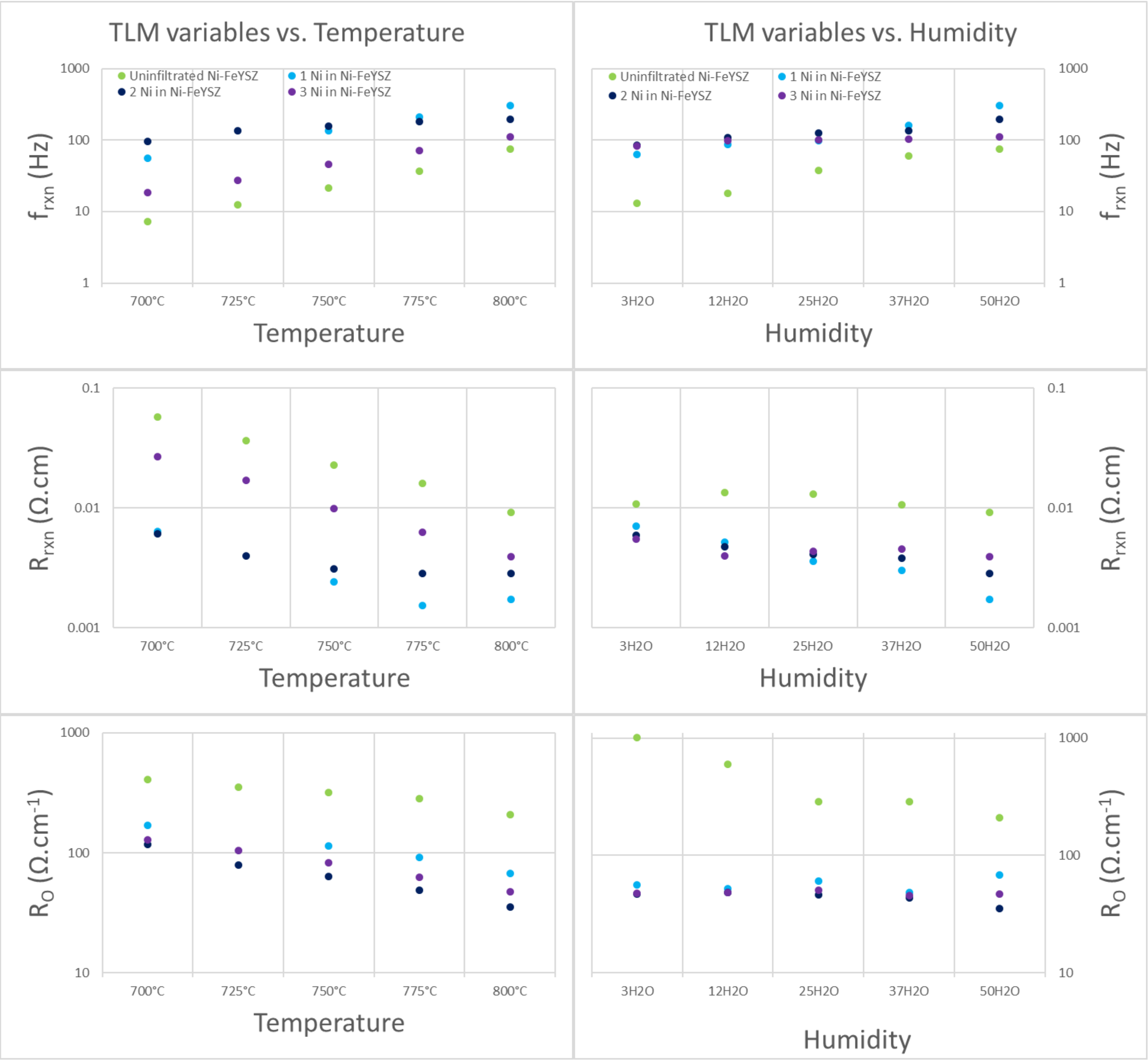

Figure 41: TLM variables f_{rxn} (a), R_{rxn} (b) and R_O (c) as a function of temperature and humidity(d-f) for uninfiltrated and Ni-infiltrated Ni-FeYSZ cells.

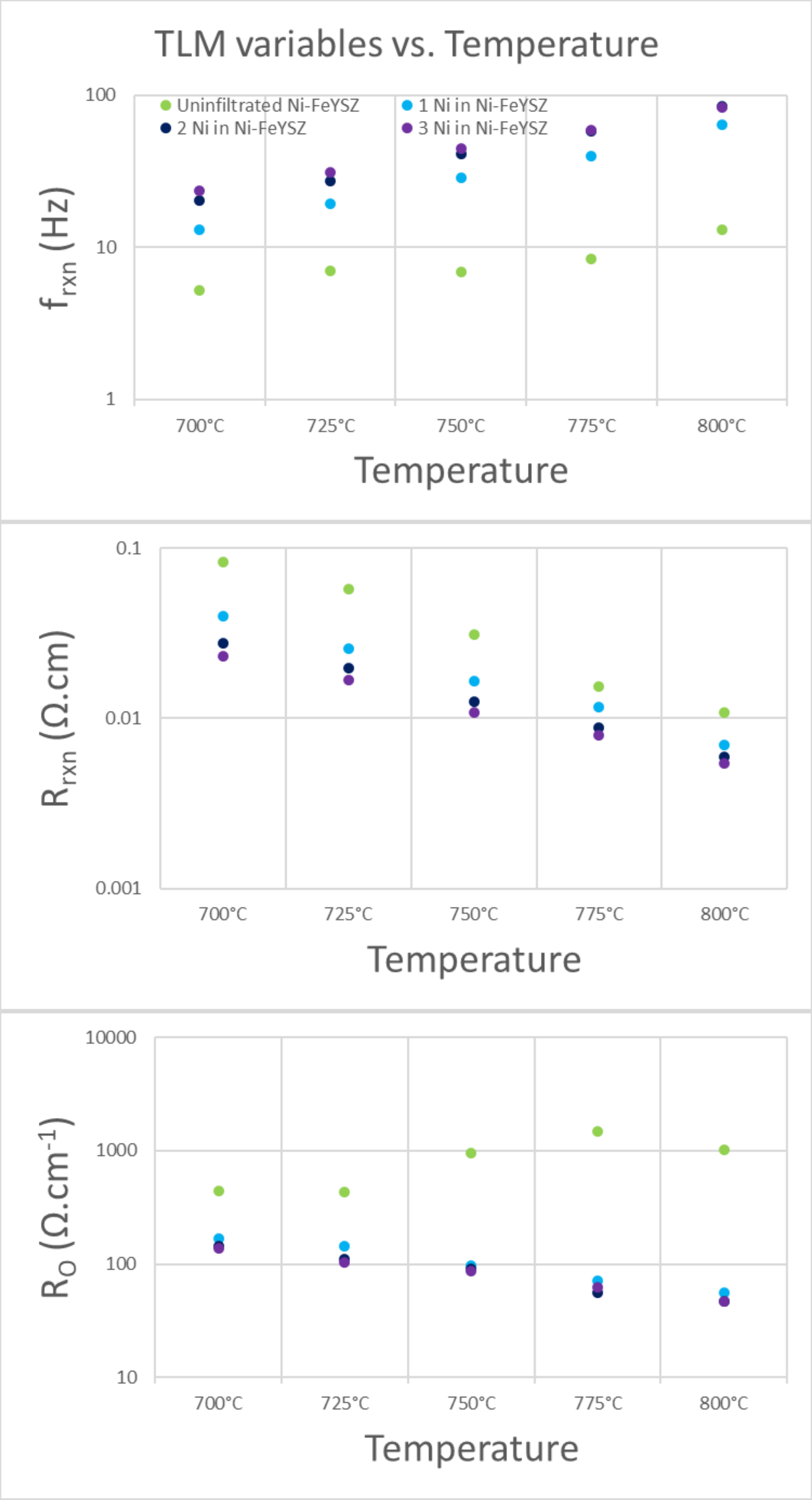

Figure 42: TLM variables f_{rxn} (a), R_{rxn} (b) and R_O (c) at 3% humidity as a function of temperature for uninfiltrated and Ni-infiltrated Ni-FeYSZ cells.

5.4 Conclusions

In this work, electrolyte supported symmetric cells, consisting of infiltrated and uninfiltrated Ni-YSZ and Ni-FeYSZ cells were fabricated, electrochemically tested, and analyzed as a function of operating temperature and humidity level. Ni-YSZ cells were infiltrated with compositions containing MIECs, such as GDC, while Ni-FeYSZ cell were infiltrated with only Ni. Both types of infiltrated cells utilized a mixed conductor in the predominantly ionic conducting phase. This was found to decrease the overall polarization of the cell. More specifically, DRT analysis and fitting of the ECM to the TLM elements have shown that the majority of the polarization resistance contributions can be attributed to R_{rxn}. For Ni-YSZ cells, the addition of GDC nanostructures into the cermet scaffold have shown to decrease the TLM polarization resistance, which also improves with increasing humidity. The addition of both Ni and GDC nanoparticles imparts some improvements in cell performance. The greater decreases in R_{rxn} at lower temperatures in cells with infiltrants suggest that the infiltrants have a greater effect in reducing polarization resistance at lower temperatures. For Ni-FeYSZ cells, infiltration is a necessary step to lower the polarization resistance. While subsequent infiltration cycles improve cell performance at extremely low humidity, just one cycle of infiltration appears to result in optimal cell performance under a majority of conditions. The introduction of more reaction sites, coupled with the introduction of electronic conductivity in the FeYSZ, allow the otherwise inactive and distant grains and nanoparticles to become electrochemically active.

6. CONCLUSIONS

The role of infiltration and mixed ionic and electronic conduction in the predominantly ionic phase of cermet electrodes has been explored using symmetrical cells. The optimum number of infiltration cycles of each infiltrant were also identified. In total, three types of cermet electrodes were infiltrated. Ni-YSZ cermet electrodes were infiltrated with nanoparticle solutions containing Ni, Ni-GDC and GDC nitrates. Ni-TiYSZ and Ni-FeYSZ, cermet electrodes which have transition metals doped into the ionic phase, were solely infiltrated with Ni nanoparticles. Table 6 compares the performance of the baseline Ni-YSZ cell with the optimally Ni-infiltrated cermet anodes. The infiltrated Ni-MIEC cermets outperform uninfiltrated Ni-YSZ cermets, and the infiltrated Ni-YSZ cells under average fuel utilization conditions (i.e. 50% H_2O). However, its superiority over optimally Ni-infiltrated YSZ is not clear under fuel rich conditions, i.e. under the 3% humidity condition. Ni-TiYSZ and Ni-FeYSZ cermets outperform Ni-YSZ at the higher 50% humidity condition, but only infiltrated Ni-FeYSZ shows significant improvement at lower temperatures and humidity conditions compared to infiltrated and uninfiltrated Ni-YSZ. This suggests further exploration into the use and characterization of infiltrated FeYSZ cermet electrodes.

Testing Humidity	Testing Temperature	Cermet Anode	Optimally Ni-Infiltrated Polarization resistance (Ω.cm^2)	Polarization resistance in uninfiltrated (and optimally Ni-infiltrated) Ni-YSZ (Ω.cm^2)	Percent change compared to uninfiltrated (and optimally Ni-infiltrated) Ni-YSZ (%)
50% H_2O	700°C	Ni-TiYSZ	4.14	10.57 (4.69)	-60.8% (-11.7%)
		Ni-FeYSZ	2.55		-75.9% (-45.6%)
	800°C	Ni-TiYSZ	0.78	1.95(0.97)	-60% (-19.6%)
		Ni-FeYSZ	0.71		-63.6% (-26.8%)
3% H_2O	700°C	Ni-TiYSZ	25.69	56.91(20.8)	-54.9% (+23.5%)
		Ni-FeYSZ	13.68		-76% (-34.2%)
	800°C	Ni-TiYSZ	1.56	5.48(1.21)	-71.5% (+29.9%)
		Ni-FeYSZ	2.45		-55.3% (+102.5%)

Table 6: Total polarization resistances of optimally Ni-infiltrated Ni-FeYSZ and Ni-TiYSZ cells and percent decrease in polarization resistance versus the baseline uninfiltrated and optimally Ni-infiltrated Ni-YSZ cell.

It is clear that infiltration increases the TPB density in cermet electrodes, and the new active TPB sites increase the overall reaction rate in the cermet, resulting in a decrease in activation polarization resistance and an increase in the cell performance. While it took 3 cycles of Ni infiltration to optimally infiltrate the Ni-YSZ cell, the Ni-FeYSZ and Ni-TiYSZ cells only required one cycle of infiltration to reach optimal performance under most conditions. This clearly shows that introduction of electronic transport in the YSZ by doping with transition metal ions activates distant and physically separated nickel nanoparticles. These effects are even more clearly seen in GDC and Ni-GDC which showed the best cell performance with 2 infiltration cycles. In the case of GDC and Ni-GDC, most of the decrease in polarization resistance can be attributed to the first cycle of infiltration. We conclude that while cermet compositions containing solely Ni and YSZ phases require multiple nickel nanoparticle infiltration cycles to reach their best performance, the incorporation of mixed ionic and electronic conduction reduces the number of required infiltration cycles to optimally reduce the polarization resistance to just one.

The DRT and ECM analysis has shown the majority of the polarization resistance is attributable to the TLM element for the cermet electrode, which models both the charge transfer reaction on the scaffold surface and the oxygen ion resistivity in the ionic phase. The former reaction plays a much larger role in the TLM compared to the latter, and it is necessary to minimize it to achieve better cermet performance. This can be noted in the ECM analysis of the three uninfiltrated cermets. While the MIEC ionic phases of FeYSZ and TiYSZ have lower ionic conductivity, as well as higher oxygen ion resistivity than the YSZ phase, any increasing polarization resistance from the slower ionic transport kinetics is outweighed by the decreased surface charge transfer resistance once infiltration is applied. The infiltration of Ni-GDC and GDC decrease both R_{rxn} and R_O of symmetric cells featuring the infiltrated cermet, with the least polarization resistance under all tested conditions.

A clearer picture of how the nanoparticles improve the cell under different operating conditions has emerged from this work. To begin, Ni nanoparticles on the YSZ scaffold contiguous with the pore phase form new TPBs, but these new TPBs may not be active if there is no electronically conducting scaffold nearby to receive the electrons resulting from electrochemical reactions. Fig. 19 and 37 show the increase of TPB and nanoparticle density alone do not result in an increase in performance. This implies that multiple cycles of Ni infiltration were necessary in Ni-YSZ cermets to create higher connectivity of nanoparticles on the YSZ scaffold. However, while further infiltration cycles seem to further increase reaction sites and nanoparticles, the polarization resistance does not decrease, and instead further increases. This suggests that beyond the optimum number of infiltration cycles, there is a greater increase of increasing the number of inactive TPBs. A combination of mechanisms leading to Ni nanoparticle coalescence, reduction in TPBs, leading to less overall connectivity of the entire electronic scaffold may be at play. To mitigate this coarsening it is important to reduce number of infiltration cycles and reduce the nanoparticle density. The incorporation of the MIEC phase into the ionic scaffold can be used alongside infiltration to reduce the required nanoparticle density and produce better performing cermet anodes.

Uninfiltrated cermet electrodes featuring MIEC phases, i.e. those with a Ni-MIEC scaffold, perform worse than Ni-YSZ. due to the higher R_{rxn} and R_O, suggesting worse connectivity and more sluggish ionic transfer in Ni-MIEC cermets. But infiltration of Ni-MIEC cermets introduces new TPBs which are all active, as there is an electronic pathway through the MIEC scaffold. It seems no matter the greater distance the nanoparticles are from the percolated scaffold, they are all able to contribute to the overall reaction due to the presence of this electronic transport pathway. This is seen most clearly in Fig. 42, where additional infiltration cycles result in better performance at extremely low humidity conditions. However, the effects of increasing humidity levels appear to lower overall cell performance, and may suggest that the increased number of nanoparticles may cause too much wetting on the MIEC scaffold, and ultimately reduce TPB density.

In general, the role of increasing the density of active TPBs appears to decrease R_{rxn} in the TLM element, especially at lower temperatures. A doped ionic scaffold is able to activate more nanoparticle TPBs, which may explain why Fig. 37 and Table 5 show further infiltration cycles result in better performance, at least for the 3% humidity levels. The introduction of more active TPBs can improve electrocatalysis, decrease the overall charge transfer resistance in our transmission line representation of the cermet scaffold, the largest contributor to polarization resistance at intermediate temperatures.

A single Ni infiltration cycle into Ni-MIECs cermets is sufficient to obtain better performance than Ni-YSZ. Through a survey of the SOFC literature, it has been found that multiple groups have also incorporated transition metals into their compositions, albeit as sintering aids rather than ionic phase dopants [22, 72-78]. In our work, we have shown that the addition of transition metal has tangible electrochemical benefits. Thus, the replacement of the YSZ phase in the Ni-YSZ anode by a transition-metal-doped-YSZ phase coupled with Ni infiltration may be a promising pathway to obtain high performance anodes.

While the MIEC in the ionic scaffold has been shown to improve infiltrated cells, it appears the MIEC phase being used as an infiltrant in the standard Ni-YSZ cermet anode greatly improves cell performance by decreasing the resistance associated with the TLM element, as well as overall cell polarization resistance. GDC under reducing environments can facilitate the transfer of both electrons as well as oxygen ions. Looking at the changes associated with the GDC phase within the cermet electrode, the porous film appears to provide not only improved connectivity of the metallic scaffold to other grains, but the entire GDC surface appears to become active electrochemical reaction sites, and allow at least some intermediate steps related to the overall charge transfer reaction to occur. Unlike the TPBs which consist of narrow centerlines where the three phases meet, the GDC surface can react directly with the pore phase to allow charge transfer as well as transport oxygen ions to the GDC/pore interface. The DRT analysis of Ni-YSZ cells containing GDC loading show the TLM element suppressed to a level where the higher 10kHz peak dominates the overall cell polarization. This high frequency (HF) peak has been reported before to be associated with the oxygen ion transport resistivity associated with YSZ/YSZ grain boundaries. While the addition of GDC/YSZ interfaces may improve oxygen ion conductivity by allowing more ionic species to react at the GDC surface, it is unknown whether it directly decreases this HF process and its polarization resistance. As shown in Fig. 34 the TLM element and HF peak magnitudes grow with decreasing temperature, yet remains fairly stable at medium levels of humidity; in fact, these peaks sharply jump with the transition to extremely low humidity levels, indicating that humidity plays a greater role in the electrochemical reaction of H_2 on the GDC/pore interface.

It should also be noted that the Ni-GDC cells also have unusual yet better performance. Microstructural analysis shows the Ni-YSZ scaffold covered by an even more porous film, with hemispherical nanoparticles dispersed either on top of the film or between the pores of the film itself. While the detailed mechanisms in the case of Ni-GDC infiltrated nanoparticles are not clear, the TPBs created by these nanoscale features have a direct electronic pathway through the scaffold via the GDC film.

7. FUTURE WORK

Enhancement of electrocatalysis through infiltration is a nuanced process, especially if the infiltrant results in multiple infiltrated phases. Unlike prior work which report infiltrated GDC nanoparticles to appear as individual hemispheres, the electrodes in this work exhibited microstructures where the GDC appeared as a connected porous film. While GDC has shown to improve the baseline Ni-YSZ cell under all conditions, it is possible that the infiltration of Ni-GDC may show even better performance at lower temperatures, which should be explored. Additionally, GDC in addition to being an excellent MIEC is an excellent electrocatalyst in its own merit. Thus, carefully designed experiments that deconvolute the role of electrocatalysis and mixed conduction in infiltrated anodes containing multiple phases such as Ni and GDC should be explored. Designing infiltrated cermet anodes containing different volume fractions of Ni and GDC and comparing the microstructural changes along with DRT analysis of electrochemical data may further elucidate how reaction sites from the added Ni and GDC each impact cermet performance.

Further improvements in microstructural analysis is necessary. Lu et. al. as well as other groups have demonstrated that FIB-SEM is an imaging method which can be used to obtain microstructural data in cermet electrodes filled with epoxy [15, 56, 66, 75, 83]. Currently, our lab members are also developing a method based on FIB-SEM in which Ni infiltrated cermet anodes can be imaged without the need for epoxy, and allow 3D reconstruction of the cermet with intact nanoparticles. Additionally, there have been no 3D reconstruction studies of GDC-infiltrated scaffolds. As previously mentioned, the morphology of infiltrated GDC in our studies is quite different from prior studies, and 3D reconstruction studies that can reveal the morphology and distribution of GDC in the cermet could play a key role in understanding the role of GDC in electrocatalysis and mixed conduction. With better resolution and detection of these nanoscale features, the composition and microstructure of infiltrated electrodes could be engineered to mitigate cell degradation by addressing the primary mechanisms responsible.

The inclusion of infiltration as a processing step may also allow new cermet compositions to be explored. The use of GDC as a film that connects isolated Ni grains could allow the cermet to maintain high performance and counteract Ni losses at higher temperatures. Alternatively, the GDC film could serve as a supplementary scaffold, which allows the use of less Ni in the cermet scaffold and still work as a percolated electronic network. The addition of a small amount of GDC loading could allow the fabrication of anode active layers which have much slower degradation and lower cost.

APPENDIX 1: DRT Trasformation

The code below transforms the discrete EIS spectra into a continuous function which acts as the DRT transformation.

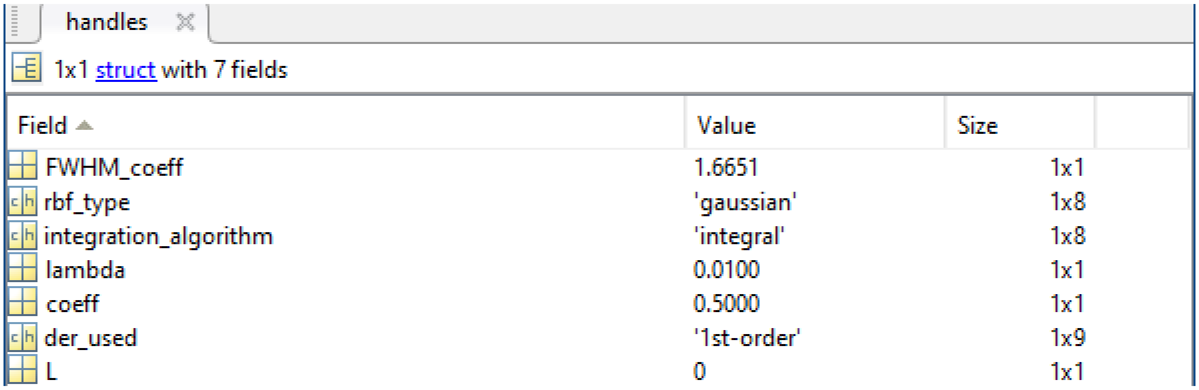

1x1 struct with 7 fields

Field	Value	Size
FWHM_coeff	1.6651	1x1
rbf_type	'gaussian'	1x8
integration_algorithm	'integral'	1x8
lambda	0.0100	1x1
coeff	0.5000	1x1
der_used	'1st-order'	1x9
L	0	1x1

Figure 43: The handles structure used perform the necessary Radial Basis Funtion transformations onto the EIS spectra to obtain the final DRT transformation.

```
function handles = DRT_Test(handles)
handles.lb_im = zeros(numel(handles.freq)+2,1);
handles.ub_im = Inf*ones(numel(handles.freq)+2,1);
handles.x_im_0 = ones(size(handles.lb_im));
handles.lb_re = zeros(numel(handles.freq)+2,1);
handles.ub_re = Inf*ones(numel(handles.freq)+2,1);
handles.x_re_0 = ones(size(handles.lb_re));
handles.taumax=ceil(max(log10(1./handles.freq)))+1;
handles.taumin=floor(min(log10(1./handles.freq)))-1;

handles.options =optimset('algorithm','interior-point-
convex','Display','off','TolFun',1e-15,'TolX',1e-10,'MaxFunEvals', 1E5);

handles.b_re = real(handles.Z_exp);% experimental
handles.b_im = -imag(handles.Z_exp);
handles.delta = mean(diff(log(1./handles.freq)));
handles.epsilon  = handles.coeff*handles.FWHM_coeff/handles.delta;
 handles.freq_out = logspace(-handles.taumin, -handles.taumax,
10*numel(handles.freq));
    handles.A_re = assemble_A_re(handles.freq, handles.epsilon, handles.rbf_type,
handles.integration_algorithm);
    handles.A_im = assemble_A_im(handles.freq, handles.epsilon, handles.rbf_type,
handles.integration_algorithm,handles.L);
    handles.M_re = assemble_M_re(handles.freq, handles.epsilon, handles.rbf_type,
handles.der_used);
    handles.M_im = assemble_M_im(handles.freq, handles.epsilon, handles.rbf_type,
handles.der_used);
    % need L and der_used
[H_re,f_re] = quad_format(handles.A_re, handles.b_re, handles.M_re, handles.lambda);
[H_im,f_im] = quad_format(handles.A_im, handles.b_im, handles.M_im, handles.lambda);
[H_combined,f_combined] = quad_format_combined(handles.A_re, handles.A_im,
handles.b_re, handles.b_im, handles.M_re, handles.M_im, handles.lambda);
warning('off')

handles.x_ridge_combined = quadprog(H_combined, f_combined, [], [], [], [],
handles.lb_re, handles.ub_re, handles.x_re_0, handles.options);
```

```
handles.gamma_ridge_combined_fine = map_array_to_gamma(handles.freq_out, handles.freq,
handles.x_ridge_combined(3:end), handles.epsilon, handles.rbf_type);
handles.gamma_ridge_combined_coarse = map_array_to_gamma(handles.freq, handles.freq,
handles.x_ridge_combined(3:end), handles.epsilon, handles.rbf_type);
end
```

APPENDIX 2: ECM analysis and fitting

The codebase below generates a MATLAB GUI which can fit EIS data from Nyquist and Bode plots into an ECM model. The model below is shown in Fig. 41, consisting of an R_Ohm resistor, a 1-10kHz RQ element, a 1-10Hz finite-length Warburg element, and a mid-frequency TLM element. Results from each EIS fitting are logged and saved into a .mat file for further post-processing. The code does not require any batch fitting, and utilizes visual inspection over educated guessing to fine-tune parameters.

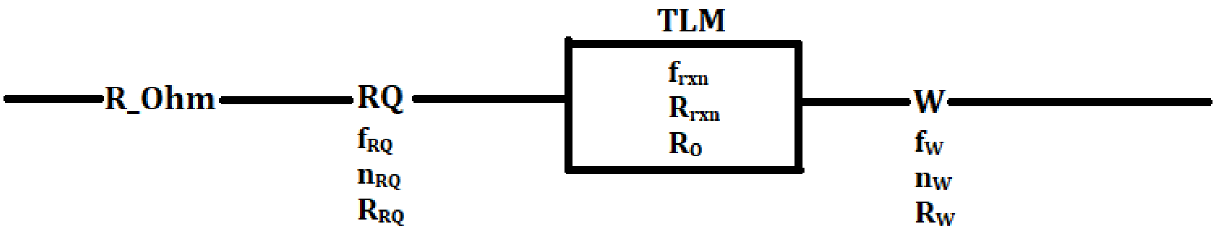

Figure 44: ECM of the tested cells, consisting of an ohmic resistor, R_Ohm, an RQ element, a TLM element and a finite-length Warburg element. Including the ohmic resistor, a total of 10 variables (3 for each non-linear circuit element) must be fit to the EIS data.

Contents

- Add DRT_Tools package, then analyze all cleaned EIS .mat files
- Retreives selected .mat file
- First initialization of fitted parameters
- Plot experimental result
- Overlay simulated results
- Have program perform CNLS fitting, or output raw variables
- Set upper and lower bounds
- Circuit Element functions

```
function varargout = R_RQ_TLM_W_ECM_Model(varargin)
% R_RQ_TLM_W_ECM_Model MATLAB code for R_RQ_TLM_W_ECM_Model.fig
```

```
%      R_RQ_TLM_W_ECM_Model, by itself, creates a new R_RQ_TLM_W_ECM_Model or raises
the existing
%      singleton*.
%
%      H = R_RQ_TLM_W_ECM_Model returns the handle to a new R_RQ_TLM_W_ECM_Model or
the handle to
%      the existing singleton*.
%
%      R_RQ_TLM_W_ECM_Model('CALLBACK',hObject,eventData,handles,...) calls the local
%      function named CALLBACK in R_RQ_TLM_W_ECM_Model.M with the given input
arguments.
%
%      R_RQ_TLM_W_ECM_Model('Property','Value',...) creates a new R_RQ_TLM_W_ECM_Model
or raises the
%      existing singleton*.  Starting from the left, property value pairs are
%      applied to the GUI before R_RQ_TLM_W_ECM_Model_OpeningFcn gets called.  An
%      unrecognized property name or invalid value makes property application
%      stop.  All inputs are passed to R_RQ_TLM_W_ECM_Model_OpeningFcn via varargin.
%
%      *See GUI Options on GUIDE's Tools menu.  Choose "GUI allows only one
%      instance to run (singleton)".
%
% See also: GUIDE, GUIDATA, GUIHANDLES

% Edit the above text to modify the response to help R_RQ_TLM_W_ECM_Model

% Last Modified by GUIDE v2.5 12-Feb-2020 23:07:54

% Begin initialization code - DO NOT EDIT
gui_Singleton = 1;
gui_State = struct('gui_Name',       mfilename, ...
                   'gui_Singleton',  gui_Singleton, ...
                   'gui_OpeningFcn', @R_RQ_TLM_W_ECM_Model_OpeningFcn, ...
                   'gui_OutputFcn',  @R_RQ_TLM_W_ECM_Model_OutputFcn, ...
                   'gui_LayoutFcn',  [] , ...
                   'gui_Callback',   []);
if nargin && ischar(varargin{1})
    gui_State.gui_Callback = str2func(varargin{1});
end

if nargout
    [varargout{1:nargout}] = gui_mainfcn(gui_State, varargin{:});
else
    gui_mainfcn(gui_State, varargin{:});
end
% End initialization code - DO NOT EDIT


% --- Executes just before R_RQ_TLM_W_ECM_Model is made visible.
function R_RQ_TLM_W_ECM_Model_OpeningFcn(hObject, eventdata, handles, varargin)
% This function has no output args, see OutputFcn.
% hObject    handle to figure
% eventdata  reserved - to be defined in a future version of MATLAB
% handles    structure with handles and user data (see GUIDATA)
% varargin   command line arguments to R_RQ_TLM_W_ECM_Model (see VARARGIN)

% Choose default command line output for R_RQ_TLM_W_ECM_Model
handles.output = hObject;
```
Add DRT_Tools package, then analyze all cleaned EIS .mat files

Enable the window to automatically update should the figure be moused over. Add basic fitted parameters to initiallize the fit. Do not list any file in the group, instead, begin calling the open file button instead of the list table.

```
addpath('DataFunctions')
% cd 'AllEISfiles'

% handles.figure1.WindowButtonMotionFcn =...
%     @(hObject,eventdata)R_RQ_TLM_W_ECM_Model('figure1_WindowButtonMotionFcn',...
%     hObject,eventdata,guidata(hObject));


% Update handles structure
guidata(hObject, handles);

% UIWAIT makes R_RQ_TLM_W_ECM_Model wait for user response (see UIRESUME)
% uiwait(handles.figure1);


% USERDATA STORED VALUES
% slider1 holds estimated fit initial values
% popupmenu holds stored experimental freq, Z', Z''
% text2-11 holds estimated handles.fitted_params()
% pushbutton1 holds a backup of the fitted_params for argument calls
% pushbutton2 holds filename

% --- Outputs from this function are returned to the command line.
function varargout = R_RQ_TLM_W_ECM_Model_OutputFcn(hObject, eventdata, handles)
% varargout  cell array for returning output args (see VARARGOUT);
% hObject    handle to figure
% eventdata  reserved - to be defined in a future version of MATLAB
% handles    structure with handles and user data (see GUIDATA)

% Get default command line output from handles structure
varargout{1} = handles.output;


% --- Executes on button press in pushbutton1.
```

Retreives selected .mat file

displays the spectra and initializes parameters.

```
function pushbutton1_Callback(hObject, eventdata, handles)
    [file, path] = uigetfile('*.mat');
    load(fullfile(path,file))
    Z_prime = Z_prime/2;
    Z_double_prime = Z_double_prime/2;
    try
    cleanData =clean_eis([freq Z_prime Z_double_prime]);
    set(handles.pushbutton1,'userdata',cleanData)
    handles.Data = cleanData;
    axes(handles.axes1)
    cla
    plot(Z_prime, Z_double_prime)
    Rtot = max(Z_prime);
    Rmin = min(Z_prime);
    R_RQ = (Rtot-Rmin)*2;
    set(handles.text2,'String',Rmin)
```

```
    set(handles.slider1,'Value',Rmin/Rtot)
```

First initialization of fitted parameters

```
    handles.fitted_params = [Rtot 4 0.6 0 1 0.9 R_RQ/2 1 R_RQ -0.7 0.5 R_RQ];
    set(handles.slider1,'userdata',handles.fitted_params);
    set(handles.pushbutton1,'String',strcat('File Read: ', file))
    set(handles.pushbutton2,'Userdata',file)
    catch
        set(handles.pushbutton1,'String','Invalid file')
    end
    initSliders(hObject, eventdata, handles);

function figure1_WindowButtonMotionFcn(hObject, eventdata, handles)
function slider1_Callback(hObject, eventdata, handles)
function slider1_CreateFcn(hObject, eventdata, handles)
if isequal(get(hObject,'BackgroundColor'), get(0,'defaultUicontrolBackgroundColor'))
    set(hObject,'BackgroundColor',[.9 .9 .9]);
end

% When any slider is called, the estimated parameters evaluated and a
% model of the simulated fits are plotted on the bode plot. Afterwards, the
% program then shifts the axis back to the nyquist plot, to prevent
% constant swapping due to the motion function.
% --- Executes on slider movement.
function slider2_Callback(hObject, eventdata, handles)
axes(handles.axes2)
cla
handles.Data = get(handles.pushbutton1,'userdata');
Rtot = max(handles.Data(:,2));
Rmin = min(handles.Data(:,2));
R_RQ = (Rtot-Rmin)*2;
% If the file does not contain any ohmic resistance, default is set to 1
try
handles.fitted_params(1) = Rtot * get(handles.slider1,'Value');
catch
    Rtot = 1;
    handles.fitted_params(1) = Rtot * get(handles.slider1,'Value');
end
% Set all sliders and their text to the fitting parameters.
set(handles.text2, 'String', handles.fitted_params(1));
handles.fitted_params(2) = 10^get(handles.slider2,'Value');
set(handles.text3, 'String', handles.fitted_params(2));
handles.fitted_params(3) = get(handles.slider3,'Value');
set(handles.text4, 'String', handles.fitted_params(3));
handles.fitted_params(4) = R_RQ * get(handles.slider4,'Value');
set(handles.text5, 'String', handles.fitted_params(4));
handles.fitted_params(5) = 10^get(handles.slider5,'Value');
set(handles.text6, 'String', handles.fitted_params(5));
handles.fitted_params(6) = get(handles.slider6,'Value');
set(handles.text7, 'String', handles.fitted_params(6));
handles.fitted_params(7) = R_RQ * (get(handles.slider7,'Value')^5);
set(handles.text8, 'String', handles.fitted_params(7));
handles.fitted_params(8) = 10^get(handles.slider8,'Value');
set(handles.text9, 'String', handles.fitted_params(8));
handles.fitted_params(9) = R_RQ * (10*get(handles.slider9,'Value'))^5;
set(handles.text10, 'String', handles.fitted_params(9));
handles.fitted_params(10) = 10^get(handles.slider10,'Value');
set(handles.text11, 'String', handles.fitted_params(10));
```

```
handles.fitted_params(11) = get(handles.slider11,'Value');
set(handles.text12, 'String', handles.fitted_params(11));
handles.fitted_params(12) = R_RQ * get(handles.slider12,'Value');
set(handles.text13, 'String', handles.fitted_params(12));
try
    try
        % Try to model the data off the experimentally stored frequencies.
        % This breaks if said file is empty
        freq_long = handles.Data(:,1);
         %generate a wide frequency space for plotting the model
    catch
        return
    end
omega_long = freq_long.*(2*pi);
R_shift = R_element(omega_long,[],1);
%unit horizontal shift element for fancy plotting
R = R_element(omega_long,[], handles.fitted_params(1));
RQ1 = RQ_element(omega_long, handles.fitted_params(2:3), handles.fitted_params(4));
% Yq, nq
TLMx = TLM_element(omega_long, handles.fitted_params(5:6), handles.fitted_params(7),
handles.fitted_params(9));
FLW = FLW_element(omega_long, handles.fitted_params(10:11),
handles.fitted_params(12));% f_w, nw
Rr = R(:,2);          Ri = -R(:,3);
RQr1 = RQ1(:,2);      RQi1 = -RQ1(:,3);
Sr = R_shift(:,2);    Si = -R_shift(:,3); % Should be 1 and 0 respectively
TLMr = TLMx(:,2);        TLMi = -TLMx(:,3);
FLWr = FLW(:,2);      FLWi = -FLW(:,3);
sim_r = Rr + RQr1 + TLMr + FLWr;
sim_i = Ri + RQi1 + TLMi + FLWi;
```

Plot experimental result

```
plot(handles.Data(:,1),-handles.Data(:,3),'ok','LineWidth',1)
handles.axes2.XScale = 'log';
handles.axes2.XGrid = 'on';
handles.axes2.XTick = [0.01,0.1,1,10,100,1000,10000,100000,1000000];
handles.axes2.XMinorGrid = 'off';
handles.axes2.YGrid = 'on';
handles.axes2.PlotBoxAspectRatio = [1 0.5 1];
```

Overlay simulated results

```
hold on
plot(handles.axes2,freq_long, sim_i, 'b-','LineWidth',1)
plot(handles.axes2,freq_long,RQi1,'-r')
plot(handles.axes2,freq_long,TLMi,'-g')
plot(handles.axes2,freq_long,FLWi,'-c')
hold off
axis auto
catch
end
axes(handles.axes1)
cla
try
plot(handles.Data(:,2),-handles.Data(:,3),'ok','LineWidth',1)
catch
end
```

```
hold on
plot(sim_r,sim_i,'b-','LineWidth',1)
plot(RQr1+Sr*(handles.fitted_params(1)), RQi1,'-r') % plots first RQ element
plot(TLMr+Sr*(handles.fitted_params(1)+handles.fitted_params(4)), TLMi,'-g')
% plots first RQ element
hold off
XGrid = 'on';
YGrid = 'on';
title('Test Fit');
```

Have program perform CNLS fitting, or output raw variables

```
function pushbutton2_Callback(hObject, eventdata, handles)
valuesR = get(handles.slider1,'userdata');
DRTdata = get(handles.pushbutton1,'Userdata');
buttonECM = eventdata.Source.Tag;
Rtot = max(DRTdata(:,2));
Rmin = min(DRTdata(:,2));
R_RQ = (Rtot-Rmin)*2;
try
handles.fitted_params(1) = Rtot * get(handles.slider1,'Value');
catch
    Rtot = 1;
    handles.fitted_params(1) = Rtot * get(handles.slider1,'Value');
end
set(handles.text2, 'String', handles.fitted_params(1));
handles.fitted_params(2) = get(handles.slider2,'Value');
set(handles.text3, 'String', handles.fitted_params(2));
handles.fitted_params(3) = get(handles.slider3,'Value');
set(handles.text4, 'String', handles.fitted_params(3));
handles.fitted_params(4) = R_RQ * get(handles.slider4,'Value');
set(handles.text5, 'String', handles.fitted_params(4));
handles.fitted_params(5) = get(handles.slider5,'Value');
set(handles.text6, 'String', handles.fitted_params(5));
handles.fitted_params(6) = get(handles.slider6,'Value');
set(handles.text7, 'String', handles.fitted_params(6));
handles.fitted_params(7) = R_RQ * (get(handles.slider7,'Value')^5);
set(handles.text8, 'String', handles.fitted_params(7));
handles.fitted_params(8) = 10^get(handles.slider8,'Value');
set(handles.text9, 'String', handles.fitted_params(8));
handles.fitted_params(9) = R_RQ * (10*get(handles.slider9,'Value'))^5;
set(handles.text10, 'String', handles.fitted_params(9));
handles.fitted_params(10) = 10^get(handles.slider10,'Value');
set(handles.text11, 'String', handles.fitted_params(10));
handles.fitted_params(11) = get(handles.slider11,'Value');
set(handles.text12, 'String', handles.fitted_params(11));
handles.fitted_params(12) = R_RQ * get(handles.slider12,'Value');
set(handles.text13, 'String', handles.fitted_params(12));
```

Set upper and lower bounds

```
fitted_params_ub = handles.fitted_params*2;
fitted_params_ub([2,5]) = handles.fitted_params([2,5])+1;
fitted_params_ub([3,6,8,10,11]) = [0.8 1 5 5 0.5];
r_rxn = handles.fitted_params(7);
r_o = handles.fitted_params(9);
T_w = handles.fitted_params(10);
fitted_params_ub([7,9, 10]) = [r_rxn*100 r_o*100 T_w*10];
```

```
fitted_params_lb = [0 -2 0.5 0 -2 0.8 r_rxn/100 -2 r_o/100 T_w/10 0 0];
fitted_params_lb([2,5]) = handles.fitted_params([2,5])-1;
readout = [fitted_params_ub;handles.fitted_params;fitted_params_lb];
% Load the experimental data and process DRT
try
    switch buttonECM
        case 'pushbutton2'
            fit = handles.fitted_params;
        case 'pushbutton3'
        [fit, err] = fit_eis_dat_RRQTLMFLW(DRTdata,...
            get(handles.pushbutton1,'String'), handles.fitted_params,...
            fitted_params_lb,fitted_params_ub);
    end
fit(2) = 10^fit(2);
fit(5) = 10^fit(5);
catch
    fit = handles.fitted_params;
    disp("Could not run fit_eis_dat")
    return;
end
% Grab basic parameters for DRT fitting
load('DRTECM.mat')
handlesDRT.lambda = 10^(-1);
fitFrequency = fit([2 5 8 10]);
handlesDRT.fitFrequency = fitFrequency([1 2 3 4]);
handlesDRT.freq = DRTdata(:,1);
handlesDRT.Z_prime_mat = DRTdata(:,2);
handlesDRT.Z_double_prime_mat = DRTdata(:,3);
handlesDRT.Z_exp = handlesDRT.Z_prime_mat(:)+
i*handlesDRT.Z_double_prime_mat(:); %this is the experimental impedance data
freq_long = handlesDRT.freq; %generate a frequency space based on the experimental
data
omega_long = freq_long.*(2*pi);
RQ1 = RQ_element(omega_long, fit(2:3), fit(4)); % Yq, nq
TLM1 = TLM_element(omega_long, fit(5:6), fit(7),fit(9)); % Yq, nq
try
    switch buttonECM
        case 'pushbutton2'
            FLW = FLW_element(omega_long, fit(8:9), fit(10));% Tw, nw
            reportfile = 'reportlogNoFit.mat';
        case 'pushbutton3'
            FLW = FLW_element(omega_long, fit(10:11), fit(12));% Tw, nw
            reportfile = 'reportlogFit.mat';
    end
catch
    fit = handles.fitted_params;
    disp("Could not run fit_eis_dat")
    return;
end
[handlesDRT] = DRT_Test(handlesDRT);
if exist('fig3') == 0
    ColorSet = varycolor(6);
    fig3 = figure('units','normalized','outerposition',[1/4 1/4 3/8 2/4]);
    hold all
    set(gca,'colororder', ColorSet)
    n3 = get(gcf,'Number');
else
    figure(n3)
end
set(gca, 'XScale', 'log')
hold on
```

```
handles.ExpFreq = handlesDRT.freq_out;
handles.Exp = handlesDRT.gamma_ridge_combined_fine;
semilogx(handles.ExpFreq, handles.Exp,'b-','LineWidth', 2);
handlesDRT.freq = freq_long;
handlesDRT.Z_prime_mat = RQ1(:,2);
handlesDRT.Z_double_prime_mat = RQ1(:,3);
handlesDRT.Z_exp = handlesDRT.Z_prime_mat(:)+
i*handlesDRT.Z_double_prime_mat(:); %this is the experimental impedance data
handlesDRT.fitFrequency = fitFrequency([1]);
handlesDRT = DRT_Test(handlesDRT);
handles.RQ1freq = handlesDRT.freq_out;
handles.RQ1 = handlesDRT.gamma_ridge_combined_fine;
semilogx(handles.RQ1freq, handles.RQ1,'-r','LineWidth', 2);
handlesDRT.Z_prime_mat = TLM1(:,2);
handlesDRT.Z_double_prime_mat = TLM1(:,3);
handlesDRT.Z_exp = handlesDRT.Z_prime_mat(:)+
i*handlesDRT.Z_double_prime_mat(:); %this is the experimental impedance data
handlesDRT.fitFrequency = fitFrequency([2]);
handlesDRT = DRT_Test(handlesDRT);
handles.RQ2freq = handlesDRT.freq_out;
handles.RQ2 = handlesDRT.gamma_ridge_combined_fine;
semilogx(handles.RQ2freq, handles.RQ2,'-g','LineWidth', 2);
try
    handlesDRT.Z_prime_mat = GE(:,2);
    handlesDRT.Z_double_prime_mat = -GE(:,3);
    handlesDRT.Z_exp = handlesDRT.Z_prime_mat(:)+
i*handlesDRT.Z_double_prime_mat(:); %this is the experimental impedance data
    handlesDRT.fitFrequency = fitFrequency([3]);
    handlesDRT = DRT_Test(handlesDRT);
    handles.GEfreq = handlesDRT.freq_out;
    handles.GE = handlesDRT.gamma_ridge_combined_fine;
    semilogx(handles.GEfreq, handles.GE,'-m','LineWidth', 2);
catch
end
try
    handlesDRT.Z_prime_mat = FLW(:,2);
    handlesDRT.Z_double_prime_mat = -FLW(:,3);
    handlesDRT.Z_exp = handlesDRT.Z_prime_mat(:)+
i*handlesDRT.Z_double_prime_mat(:); %this is the experimental impedance data
    handlesDRT.fitFrequency = fitFrequency([4]);
    handlesDRT = DRT_Test(handlesDRT);
    handles.FLWfreq = handlesDRT.freq_out;
    handles.FLW = handlesDRT.gamma_ridge_combined_fine;
    semilogx(handles.FLWfreq, handles.FLW,'-c','LineWidth', 2);
catch
end
plot(handles.ExpFreq,(handles.Exp-handles.RQ1))
plot(handles.ExpFreq,(handles.Exp-handles.RQ2))
legend('Exp. Data','RQ1','TLM','GE','FLW','Location','eastoutside')
xlabel('Z_{Real}(\Omega cm^2)');
ylabel('Z_{Imaginary}(\Omega cm^2)');
hold off
set(gca, 'XScale', 'log')
load(reportfile)
currentFilename = get(handles.pushbutton2,'Userdata');
newFilename = char(strcat...
    ("0000000000000000000000000000000000000000000000000000000000000_",...
    currentFilename));
try
    savedfiles1 = [savedfiles1; newFilename(end-83:end)];
```

```
    savedfiles3 = [savedfiles3; [fit 10^4*0.006/acoth(TLM1(end,2)*(fit(7)*fit(9))^(-
0.5))]];
    save(reportfile,'savedfiles1','savedfiles3')
catch
    savedfiles1 = newFilename(end-83:end);
    savedfiles3 = [fit 10^4*0.006/acoth(TLM1(end,2)*(fit(7)*fit(9))^(-0.5))]
    save(reportfile,'savedfiles1','savedfiles3')
end
function pushbutton3_Callback(hObject, eventdata, handles)
function initSliders(hObject, eventdata, handles)
Rtot = max(get(handles.slider1,'userdata'));
set(handles.text2, 'String', handles.fitted_params(1));
set(handles.text3, 'String', 10^handles.fitted_params(2));
set(handles.text4, 'String', handles.fitted_params(3));
set(handles.text5, 'String', handles.fitted_params(4));
set(handles.text6, 'String', 10^handles.fitted_params(5));
set(handles.text7, 'String', handles.fitted_params(6));
set(handles.text8, 'String', handles.fitted_params(7));
set(handles.text9, 'String', 10^handles.fitted_params(8));
set(handles.text10, 'String', handles.fitted_params(9));
set(handles.text11, 'String', 10^handles.fitted_params(10));
set(handles.text12, 'String', handles.fitted_params(11));
set(handles.text13, 'String', handles.fitted_params(12));

set(handles.slider1,'Value', handles.fitted_params(1)/Rtot/10);

set(handles.slider2,'Value', handles.fitted_params(2));
set(handles.slider3,'Value', handles.fitted_params(3));
set(handles.slider4,'Value', floor(handles.fitted_params(4))/Rtot/9);

set(handles.slider5,'Value', handles.fitted_params(5));
set(handles.slider6,'Value', handles.fitted_params(6));
set(handles.slider7,'Value', floor(handles.fitted_params(7))/Rtot);

set(handles.slider8,'Value', handles.fitted_params(8));
set(handles.slider9,'Value', handles.fitted_params(9)/Rtot/1000);
set(handles.slider10,'Value', handles.fitted_params(10));
set(handles.slider11,'Value', handles.fitted_params(11));
set(handles.slider12,'Value', floor(handles.fitted_params(12))/Rtot/1000);
```

Circuit Element functions

All parameters are based on the f_Rq, n_q and R, instead of the n_q, Y_q and R. This needs to be

```
function dat = R_element(omega, params, R)
 % from a given set of frequencies generates the Zr and Zi for a resistor
 Z = R;
 dat(:,1) = omega;
 dat(:,2) = real(Z);
 dat(:,3) = imag(Z);
function dat = RQ_element(omega, params, R)
 % from a given set of frequencies generates the Zr and Zi for a RQ
 % element
if R ~= 0
 f_q = params(1);
%  Y_q = params(1);
 n_q = params(2);
Y_q = (1/(2*pi*f_q)).^n_q/R;
 Q = 1 ./ (Y_q .* (omega.*1i).^n_q);
```

```
 Z = R ./ ( 1 + R.*(Q.^-1) );
else
     Z = omega* 0;
end
 dat(:,1) = omega;
 dat(:,2) = real(Z);
 dat(:,3) = imag(Z);
function dat =  TLM_element(omega, params, Rct,R_O)
 f_q = params(1);
 n_q = params(2);
 Y_q = (1/(2*pi*f_q)).^n_q/Rct;
 Q = 1 ./ (Y_q .* (omega.*1i).^n_q);
 Zct = Rct ./ ( 1 + Rct.*(Q.^-1) );
 lamb = sqrt(Zct/R_O);
 Z_TLM = R_O * (lamb .* coth(0.006*ones(length(lamb),1)./lamb));
 dat(:,1) = omega;
 dat(:,2) = real(Z_TLM);
 dat(:,3) = imag(Z_TLM);
function dat = GE_element(omega, params, R)
 % from a given set of frequencies generates the Zr and Zi for a
 % Gerischer Element
 t_c = 1/params(1);
 Z = R ./ sqrt(1+omega.*t_c.*1i);
 dat(:,1) = omega;
 dat(:,2) = real(Z);
 dat(:,3) = imag(Z);
function dat = FLW_element(omega, params, R)
 % from a given set of frequencies generates the Zr and Zi for a
 % Finite-Length Warburg Element
 T_w = params(1);
 n_w = params(2);
 Z = R .* ( tanh( (omega.*T_w.*1i).^n_w ) )./...
              ( (omega.*T_w.*1i ).^n_w ) ;
 dat(:,1) = omega;
 dat(:,2) = real(Z);
 dat(:,3) = imag(Z);




%--- Executes during object creation, after setting all properties.
function slider2_CreateFcn(hObject, eventdata, handles)
if isequal(get(hObject,'BackgroundColor'), get(0,'defaultUicontrolBackgroundColor'))
    set(hObject,'BackgroundColor',[.9 .9 .9]);
end

function slider3_Callback(hObject, eventdata, handles)
function slider3_CreateFcn(hObject, eventdata, handles)
if isequal(get(hObject,'BackgroundColor'), get(0,'defaultUicontrolBackgroundColor'))
    set(hObject,'BackgroundColor',[.9 .9 .9]);
end
function slider4_Callback(hObject, eventdata, handles)
function slider4_CreateFcn(hObject, eventdata, handles)
if isequal(get(hObject,'BackgroundColor'), get(0,'defaultUicontrolBackgroundColor'))
    set(hObject,'BackgroundColor',[.9 .9 .9]);
end
function slider5_Callback(hObject, eventdata, handles)
function slider5_CreateFcn(hObject, eventdata, handles)
if isequal(get(hObject,'BackgroundColor'), get(0,'defaultUicontrolBackgroundColor'))
    set(hObject,'BackgroundColor',[.9 .9 .9]);
end
```

```
function slider6_Callback(hObject, eventdata, handles)
function slider6_CreateFcn(hObject, eventdata, handles)
if isequal(get(hObject,'BackgroundColor'), get(0,'defaultUicontrolBackgroundColor'))
    set(hObject,'BackgroundColor',[.9 .9 .9]);
end
function slider7_Callback(hObject, eventdata, handles)
function slider7_CreateFcn(hObject, eventdata, handles)
if isequal(get(hObject,'BackgroundColor'), get(0,'defaultUicontrolBackgroundColor'))
    set(hObject,'BackgroundColor',[.9 .9 .9]);
end
function slider8_Callback(hObject, eventdata, handles)
function slider8_CreateFcn(hObject, eventdata, handles)
if isequal(get(hObject,'BackgroundColor'), get(0,'defaultUicontrolBackgroundColor'))
    set(hObject,'BackgroundColor',[.9 .9 .9]);
end
function slider9_Callback(hObject, eventdata, handles)
functon slider9_CreateFcn(hObject, eventdata, handles)
if isequal(get(hObject,'BackgroundColor'), get(0,'defaultUicontrolBackgroundColor'))
    set(hObject,'BackgroundColor',[.9 .9 .9]);
end
function slider10_Callback(hObject, eventdata, handles)
function slider10_CreateFcn(hObject, eventdata, handles)
if isequal(get(hObject,'BackgroundColor'), get(0,'defaultUicontrolBackgroundColor'))
    set(hObject,'BackgroundColor',[.9 .9 .9]);
end
function popupmenu1_Callback(hObject, eventdata, handles)
updateWindow = get(handles.popupmenu1, 'String');
switch updateWindow{hObject.Value}
    case 'Yes'
        handles.figure1.WindowButtonMotionFcn =...
         @(hObject,eventdata)R_RQ_TLM_W_ECM_Model('slider2_Callback',...
        hObject,eventdata,guidata(hObject));
    case 'No'
        handles.figure1.WindowButtonMotionFcn = [];
end
function popupmenu1_CreateFcn(hObject, eventdata, handles)
if ispc && isequal(get(hObject,'BackgroundColor'),
get(0,'defaultUicontrolBackgroundColor'))
    set(hObject,'BackgroundColor','white');
end


% --------------------------------------------------------------------
function Untitled_1_Callback(hObject, eventdata, handles)
function slider11_CreateFcn(hObject, eventdata, handles)
if isequal(get(hObject,'BackgroundColor'), get(0,'defaultUicontrolBackgroundColor'))
    set(hObject,'BackgroundColor',[.9 .9 .9]);
end


function slider12_CreateFcn(hObject, eventdata, handles)
if isequal(get(hObject,'BackgroundColor'), get(0,'defaultUicontrolBackgroundColor'))
    set(hObject,'BackgroundColor',[.9 .9 .9]);
end

function dat = clean_eis(exp_dat)
 omega = exp_dat(:,1);
 Zr = exp_dat(:,2);
 Zi = exp_dat(:,3);
 bad = any(Zi>0,2);
 if sum(bad) > length(Zi)/2
```

```
   Zi = Zi.*-1;
   bad = any(Zi>0,2);
end
c_omega = omega(~bad,:);
c_Zr = Zr(~bad,:);
c_Zi = Zi(~bad,:);
dat = [c_omega, c_Zr, c_Zi];
```

BIBLIOGRAPHY

[1] R.P. O'Hayre, S.-W. Cha, W.G. Colella, F.B. Prinz, Fuel Cell Fundamentals, John Wiley & Sons, Inc., Hoboken, New Jersey, 2016.

[2] S.C. Singhal, K. Kendall, eds., High Temperature Solid Oxide Fuel Cells: Fundamentals, Design and Applications, 1st ed., Elsevier Ltd, Oxford, UK, 2003.

[3] U.S. Department of Energy, Technology Program Plan Solid Oxide Fuel Cells, Solid Oxide Fuel Cell Technol. Progr. Plan. (2013). https://www.netl.doe.gov/File Library/Research/Coal/energy systems/fuel cells/Program-Plan-Solid-Oxide-Fuel-Cells-2013.pdf.

[4] K.J. Yoon, S. Gopalan, U. B. Pal, Performance Analysis of Single Step Co-fired Solid Oxide Fuel Cells (SOFCs), ECS Transactions. 25 (2009) 533-542. doi: 10.1149/1.3205564.

[5] R. Wang, M. Würth, U. B. Pal, S. Gopalan, S. N. Basu. Roles of humidity and cathodic current in chromium poisoning of Sr-doped $LaMnO_3$-based cathodes in solid oxide fuel cells, Journal of Power Sources. 360 (2017) 87-97. doi: 10.1016/j.jpowsour.2017.06.005.

[6] J.T.S. Irvine, P. Connor, Solid Oxide Fuel Cells: Facts and Figures / Past, Present and Future Perspectives for SOFC Technologies, Springer-Verlag, London, 2013. doi:10.1007/978-1-4471-4456-4.

[7] G.C. Karvountzi, C. M. Price, P. F. Duby, Effect of Fuel Cell Operation Pressure on the Optimization of a Hybrid System SOFC/Turbine for Cogeneration, Proceedings of the ASME 2004 2nd International Conference on Fuel Cell Science, Engineering and Technology, American Society of Mechanical Engineers Digital Collection. (2008) 625-631. doi: 10.1115/FUELCELL2004-2531.

[8] M. Nguyen, Solid Oxide Fuel Cell Systems for Power Generation Applications, ECS Proceedings Volumes. (2003) 43-47. doi: 10.1149/200307.0043PV.

[9] S. Suresh, J. Targoff, S. Lasher, E. Carlson, R. Zogg, Challenges and Opportunities for Fuel Cells in Stationary Power Generation, Cogeneration & Distributed Generation Journal. 3 (2009) 31-42. doi: 10.1080/15453660509509067.

[10] S.P. Jiang, Nanoscale and nano-structured electrodes of solid oxide fuel cells by infiltration: Advances and challenges, International Journal of Hydrogen Energy. 37 (2012) 449-470. doi: 10.1016/j.ijhydene.2011.09.067

[11] Z. Liu, B. Liu, D. Ding, M. Liu, F. Chen, C. Xia, Fabrication and modification of solid oxide fuel cell anodes via wet impregnation/infiltration technique, Journal of Power Sources. 237 (2013) 243-259. doi: 10.1016/j.jpowsour.2013.03.025.

[12] J.T.S. Irvine, D. Neagu, M. C. Verbraeken, C. Chatzichristodoulou, C. Graves, M. B. Mogensen, Evolution of the electrochemical interface in high-temperature fuel cells and electrolysers, Nature Energy. 1 (2016) 15014. doi: 10.1038/nenergy.2015.14

[13] P.A. Connor, X. Yue, C.D. Savaniu, R. Price, G. Triantafyllou, M. Cassidy, G. Kerherve, D.J. Payne, R.C. Maher, L.F. Cohen, R.I. Tomov, B.A. Glowacki, R.V. Kumar, J.T.S. Irvine, Tailoring SOFC Electrode Microstructures for Improved Performance, Advanced Energy Materials. 8 (2018) 1–20. doi:10.1002/aenm.201800120.

[14] P. Gasper, Y. Lu, S. N. Basu, S. Gopalan, U. B. Pal, Effect of anodic current density on the spreading of infiltrated nickel nanoparticles in nickel-yttria stabilized zirconia cermet anodes, Journal of Power Sources. 410 (2019) 196-203. doi: 10.1016/j.jpowsour.2018.11.002.

[15] Y. Lu, Improving intermediate temperature performance of NI-YSZ cermet anodes for solid oxide fuel cells by infiltration of nickel nanoparticles and mixed ionic electronic conductors. Boston University.

[16] A. Bertei, J. G. Pharoah, D. A. W. Gawel, C. Nicolella, Microstructural Modeling and Effective Properties of Infiltrated SOFC Electrodes, ECS Transactions. 57 (2013) 2527-2536. doi: 10.1149/05701.2527ecst.

[17] L. Holzer, B. Münch, B. Iwanschitz, M. Cantoni, T. Hocker, T. Graule, Quantitative relationships between composition, particle size, triple phase boundary length and surface area in nickel-cermet anodes for Solid Oxide Fuel Cells, Journal of Power Sources. 196 (2011) 7076–7089. doi:10.1016/j.jpowsour.2010.08.006.

[18] M. Li, B. Hua, J. Luo, S. P. Jiang, J. Pu, B. Chi, J. Li, Enhancing Sulfur Tolerance of Ni-Based Cermet Anodes of Solid Oxide Fuel Cells by Ytterbium-Doped Barium Cerate Infiltration, ACS Applied Materials & Interfaces. 8 (2016) 10293-10301. doi: 10.1021/acsami.6b00925.

[19] B. Timurkutluk, C.Timurkutluk, M. D. Mat, Y. Kaplan, Anode-supported solid oxide fuel cells with ion conductor infiltration, International Journal of Energy Research. 35 (2011) 1048-1055. doi: 10.1002/er.1832.

[20] P. Keyvanfar, V. Birss, Optimization of Infiltration Techniques Used to Construct Ni/YSZ Anodes, Journal of the Electrochemical Society. 161 (2014) F660-F667. doi:10.1149/2.056405jes.

[21] R. Kiebach, P. Zielke, J.V.T. Hogh, K. Thyden, H.J. Wang, R. Barford, P. V. Hendriksen, Infiltration of SOFC Stacks: Evaluation of the Electrochemical Performance Enhancement and the Underlying Changes in the Microstructure, Fuel Cells. 16 (2016) 80-88. doi:10.1002/fuce.201500107.

[22] Y.A. Chart, M.Y. Lu, S. A. Barnett, High-Performance Oxygen Electrodes for Low Temperature Solid Oxide Cells, ECS Meeting Abstracts. MA2019-01 (2019) 1713-1713. doi: 10.1149/MA2019-01/33/1713.

[23] M. Hattori, Y. Takeda, J.-H. Lee, S. Ohara, K. Mukai, T. Fukui, S. Takahashi, Y. Sakaki, A. Nakanishi, Effect of annealing on the electrical conductivity of the Y_2O_3–ZrO_2 system, Journal of Power Sources. 131 (2004) 247-250. doi: /10.1016/j.jpowsour.2003.11.084.

[24] B.A. Boukamp, A Linear Kronig-Kramers Transform Test for Immittance Data Validation, Journal of the Electrochemical Society. 142 (1995) 1885–1894. doi:10.1149/1.2044210.

[25] V. Sonn, A. Leonide, E. Ivers-Tiffée, Combined Deconvolution and CNLS Fitting Approach Applied on the Impedance Response of Technical Ni / 8YSZ Cermet Electrodes, Journal of The Electrochemical Society. 155 (2008) B675-B679. doi: 10.1149/1.2908860.

[26] T. H. Wan, M. Saccoccio, C. Chen, F. Ciucci, Influence of the Discretization Methods on the Distribution of Relaxation Times Deconvolution: Implementing Radial Basis Functions with DRTtools, Electrochimical Acta. 184 (2015) 483-499. doi:/10.1016/j.electacta.2015.09.097.

[27] T. E. Burye, J.D. Nicholas, Precursor solution additives improve desiccated $La_{0.6}Sr_{0.4}Co_{0.8}Fe_{0.2}O_{3-x}$ infiltrated solid oxide fuel cell cathode performance, J. Power Sources 301 (2016) 287-298. doi: 10.1016/j.jpowsour.2015.10.012.

[28] J. D. Nicholas, S. A. Barnett, Measurements and Modeling of $Sm_{0.5}Sr_{0.5}CoO_{3-x}$ – $Ce_{0.9}Gd_{0.1}O_{1.95}$ SOFC Cathodes Produced Using Infiltrate Solution Additives, Journal of The Electrochemcial Society. 157 (2010) B536. doi: 10.1149/1.3284519.

[29] P. J. Gasper, Improving Electrochemical Performance Of Nickel – Yttria Stabilized Zirconia Cermet Anodes Employing Nickel Nanoparticles, Boston University, 2019.

[30] C. Ahamer, A. K. Opitz1, G. M. Rupp, J. Fleig, Revisiting the Temperature Dependent Ionic Conductivity of Yttria Stabilized Zirconia (YSZ), Journal of The Electrochemcial Society. 164 (2017) F790. doi: /10.1149/2.0641707jes.

[31] T. Klemenso, M, Mogensen, Ni-YSZ Solid Oxide Fuel Cell Anode Behavior Upon Redox Cycling Based on Electrical Characterization, Journal of the American Ceramic Society. 90 (2007) 3582-3588. doi:10.1111/j.1551-2916.2007.01909.x.

[32] A. Buyukaksoy, S. P. Kammampata, V. I. Birss, Effect of porous YSZ scaffold microstructure on the long-term performance of infiltrated Ni-YSZ anodes, Journal of Power Sources. 287 (2015) 349-358. doi: 10.1016/j.jpowsour.2015.04.072.

[33] T. Skafte, J. Hjelm, P. Blennow, C. Graves, Reactivating the Ni-YSZ electrode in solid oxide cells and stacks by infiltration, Journal of Power Sources. 378 (2018) 685-690. doi: 10.1016/j.jpowsour.2018.01.021.

[34] A.N.N. Busawon, D. Sarantaridis, A. Atkinson, Ni Infiltration as a Possible Solution to the Redox Problem of SOFC Anodes, Electrochemical and Solid-State Letters. 11 (2008) B186. doi:10.1149/1.2959078.

[35] S.W. Kim, M. Park, H. Kim, K.J. Yoon, J.W. Son, J.H. Lee, B.K. Kim, J.H. Lee, J. Hong, In-situ nano-alloying Pd-Ni for economical control of syngas production from high-temperature thermo-electrochemical reduction of steam/CO_2, Applied Catalysis. B, Environmental. 200 (2017) 265–273. doi:10.1016/j.apcatb.2016.07.008.

[36] L. Adijanto, R. Küngas, J. Park, J.M. Vohs, R.J. Gorte, SOFC anodes based on infiltration of tungsten bronzes, International Journal of Hydrogen Energy. 36 (2011) 15722-15730. doi: 10.1016/j.ijhydene.2011.09.059.

[37] E.C. Miller, Q. Sherman, Z. Gao, P. W. Voorhees, S. A. Barnett, Stability of Nickel-Infiltrated Anodes in Intermediate Temperature SOFCs, ECS Meeting Abstracts, MA2015-03, 267. doi.org/10.1149/MA2015-03/1/267.

[38] M. Lomberg, E. Ruiz-Trejo, G. Offer, N.P. Brandon, Characterization of Ni-infiltrated GDC electrodes for solid oxide cell applications, Journal of the Electrochemical Society. 161 (2014) F899–F905. doi:10.1149/2.0501409jes.

[39] B.A. Boukamp, Fourier transform distribution function of relaxation times; application and limitations, Electrochimica Acta. 154 (2015) 35–46. doi:10.1016/j.electacta.2014.12.059.

[40] B.A. Boukamp, A. Rolle, Use of a distribution function of relaxation times (DFRT) in impedance analysis of SOFC electrodes, Solid State Ionics. 314 (2018) 103–111. doi:10.1016/j.ssi.2017.11.021.

[41] B.A. Boukamp, A. Rolle, Analysis and Application of Distribution of Relaxation Times in Solid State Ionics, Solid State Ionics. 302 (2016) 12–18. doi:10.1016/j.ssi.2016.10.009.

[42] B.A. Boukamp, Derivation of a Distribution Function of Relaxation Times for the (fractal) Finite Length Warburg, Electrochimica Acta. 252 (2017) 154–163. doi:10.1016/j.electacta.2017.08.154.

[43N] A. Faes, A. Hessler-Wyser, D. Presvytes, C. G. Vayenas, and J. Van Herle. *Fuel cells*, 9(6), 841 (2009).

[44] A. Hagen, R. Barfod, P. V. Hendriksen, Y.-L. Liu, S. Ramousse. Degradation of Anode Supported SOFCs as a Function of Temperature and Current Load, Journal of the Electrochemical Society. 153 (2006) A1165-A1171. doi: 10.1149/1.2193400.

[45] K .J. Yoon, S. Gopalan, U. B. Pal, Effect of Anode Active Layer on Performance of Single Step Co-fired Solid Oxide Fuel Cells (SOFCs), ECS Transactions. 13 (2008) 249-257. doi: 10.1149/1.3050397.

[46N] S. Darvish, S. Gopalan, Y. Zhong, Thermodynamic stability maps for the $La_{0.6}Sr_{0.4}Co_{0.2}Fe_{0.8}O_{3\pm\delta}$–$CO_2$–$O_2$ system for application in solid oxide fuel cells, Journal of Power Sources,. 336 (2016), 351-359. doi.org/10.1016/j.jpowsour.2016.10.004.

[47N] R. Wang, Z. Sun, U. B. Pal, S. N. Basu, S. Gopalan, Mitigation of chromium poisoning of cathodes in solid oxide fuel cells employing $CuMn_{1.8}O_4$ spinel coating on metallic interconnect, Journal of Power Sources, 376 (2018), 100-110. doi.org/10.1016/j.jpowsour.2017.11.069.

[48N] Z. Sun, R. Wang, A. Y. Nikiforov, S. Gopalan, U. B. Pal, S. N. Basu, $CuMn_{1.8}O_4$ protective coatings on metallic interconnects for prevention of Cr-poisoning in solid oxide fuel cells, Journal of Power Sources, 378 (2018), 125-133.

[49N] A. Leonide, Y. Apel, and E. Ivers-Tiffee, SOFC Modeling and Parameter Identification by Means of Impedance Spectroscopy, ECS Transactions, 19(20) (2009), 81-109. doi.org/10.1149/1.3247567.

[50N] A. Leonide, V. Sonn, A. Weber, and E. Ivers-Tiffée, Evaluation and Modeling of the Cell Resistance in Anode-Supported Solid Oxide Fuel Cells, Journal of The Electrochemical Society, 155(1) (2008), B36. doi.org/10.1149/1.2801372.

[51N] K. J. Yoon, M. Biswas, H. J. Kim, M. Park, J. Hong, H. Kim, J. W. Son, J. H. Lee, B. K. Kim, H. W. Lee, Nano-tailoring of infiltrated catalysts for high-temperature solid oxide regenerative fuel cells, Nano Energy, 36 (2017), 9-20. doi.org/10.1016/j.nanoen.2017.04.024

[52N] S. N. Basu, Y. Lu, P. J. Gasper, S. Gopalan, U. B. Pal, Enhancing Anodic Catalytic Activity at High Fuel Utilization By Infiltration of Ni Nanoparticles, ECS Transactions, 78(1) (2017), 1397. doi.org/10.1149/07801.1397ecst.

[53] M. D. Gross, J. M. Vohs, R. J. Gorte, Enhanced Thermal Stability of Cu-Based SOFC Anodes by Electrodeposition of Cr, Journal of The Electrochemical Society, 153 (2006) A1386-A1390. doi: 10.1149/1.2201534.

[54] S. McIntosh, J.M. Vohs, R. J. Gorte. Role of Hydrocarbon Deposits in the Enhanced Performance of Direct-Oxidation SOFCs, Journal of The Electrochemical Society, 150 (2003) A470-A476. doi: 10.1149/1.1559064.

[55N] O. Costa-Nunes, R. J. Gorte, J. M. Vohs, Comparison of the performance of Cu–CeO_2–YSZ and Ni–YSZ composite SOFC anodes with H2, CO, and syngas, Journal of Power Sources, 141(2)(2005), 241-249. doi.org/10.1016/j.jpowsour.2004.09.022.

[56] Y. Lu, P. Gasper, U. B. Pal, S. Gopalan, S. N. Basu, Improving intermediate temperature performance of Ni-YSZ cermet anodes for solid oxide fuel cells by liquid infiltration of nickel nanoparticles, Journal of Power Sources. 396 (2018) 257-264. doi:10.1016/j.jpowsour.2018.06.027.

[57] Y. Lu, P. Gasper, A. Y. Nikiforov, U. B. Pal, S. Gopalan, S. N. Basu, Co-infiltration of Nickel and Mixed Conducting $Gd_{0.1}Ce_{0.9}O_{2-\delta}$ and $La_{0.6}Sr_{0.3}Ni_{0.15}Cr_{0.85}O_{3-\delta}$ Phases in Ni-YSZ Anodes for Improved Stability and Performance, JOM, 71(2019) 3835. doi: /10.1007/s11837-019-03723-1.

[58] R. Fernández-González, J. C. Ruiz-Morales, J. Canales-Vázquez, J. R. Jurado, A. Makradi, P. Núñez, Decreasing the polarisation resistance of a Ni-YSZ solid oxide fuel cell anode by infiltration of a ceriabased solution, International Journal of Hydrogen Energy. 41 (2016) 19731-19736. doi: /10.1016/j.ijhydene.2016.03.092.

[59] S. A. Barnett, B.-K. Park, R. Scipioni, Effect of Infiltration on Performance of Ni-YSZ Fuel Electrodes, ECS Transactions. 91 (2019) 1791-1797. doi: 10.1149/09101.1791ecst.

[60N] T. Horita, K. Yamaji, N. Sakai, Y. Xiong, T. Kato, H. Yokokawa, T. & Kawada. J Power Sources, 106(1-2), 224 (2002).

[61N] K. J. Yoon, S. Gopalan, U. B. Pal, Analysis of Electrochemical Performance of SOFCs Using Polarization Modeling and Impedance Measurements, Journal of The Electrochemical Society, 156 , 3 (2009), B311. doi.org/10.1149/1.3046158

[62N] K. Kobayashi, Y. Kai, S. Yamaguchi, N. Fukatsu, T. Kawashima, Y. Iguchi, Electronic conductivity measurements of 5 mol% TiO2-doped YSZ by a d.c.-polarization technique, Solid State Ionics, 93, 3-4 (1997), 193. doi.org/10.1016/S0167-2738(96)00534-6.

[63N] A.J. Feighery, J.T.S. Irvine, D.P. Fagg, A. Kaiser, Phase Relations at 1500°C in the Ternary System ZrO2–Y2O3–TiO2, Journal of Solid State Chemistry, 143, 2 (1999), 273-276. doi.org/10.1006/jssc.1998.8108.

[64] D. Skarmoutsos, P. Nikolopoulos, A, Tsoga, Titania doped YSZ for SOFC anode Ni-cermet, Ionics, 5 (1999), 455–459. https://doi.org/10.1007/BF02376013.

[65] A. Kaiser, A. J. Feighery, D. P. Fagg, J. T. S. Irvine, Electrical characterization of highly Titania doped YSZ, Ionics, 4 (1998), 215–219. https://doi.org/10.1007/BF02375948.

[66] B. Y. Park, R. Scipioni, D. Cox, S. A. Barnett, Enhancement of Ni-$(Y_2O_3)_{0.08}(ZrO_2)_{0.92}$ fuel electrode performance by infiltration of $Ce_{0.8}Gd_{0.2}O_{2-\delta}$ nanoparticles, Journal of Materials Chemistry A, 8.7 (2020) 4099-4106. doi.org/10.1039/C9TA12316D.

[67] B. Mo, J. Rix, U. B. Pal, S. N. Basu, S. Gopalan, Characterizing Performance of Electrocatalyst Nanoparticles Infiltrated into Ni-YSZ Cermet Anodes for Solid Oxide Fuel Cells, Journal of The Electrochemical Society, 167(5) (2020), 54515. doi.org/10.1149/1945-7111/ab74bf.

[68] J. Nielsen, T. Klemensø, and P. Blennow, Detailed impedance characterization of a well performing and durable Ni:CGO infiltrated cermet anode for metal-supported solid oxide fuel cells, Journal of Power Sources, 219 (2012), 305-316. doi.org/10.1016/j.jpowsour.2012.07.031.

[69] T. Takeuchi, E. Bétourné, D. C. Sinclair, M. Tabuchi, A. R. West, H. Kageyama, Densification and conductivity enhancement of $Na_4Zr_2Si_3O_{12}$-based solid electrolytes using TiO_2 as a sintering aid, Solid State Ionics, 120, 1-4 (1999) 33-41. doi.org/10.1016/S0167-2738(99)00004-1.

[70] W. D. Callister, M. L. Johnson, I. B. Cutler, R. W. Ure, Sintering chromium oxide with the aid of TiO_2, Journal of the American Ceramic Society, 62, 3-4 (1979): 208-211. doi.org/10.1111/j.1151-2916.1979.tb19056.x.

[71] M. I. Osendi, J. S. Moya, Role of titania on the sintering, microstructure and fracture toughness of Al_2O_3/ZrO_2 composites, Journal of Materials Science Letters, 7 (1988), 15-18. doi.org/10.1007/BF01729901.

[72] T. S. Zhang, J. Ma, L. B. Kong, S.H. Chan, P. Hing, J.A. Kilner, Iron oxide as an effective sintering aid and a grain boundary scavenger for ceria-based electrolytes, Solid State Ionics, 167.1-2 (2004), 203-207. doi.org/10.1016/j.ssi.2004.01.006.

[73] A. S. Mehranjani, D. J. Cumming, D. C. Sinclair, R. H. Rothman, Low-temperature co-sintering for fabrication of zirconia/ceria bi-layer electrolyte via tape casting using a Fe_2O_3 sintering aid, Journal of the European Ceramic Society 37.13 (2017) 3981-3993.doi.org/10.1016/j.jeurceramsoc.2017.05.018.

[74] S. Sivakumar, H. L. Teow, R. Singh, A. Niakan, N. Mase, The Effect of Iron Oxide on the Mechanical and Ageing Properties of Y-TZP Ceramic, Key Engineering Materials, 701 (2016), 225–229. doi.org/10.4028/www.scientific.net/kem.701.225.

[75] J. Ascolani-Yael, A. Montenegro-Hernández, Q. Liu, S. A. Barnett, L. Mogni, Study of $La_{0.6}Sr_{0.4}Co_{1-x}Fe_xO_{3-\delta}$ (x = 0.2 & 0.8) Electrochemical Response as SOFC Cathodes and Its Relation with Microstructure, Journal of The Electrochemical Society, 166 (2019), F1301. doi.org/10.1149/2.0281916jes.

[76] J. Kim, G.H. Kim, K. Park, Porous NiO–YSZ and Ni–YSZ composites fabricated using NiO–YSZ composite nanopowders and WO3 additive, Materials Characterization, 160 (2020) 110113. doi.org/10.1016/j.matchar.2019.110113.

[77] S. M. Khaliullin, A.S. Khaliullina, A.Y. Neiman, High-temperature conductivity and structure of $Y_2(WO_4)_3$ ceramics, Russian J. Phys. Chem. B, 10 (2016), 62-68. doi.org/10.1134/S1990793116010176.

[78] M. Y. Lu, R. Scipioni, B. K. Park, T. Yang, Y. A. Chart, S. A. Barnett, Mechanisms of PrOx performance enhancement of oxygen electrodes for low and intermediate temperature solid oxide fuel cells, Materials Today Energy, (14) 2019 100362. doi.org/10.1016/j.mtener.2019.100362.

[79] A. Bertei, E. Ruiz-Trejo, K. Kareh, V. Yufit, X. Wang, F. Tariq, N.P. Brandon, The fractal nature of the three-phase boundary: A heuristic approach to the degradation of nanostructured Solid Oxide Fuel Cell anodes, Nano Energy. 38 (2017) 526–536. doi:10.1016/j.nanoen.2017.06.028.

[80] C. Endler, A. Leonide, A. Weber, F. Tietz, E. Ivers-tiffée, Time-Dependent Electrode Performance Changes in Intermediate Temperature Solid Oxide Fuel Cells, Journal of the Electrochemical Society. 157 (2010) 292–298. doi:10.1149/1.3270047.

[81] K.J. Yoon, S. Gopalan, U.B. Pal, Effect of fuel composition on performance of single-step cofired SOFCs, Journal of the Electrochemical Society. 154 (2007) B1080. doi:10.1149/1.2769826.

[82] B. Mo, J. Rix, U. B. Pal, S. N. Basu, S. Gopalan, Improving SOFC Anode Electrocatalytic Activity Using Nanoparticle Infiltration into MIEC Compositions, Journal of The Electrochemical Society, 167(13) (2020), 134506. doi.org/10.1149/1945-7111/abb70f.

[83] B.F. Lasagni, A. Lasagni, M. Engstler, H.P. Degischer, F. Mücklich, Nanocharacterization of cast structures by FIB-tomography, Advanced Engineering Materials. (2008) 62‑66. doi:10.1002/adem.200700249.

CURRICULUM VITAE

Boshan Mo
B.S. in Electrical Engineering, 2016, Boston University
M.S. in Materials Science and Engineering, 2016, Boston University

Conference presentations:

B. Mo, “Effect of Nanoparticle Impregnation on Ni-YSZ Cermet Electrode Polarization Using YSZ-Supported Cells”, presented at ECS, May. 25th, 2019, Dallas, TX.

Prior publications:

B. Mo, J. Rix, U. B. Pal, S. N. Basu, S. Gopalan, Improving SOFC Anode Electrocatalytic Activity Using Nanoparticle Infiltration into MIEC Compositions, Journal of The Electrochemical Society, 167 (2020), 134506. doi.org/10.1149/1945-7111/abb70f.

B. Mo, J. Rix, U. B. Pal, S. N. Basu, S. Gopalan, Characterizing Performance of Electrocatalyst Nanoparticles Infiltrated into Ni-YSZ Cermet Anodes for Solid Oxide Fuel Cells, Journal of The Electrochemical Society, 167 (2020), 54515.

Wang, Ruofan, Manuel Würth, Boshan Mo, Uday Bhanu Pal, Srikanth Gopalan, and Soumendra Nath Basu. "Effect of Humidity and Cathodic Current on Chromium Poisoning of Sr-Doped LaMnO3-Based Cathode in Anode-Supported Solid Oxide Fuel Cells." ECS Transactions 75, no. 42 (2017): 61-67.

Huang, Guiqing, Boshan Mo, and Youde Mo. "Methods of making low cost electrode active materials for secondary batteries from ilmenite." U.S. Patent 9,577,257, issued February 21, 2017.

Huang, Guiqing, Boshan Mo, and Youde Mo. "Method of synthesizing phosphate salt of high purity." U.S. Patent Application 15/586,715, filed November 16, 2017.

Huang, Guiqing, Boshan Mo, and Youde Mo. "Methods of making low cost electrode active composite materials for secondary electrochemical batteries." U.S. Patent 9,296,612, issued March 29, 2016.